Monitoring an Air Core by means of Electrical Resistance Tomography

Prepared For: The Department of Electrical Engineering at the University of Cape Town

Prepared By: J. Elliott

Date: 26 March 2006

Dissertation submitted in partial fulfilment of the requirements
Of the degree of Master of Science (MSc) in Electrical
Engineering at the University of Cape Town

30/03/2006

Signed by candidate

Signature removed

Acknowledgements

My sincerest thanks to Prof John Tapson for supervising and guiding me throughout the duration of the project. I would like to thank UCT's Mechanical Engineering workshop for their help with the mechanical construction of the electrode and blender rigs. I would like to thank Dr. Wilkinson and his research group for allowing me to use the TDM ERT system and for helping me with some of the off-line reconstruction software. I would also like to thank my family for all their support. Most of all, I would like to thank God for guiding safely up to this stage of my life.

Abstract

Cyclonic separators have been used in industrial separation processes for many years. Some of these processes include: the cotton industry, grain processing, food processing, and chemical and mineral processing. In these various processes, the separation of solid and liquid particles from gas or liquid media is employed. For solid-liquid separation, the process takes place in a liquid phase continuum. In most cases, this liquid phase continuum is dense and opaque, and therefore the internal flow within these cyclonic separators has been a mystery for many years.

More recently, there has been a massive increase in research into cyclonic separation devices and processes. This is owing to the fact that there is a large need for the optimisation and control of such devices in order to utilise resources more effectively, reduce environmental impact, and make the entire process much more cost efficient.

In an industrial setup involving cyclonic separators, it is very hard to determine the optimal operating point so that the device's performance is at a maximum. One measurement strategy that does offer great insight into such problem is tomography. It has been found that the air core formed inside a cyclonic separator is one means of determining the separator's performance. This air core can be measured and visualised by means of Electrical Resistance Tomography (ERT).

In most cases, ERT is employed with Time Domain Multiplexing (TDM). However, at the University of Cape Town (UCT), an innovative ERT system utilising Frequency Domain Multiplexing (FDM) has been developed. This paper describes a comparison, performed at UCT, between a TDM ERT and the FDM ERT system. Both systems were involved with capturing data related to air core behaviour within a cyclonic separator. This data was used to train neural networks and make air core diameter predictions from unseen data for both systems. Both static and dynamic measurements were used in the process, and the FDM ERT system was found to be more accurate. However, the TDM system does offer the advantages of image reconstruction and greater speed. With more software development the FDM system could offer low resolution image recomstruction.

Table of Contents

List of Illustrations

Figures

Tables

1 Introduction

This thesis describes the implementation and testing of two electrical resistance tomography (ERT) systems, one using frequency domain multiplexing and the other using time domain multiplexing, to monitor and predict the diameter of an air core inside a process vessel.

1.1 Background

In the industrial processing of minerals, the initial step is to liberate all minerals in a rock or ore feed by means of grinding or natural size reduction. Once this step has been completed, the minerals then need to be separated individually.

One such process is that of separating diamonds from kimberlite. In the diamond separation process, the diamond plant utilizes the difference in relative densities between the diamonds and the host rock to separate the diamonds into a small parcel of high density material [40]. The initial feed for this process is mixed into a suspension of finely ground ferrosilicate slurry and this slurry is then pumped into a cyclonic separator which yields a concentrate of diamonds and high density material.

When cyclonic separators are used for separation, it is very difficult to determine the optimal operating point and keep the separator's performance at a maximum. This is because of the nature of the process. The ferrosilicate slurry is very dense and opaque, and as a result it is not possible to make any visual observations.

In order to address the problems of monitoring cyclonic separators, many researchers have designed different tomography systems which try to image the interior of the process vessel. The main requirement for one of these tomography

systems is that it should not interfere with or affect the separation process in any manner that would cause a decrease in the separator's efficiency.

As with all processes, an operating cost is present and therefore if these tomography systems can monitor the cyclonic separator's performance and keep it at a maximum, then the operating costs will be kept to a minimum.

To address the above problems, a research project on monitoring an industrial hydrocyclone using Electrical Impedance Tomography (EIT) was initiated in 2004 by Prof. J. Tapson and Mr. V. Capindissa. The aims of the project were to introduce an online measurement system which would acquire data to be used in various monitoring and control strategies. For these purposes Capindissa [27] used a frequency domain multiplexed (FDM) EIT system. This EIT system was then changed to a FDM ERT (electrical resistance tomography) system by Goldswain [28], and the ERT system is yet to be tested on the hydrocyclone.

1.2 Description of Problems to be Investigated

The following areas must be investigated with respect to the existing FDM ERT system:

- Determine whether the ERT system is capable of monitoring a hydrocyclone.
- Determine the accuracy of the system.
- Make a comparison between the FDM ERT system and a TDM ERT system (in terms of both accuracy and speed).
- Image the air core at various stations from top to bottom of the cyclone.

1.3 Significance of Specified Problems

In the separation of minerals, the fluid being processed is pumped into the cyclonic separators at a very high pressure. This means that the fluid moves very quickly. Therefore if the ERT system is going to track all the changes happening inside the process vessel on a real-time basis, it needs to be equally fast. The EIT system used by Capindissa [27] was able to run at roughly 200 frames per second (which is sufficiently fast), but since Goldswain [28] changed the system to an ERT system, no real-time tests on the hydrocyclone have taken place in order to determine the tomography system's abilities.

Various researchers have discovered that the operating state and efficiency of separation of a cyclonic separator can be determined and controlled by means of monitoring the air core formed inside one of these separation devices [27]. This air core may be monitored by means of an ERT system (it will be in this report). Now, because the air core formed is normally only a few millimetres in diameter, the ERT system which is going to monitor the separator needs to be highly accurate and relatively unaffected by any noise created by the pump motor.

There are currently two ERT systems that exist at the University of Cape Town (UCT), a FDM ERT system [20] and a TDM ERT system [32, 33, 35]. The FDM ERT system is the only existing FDM system worldwide and is therefore the fastest FDM system. The TDM system is the fastest ERT system built to date. Both these systems need to be tested in various manners in order to make a comparison as to which of the two systems would be better for the purpose of monitoring a cyclonic separator.

1.4 Objectives of Research

The objectives of this research project are to:

- Design and construct new and improved electrode rigs which can be attached to both the ERT systems.
- Capture data from both systems which will be used for determining the whether each system is capable of monitoring a cyclonic separator.
- Design offline reconstruction code and make a comparison between the two systems based on their reconstruction results from all the captured data.
- Make recommendations for both ERT systems, new electrode designs, and for new reconstruction methods.

1.5 Limitations and Scope of Research

Although various concerns emerged during the research process, the focus of the research was limited to the fact that some of aspects of the project were originally developed by other members of the research group and by other researchers outside the research group.
These limitations included:

- The hardware for the FDM system was developed a few years ago, and as a result, the system will probably not be as fast and accurate as it could be.
- The TDM system belongs to another research group and all research related to it will have to be done according to the other group's time schedule.
- The online reconstruction software for the FDM system was originally designed for an EIT system and as a result no online reconstruction software exists for the ERT system.

- The limited amount of time required to research, design, construct and sufficiently test the electrode rigs and reconstruction methods.

1.6 Plan of Development

The dissertation begins with a review of all relevant literature written on cyclonic separators and the techniques used to monitor them. This includes the hardware, software and reconstruction techniques for various tomography systems. It then focuses on the system structure of the two ERT systems which will be used for the purposes of this paper, and the design and construction of all the new electrode rigs for the tomography systems. Attention is then paid to the new software used for offline reconstruction of all the captured data for both systems, including image reconstruction software and neural network diameter prediction software. All results obtained from the testing of the ERT systems are then presented and discussed. After the results have been examined, various conclusions will be made, based on the results of all the testing done. Lastly, recommendations will be made regarding these results and conclusions.

2 Review of Previous Work Done

In mineral processing, the initial step is to liberate all the minerals in a rock or ore feed either by grinding or natural size reduction, after which they can be separated individually. However, depending on their behaviour and properties, different separation technologies can be applied. One of these technologies is separation by gravity. Separation by gravity makes use of the fact that if there is a difference in density between the individual phases/minerals in a feed, they can be separated using this density difference [2, 3].

The main application of interest with respect to this form of separation (using the density difference), is that of cyclonic separators.

2.1 Cyclonic Separators

Cyclonic separators use the centrifugal force generated by a fluid vortex and utilise the different phase densities to separate a multi-phase (liquid, solid, and gas) flow or feed into its individual phases [1]. The required vortex is created by pumping a fluid tangentially into a cylindrical section of a separator under high pressure [3]. A cyclonic separator has no moving parts, and there are various separator arrangements that have been designed and built in order to achieve the highest possible percentage recovery of these constituent phases [1]. In general, a cyclonic separator consists of a cylindrical section with a tangential inlet and two exits, one for heavy (dense) flow and the other for light (less dense) flow.

"The word cyclone implies an air pressure drop. Meteorologically, hurricanes, tornados and dust devils are cyclones. As such, defined regions of concentrated low air pressure are accompanied by swirling or rapidly revolving air currents". [3]

A cyclonic separator operates on a similar principle to that of a cyclone. Because fluid or feed is pumped in tangentially, the swirling motion creates a negative air-

pressure drop across the 'less dense' exit of the separator's cylinder. This then provides a pressure gradient. The higher pressure of air in the lower level of the cylinder is forced out through the 'less dense' exit, moving from a region of relative high pressure to low pressure. At the same time, the less dense phase will be forced out the overflow with the moving air stream, while the denser phase ('heavy' product) will move to the 'denser' exit [3].

Factors other than the individual phase characteristics (density etc.) which influence cyclonic separator operation include:

- Common diameter and length of the cylinder
- Common diameter and length of the cone (hydrocyclone)
- Flow rate at entry into the cylinder

Additional considerations include energy losses due to frictional forces on the cylinder sides, irregular air currents within the cylinder and turbulence at the tangential entry point which creates back pressure losses [3]. The inlet velocity is a key variable in the operation of a cyclonic separator. Therefore, inlet velocity should be low to minimize back pressure loss, and high for effective separation. This means that an important balance has to be struck according to the material in the system and the intended process [3].

Cyclonic separators are used in many different processes which include the cotton industry, grain processing, food processing, and chemical and mineral processing [3, 15]. In these various processes, the separation of solid and liquid particles from gas or liquid media is employed [15]. For solid – solid separation and solid – liquid separation in a liquid phase continuum, there are two main types of cyclonic separators used, these being: Hydrocyclones and Dense Medium Cyclones (Dense Media Separators) [15].

2.1.1 Hydrocyclones

Hydrocyclones are widely used in various processing industries for de-watering, and classifying according to a required particle size or for density separation. The reasons why hydrocyclones are so popular are because of their:

- High throughput
- Low maintenance
- Low operating costs
- Small physical size

Hydrocyclones are physically simple and robust. A typical hydrocyclone consists of three sections: a tangential inlet, a cylindrical section and a conical section. Figure 2.1.1 shows a diagram of a typical hydrocyclone. The tangential inlet is attached to the top of the cylindrical section. The conical section is then attached to the bottom of the cylindrical section. A vortex finder (overflow) is located centrally through the lid of the cylindrical section, and the apex (underflow) is located centrally at the base of the conical section of the hydrocyclone [9, 15].

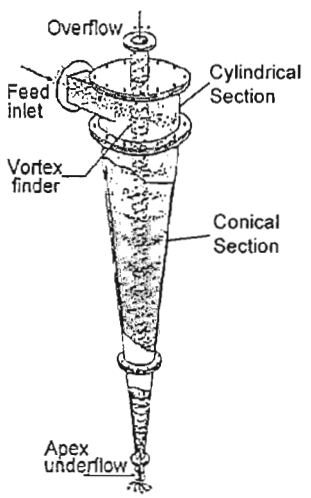

Figure 2.1.1: Diagram of a cyclone showing the different sections. [15]

The feed of particles are fed into the tangential inlet in the form of a pressurised slurry. The slurry is generally solid or liquid particles in a fluid medium. This slurry can then exit the hydrocyclone via either the apex or vortex. In the case of a hydrocyclone, the continuous fluid is water [15]. The design variables which influence the actual performance and efficiency of a hydrocyclone are the inlet and outlet diameters [9]. Because of the tangential entry of the slurry, an outer layer of liquid swirls downward until the conical section of the cyclone, where it then changes direction and moves upward. This causes what is known as a 'double helical flow' [9]. An air core of negative pressure and zero velocity then forms in the centre of the hydrocyclone. This air core will be discussed in much greater detail in a later section.

Because of the centrifugal force created by the tangential feed injection, the movement of solid particles, relative to that of the liquid is created. This relative motion depends on the size, shape, density and concentration of the solid particles, as well as on the density and viscosity of the fluid [8]. Therefore, larger and denser particles tend to move to the wall of the cyclone and spiral down and exit at the underflow or apex, while the smaller and less dense particles get sucked up by the air pressure and leave through the overflow. The liquid leaves through both exits and the volume split (of the liquid) is determined by the relative sizes of the apex and vortex and most importantly by the size (diameter) of the air core [15].

Separation efficiency of a hydrocyclone is measured as the relationship between the percentage of each particle size of feed exiting at the under flow, and is often used to represent the performance of the separator with regard to particle separation and classification [8]. One aspect which plays a fundamental role in good separation efficiency is uniform feed conditions with respect to solid concentration and particle size distribution [29]. Therefore in order to maintain uniform feed conditions, a control

strategy should be employed. This control strategy should be able to stabilize the operating state of the separator by controlling both the volume split of the particles and the feed pump speed. However, before it is possible to actually control the process, it is necessary to first look at and differentiate between the output values (which can be detected at the two separator exits) and the process state values (which characterize the interior conditions of the separator) of a hydrocyclone. These operating states have a couple of typical features, which can also be seen in figure 2.1.2:

- Sediment mass stored in the hydrocyclone
- Formation of an air core
- Shape of the underflow discharge [29]

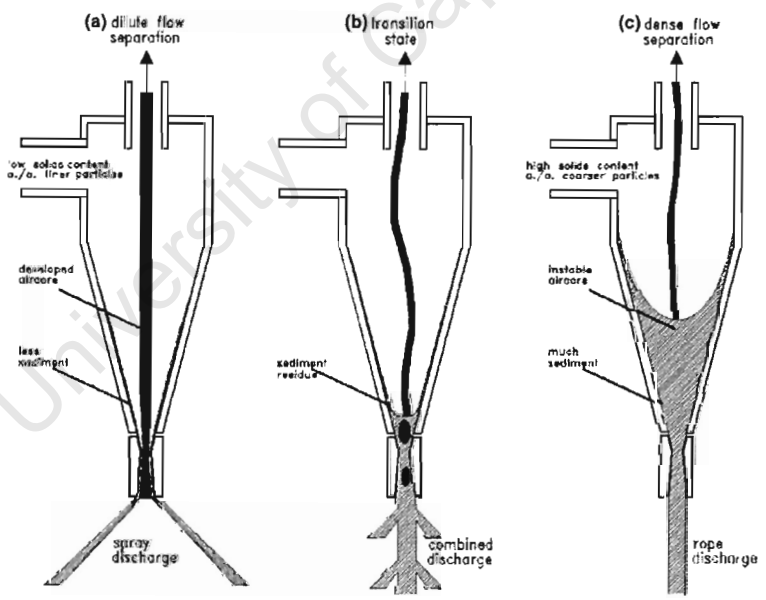

Figure 2.1.2: Operating states of a hydrocyclone. [29]

As can be seen above, there are three different operating states for any given hydrocyclone.

Dilute Flow Separation: Here, the hydrocyclone has a typical spray discharge at the underflow, and an air core that extends all the way from the vortex finder to the underflow can be observed. In terms of separation, the hydrocyclone presents high solids recoveries, but low solids concentrations, meaning that more fine particles will be swept into the underflow.

Dense Flow Separation: In this state, the hydrocyclone is characterized by a roping discharge at the underflow. The air core is not present the whole way through the separator and oscillates intensively. Here, more solids are kept in the conical section of the hydrocyclone and are partly forced to the overflow, resulting in a reduced solid recovery at the underflow. Therefore the advantage of this state is that there is a high solid content with less fine particles.

Transition State: This is an instable state with rapid changes between rope and spray discharge. Therefore, this state can show characteristics from both the above states, as well as a combination of the two states with respect to the shape of the underflow and the air core. The transition state shows remarkable separation effects and hence there is a lot of interest in monitoring this state in industry. [10, 29]

2.1.2 Dense Media Separators

Dense Media Separation takes place in a fluid medium. In the case of a Dense Media Separator (DMS), the continuous phase is a dense suspension of fine magnetite or ferrosilicon [15]. In a DMS the apparent density and viscosity of the dense medium can be controlled so as to allow selective separation of the solid particles on the basis of their size and specific gravity [15], where specific gravity is defined as the density of a material divided by the density of a standard reference material [3].

Separation is based on the competing radial forces acting on the particulate phases owing to centrifugal action and fluid drag [15].

DMS's operate in a very similar fashion to hydrocyclones and are used in various processing applications including separation of iron ore from siliceous gangue, coal from shale, diamonds from kimberlite and in a variety of plastic and metal materials recycling operations [15]. Of all these applications, it is specifically the diamond separation that interests the De Beers research group at UCT.

In this diamond separation process at De Beers, the diamond plant uses the difference in relative densities between the diamonds and host rock to separate the diamonds into a small parcel of high density material [40]. The initial feed is mixed into a suspension of finely ground ferrosilicon slurry. This mixture is then pumped or gravity fed into the separator which yields a concentrate made up of diamonds and high density material. The ferrosilicon is then recovered and re-used [40]. Figure 2.1.3 shows a picture of the type of DMS used in the diamond separation process.

The productivity of DMS's are very good, but the overall processes do require good control in order to prevent various losses due to small fluctuations in separator performance [15].

As with hydrocyclones, an air core is present during the operation of dense medium cyclones. Therefore it is now time to discuss this air core in greater detail.

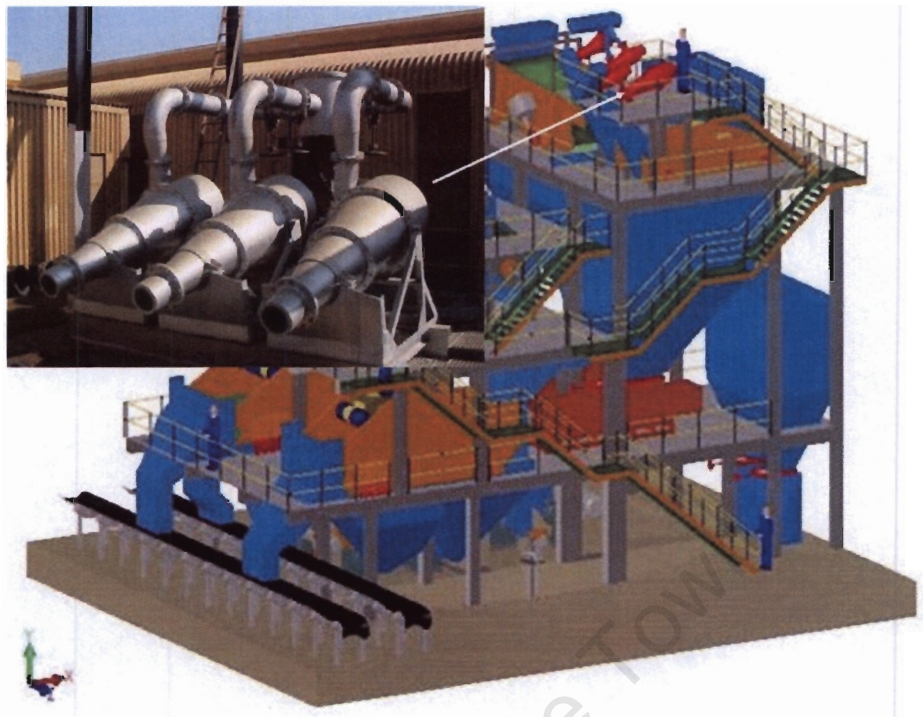

Figure 2.1.3: Picture of three DMS units which are used in the diamond separation process at De Beers.

2.1.3 The Air Core

Although cyclonic separators are simple in design, they are extremely complex with respect to the fluid mechanics governing their separation efficiency [23]. This is because of the nature of the environment that these devices work in. For example, the process slurries are mostly opaque and the cylinders are predominantly metal walled [23]. Therefore it has always been very difficult to understand and model the internal flows within these separation devices. If all the literature on these separation devices is actually considered, one will find that there are conflicting opinions regarding some of the characteristics of the flow field within cyclonic separators [8]. However, it is well known that inside a cyclonic separator, there is a three phase flow containing solids, liquid and air. As was mentioned previously, when the feed is injected tangentially, a pressure gradient is formed with negative air pressure at the centre of the separator.

Because of this an air core is formed and it is this air core, which is of particular interest.

The air core, with respect to its size and stability, is one of the least understood factors affecting the flow split of cyclonic separators. Therefore in many cases, researchers have tried to predict separator performance by using simple forms of dimensionless analysis and some have even excluded the presence of the air core when trying to describe the feed flow and particle transport [6, 16]. However many major institutions researching flow patterns of cyclonic separators have more recently acknowledged that the air core does play a major role in the performance of these devices [4, 5, 6, 13, 16, 27]. This has in turn lead to a general consensus that the size and stability of the air core are indeed major factors that influence the flow split and hence separator efficiency. Therefore there is a need to consider exactly what affects the air core itself, as well as how the air core can be linked to other output values which characterize separator performance.

Prediction of the air core size and shape is a complex task as there are many variables to consider. These variables include both the cyclone geometry and the operating conditions [5, 6, 15]. In terms of the operating conditions:

- If the feed flow rate into the cyclonic separator is increased, the air core diameter increases linearly and becomes stable after the feed pressure reaches a certain critical limit [6, 16, 23]. It has also been stated that once the air core is formed, even if there is a decrease in feed flow rate (below that of the critical rate for a stable core), the air core will persist [15]. Furthermore, it is also known that there is another critical limit where if the feed pressure is increased too much, the air core will decrease and collapse [5].

- In terms of the slurry viscosity, it has been concluded that an increase in it, causes a decrease in the size or diameter of the air core [6, 16, 23]. Therefore, if the slurry viscosity is too high, it will cause the air core to decay [6].

With cyclonic separators, the shape of the underflow discharge can tell us a great deal about their performance. It was also previously seen in the section 2.1.1 on hydrocyclones that the air core is indeed related to the type of underflow discharge. But in fact, the underflow discharge of a cyclonic separator is more of an effect than a cause of the air core [27]. A spray type discharge suggests that an air core exists, while a rope-type discharge suggests that an air core does not. Both these states are also related to slurry viscosity [16].

Now, in terms of the effects that the cyclone geometry has on the air core:

- It has been suggested that the diameter of the air core is influenced by the actual diameter of the cyclone [8].
- Both the diameters of the apex and the vortex finder affect the air core diameter. Furthermore it is said that the diameter of the air core is strongly dependant upon the apex diameter [14, 15] and that the difference between the air core diameter and apex diameter is very small [6].

Bustamente et al. (as stated in the work by Concha[7]) stated that there are ranges of ratio's (d_u/d_o) between the apex (d_u) and vortex (d_o) diameters that would yield either rope or spray discharge. The ranges are as follows:

- $d_u/d_o < 0.34$, underflow exhibits a rope discharge (resulting in no air core).

- $0.34 < d_u/d_o < 0.50$, underflow exhibits either rope or spray discharge, depending on pressure and other variables (therefore air core may or may not exist).
- $0.50 < d_u/d_o < 0.90$, underflow exhibits a spray discharge (resulting in an air core).

These values did differ slightly in Concha's [7] works. He used the following values:

- $d_u/d_o < 0.45$, underflow exhibits a rope discharge (resulting in no air core).
- $0.45 < d_u/d_o < 0.56$, underflow exhibits either rope or spray discharge depending on pressure and other variables (therefore air core may or may not exist).
- $0.56 < d_u/d_o$, underflow exhibits a spray discharge (resulting in an air core).

Now that what affects the air core has been reviewed, it is possible to look at how the air core behaves.

The air core is instable with respect to its size, shape and position because of the air-water boundary [6, 9]. This boundary can take on a sinusoidal shape and is caused by the high pressure gradient and its discontinuity at the interface, which creates pressure disturbances that grow rapidly with time and cause the shape and size of the air core to vary [6].

By many researchers, the air core is assumed to have a circular shape and be cylindrical along the separator length; whereas in practice, it has been shown that the air core is not always circular and is actually more conical in shape [6, 15, 23]. In fact, with respect to the air core not being a circular

shape, it is actually more useful to determine the size of the area that the air core occupies and use it as a measurement parameter instead [23].

In addition to this it has been found that the air core shifts off the axial centre of the separator for relatively low and high flow rates [16]. For large diameter hydrocyclones and DM cyclones (DMS), it was observed by Wood (as referenced in the work by Williams et al. [15]) that there was some 'rifling' in the air core shape, particularly near the vortex finder [15].

Therefore in light of the above research and fact that the air core's size and stability indicate the performance of a separator, it can be concluded that by monitoring the air core diameter or area and carefully controlling these aspects, the flow conditions and separation efficiency of cyclonic separators can be controlled and enhanced [6, 15].

2.2 Process Tomography

The word 'tomography' originated from the Greek word 'tomos', meaning 'to slice', and 'graph', meaning 'image' [42].

Tomography is defined in the Oxford Dictionary [46] as: "Radiology in which an image of a predetermined plane in the body or other object is obtained by rotating the detector and the source of radiation in such a way that points outside the plane give a blurred image. Also in extended use, any analogous technique using other forms of radiation."

From all its descriptions, tomography is often perceived as a medical imaging tool, whereas it is actually not restricted to medical purposes only, it is also used in industry. Therefore this field of application is either known as Industrial Process Tomography (IPT) or just Process Tomography (PT) [42].

Tomography and its related instrumentation developed from round the 1950's, and has since led to the widespread availability of various body scanner instrumentation for medicinal purposes. Nowadays, with industrial demand to use resources more efficiently and to meet certain production requirements with respect to quality and reduced environmental emissions, tomography, with its non-invasive manner of imaging, has developed into a reliable tool for many industrial process applications [39].

During the 1980s process tomography evolved a great deal. To be specific, it was during the mid-1980s that the work commenced that has now led to the present generation of PT systems [39].

Tomography involves taking measurements around the border of either a vessel or patient (in the medical case). These measurements are then manipulated in various

manners in order to determine exactly what is happening inside the vessel or patient [41].

The most well known form of tomography is that of computerized axial tomography (CAT). Also referred as CAT scanning, this technique is used in medicine and is expensive. However process tomography requires cheaper, faster and more robust forms of instrumentation to measure the fast changing, chemically aggressive, access limited concentrations and the movement of components inside the required process [39, 41, 44]. These measurements are then reconstructed to give either volume or void fraction predictions, or two- or three-dimensional images, providing reliable information used to monitor processes and improve quality, efficiency and the overall control of the process [39, 44].

2.2.1 A Typical Tomography System

A typical tomographic system involves getting the necessary measurement signals from the sensors located on the boundary of the object of interest (such as a pipeline or process vessel). These measurements then provide information with respect to the nature and distribution of components inside the sensing zone [39]. Most of the tomography schemes available today are concerned with reconstructing the measurement information into some form of images.

A tomography system consists of a few basic components as follows, and can be seen in figure 2.2.1:

- Sensors
- Input signal/data control and data acquisition system
- PC host system (with graphic display monitor)

The sensors, and input signal/data control and data acquisition system embody the hardware. The PC host system is software based and is used for signal reconstruction, interpretation, and for the generation of output control signals to process hardware. Lastly, the graphic display monitor is used to display images and other information linked to the measured process [39].

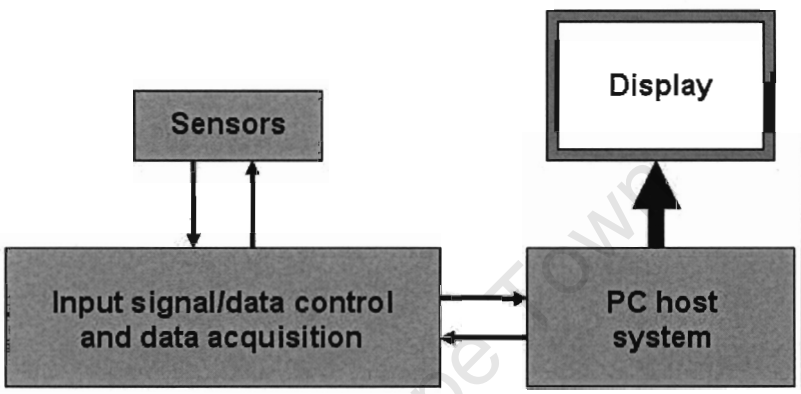

Figure 2.2.1: The basic components of a tomography system

Obtaining a high quality image or volume/void fraction prediction is only the first stage of input information for a process engineer. The actual goal is the accurate interpretation of the image or information in order to make the overall process run more efficiently.

As has been mentioned previously, one of the fundamental requirements for a tomography system is that it should be non-invasive (meaning that it should not necessitate penetration of the process vessels walls, by means of probes etc.) and non-intrusive (meaning it should not disturb the nature of the examined process). However it is not always possible to meet both of the above requirements, but the latter can generally be satisfied. [39]

The sensors are the heart of any tomographic system. There are a variety of different sensing methods based on measurements of transmission, diffraction or electrical phenomena [39, 43]. Some of these include

infared, optical, X-ray and Gamma-ray tomographic systems, positron emission tomography (PET), magnetic resonance imaging (MRI), sonic or ultrasonic tomographic systems, and electrical tomography (resistance, capacitance and impedance). These techniques all have their advantages, disadvantages and limitations. The choice of a particular technique is usually dictated by many of the following factors: physical properties of the flow, the desired spatial and temporal resolution of imaging, cost of the equipment, its physical dimensions, human resources needed to operate it, and potential hazards to the personnel involved (e.g. radiation). [42]

Table 2.2.1 below shows some of the sensing methods used to monitor cyclonic separators.

Table 2.2.1: Some of the sensing techniques used for monitoring hydrocyclone performance [12, 39]

Technique	Sensing Modality	Sensor Location	Measurement	Spatial Resolution
Tomography	X-ray	External, around the body	Internal density profile	1%
	Electrical resistance	Internal, around the cylindrical and conical sections	Air core shape and size, internal density profile	10%
	Electrical capacitance	External, around the discharge spray	Discharge profile and spray angle	10%
Video Imaging	Optical emission	External, via: – vortex finder observing inner air core – at underflow discharge spray	Air core shape and size, internal flow pattern, spray angle of the discharge, both average and fluctuation	
Mechanical	Paddles	External, around the discharge spray	Spray angle of the discharge	
	Calipers	External, around the discharge spray Internal, around the central axis	Spray angle of the discharge Air core shape and size	
Acoustic monitoring	Acoustic emission (active) Acoustic emission (passive)	External, around the discharge spray External, on the hydrocyclone body	Spray angle of the discharge Feed properties and operating parameters	3%
Ultrasound	Ultrasonic transducers	External, around the cylindrical section of the hydrocyclone	Air core shape and size	

Because of the task at hand and the fact that the De Beers research group is particularly interested in tomography schemes used for measuring the

operating states of cyclonic separators with respect to the air core, only the related tomography schemes shall be reviewed in this paper. Many investigations of the air core have been made by using visual observations and laser Doppler velocimetry in glass walled hydrocyclones treating water [15]. In terms of mechanical measurements made, Wood (as referenced by Williams et al. [15]) inserted measurement calipers on an axially mounted rod down into the air vortex of a DM cyclone. However it is the internal electrical measurements that are of particular interest to the research group. This involves looking at both ultrasound tomography and electrical resistance tomography.

2.2.2 Ultrasound Process Tomography

As the slurries in cyclones are invariably water-based suspensions, ultrasound should theoretically provide a relatively easy manner of monitoring the air core size, shape and position [13]. Schlaberg et al. [13] stated that if the air core remained stationary along the centre axis of the cyclone, it would be possible to fit a single transducer to determine the air core size. However, because the air core has an oscillatory nature, it is necessary to fit a number of transducers around a hydrocyclone cylinder. By doing this one can take measurements from multiple views around the cyclone perimeter and thus determine the size and position of the air core [13].

Ultrasound tomography (UST), also known as reflection mode tomography has been well studied in the medical field, and as a result has a wide range of applications [12]. UST makes use of transducers which operate in pulse-echo mode, and detect the changes in acoustic impedance (Z) which are closely related to the density (ρ) of a media, where:

$$Z = \rho c \qquad (c \text{ is the speed of sound}) \qquad (2.2.1)$$

Because of this difference (between the fluid medium and that of the target or targets) and the fact that air cannot propagate ultrasonic waves in the megahertz region, only the time-of-flight (TOF) data from the echo is used in the image reconstruction process [11].

A typical UST system can be seen in figure 2.2.2 and consists of the following hardware:

- Sensors: Ultrasonic Transducers
- Input signal/data control and data acquisition system
- Host computer (for processing, image reconstruction and image display)

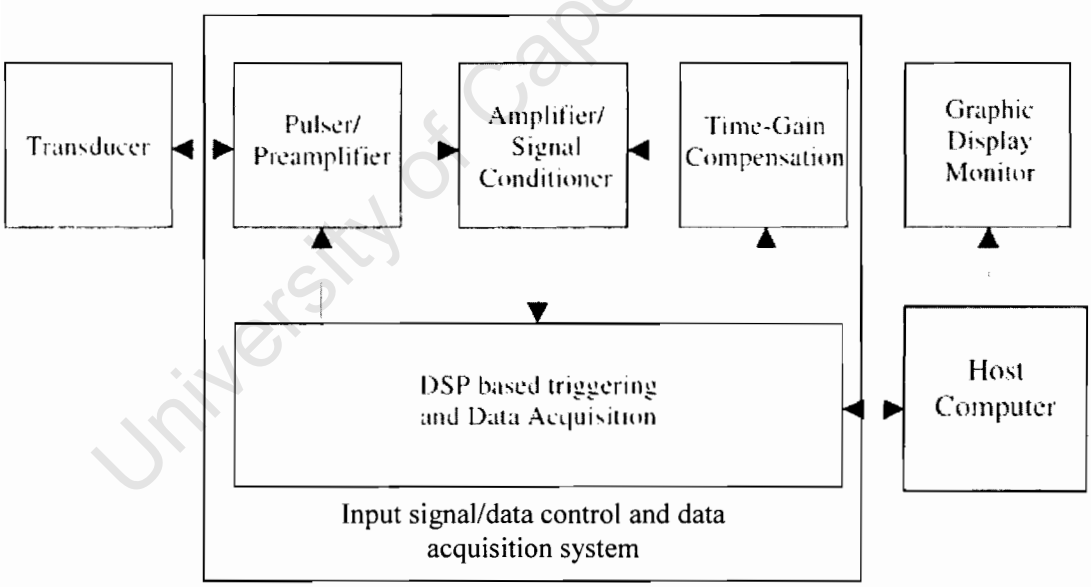

Figure 2.2.2: Block diagram of a typical UST system.

A tomography system such as the one above has been fitted to a hydrocyclone to observe the air core [13, 14]. In both cases the hardware used was exactly the same.

The cyclone was fitted with 16 ultrasonic transducers (figure 2.2.3) and a close-by set of pulser/preamplifier circuits. These were then attached to an electronic system containing time gain controlled amplifiers and a digital signal processor (DSP) which sends the converted data to a host computer. The data is then processed by the host computer and an image of the air core is reconstructed and displayed on the graphic display monitor. [13]

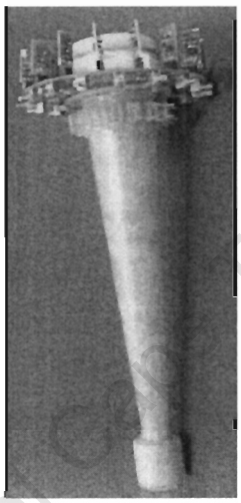

Figure 2.2.3: Hydrocyclone fitted with ultrasonic transducers. [13]

The data that is sent from the data acquisition system to the host computer is in the form of emitter, receiver and TOF data packets. For example, if an echo is detected, the index of the pulse originating transducer and the index of the detecting sensor, together with the amount of time it took for the pulse to get from one to the other (TOF) are transmitted to the host computer. [13]

Now that the data has been sent to the host computer, the host can process the data and do the image reconstruction.

There are a few different methods of image reconstruction that exist and have been used to find the air core properties.

Schlaberg et al. [12, 13] used a back-projection image reconstruction method. In this method the emitter, receiver, TOF and the fan angle (of the transducer) data are used to do the image reconstruction. By superimposing arcs along the path where an object may be located, Schlaberg et al. were able to generate an image where the boundary of the air core is highlighted by the intersection of all the arcs [13].

The images that were obtained by this method resulted in an image resolution of 50 × 50 pixels, where one pixel corresponds to 1mm. Figure 2.2.4 shows one of the reconstructed images with a partial subset of operating sensors.

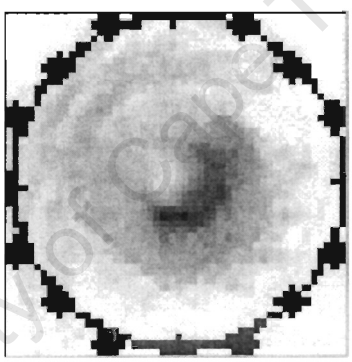

Figure 2.2.4: Reconstructed image with a partially operating UST sensor. Here, the back-projection image reconstruction technique is used. The image has a resolution of 50 × 50 pixels, where one pixel corresponds to 1mm [13]

The hardware for above system is capable of running at 200 frames per second; however, the image reconstruction slowed the system down and it was only possible to display 6 images per second. The host computer used was a 266MHz PC, which by today's standards is extremely slow. Therefore much faster image reconstruction would now be possible.

Podd et al. [14] stated that the back-projection reconstruction technique yields poor resolution images and as a result of this, it is not possible to determine an accurate air core diameter. Therefore a model-based parametric reconstruction technique should rather be used. With this technique, although the accuracy of the individual echo positions from the sensors was 1mm, by means of statistical methods, sub-millimeter accuracy was obtained.

The final method of image reconstruction is that of a Hough transform. This method uses an algorithm which processes the pixel field with respect to the parameters of radius and circle centre coordinates and seeks a high correlation between the parameters and the image [21]. This form of image reconstruction is said to be a fairly robust method with respect to noise or sensor failure. An image using this reconstruction technique can be seen in figure 2.2.5.

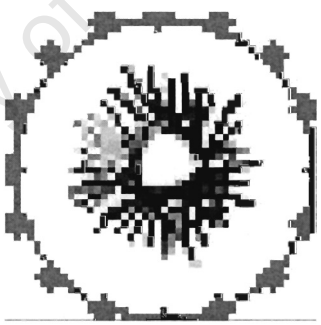

Figure 2.2.5: Pixilated reflection-mode ultrasound tomogram of a hydrocyclone [21].

Although these systems are successful when used with a hydrocyclone containing water, they may not have similar results when used with dense slurry which in addition could contain heavier solid particles, as these particles could cause scattering of the ultrasonic waves, resulting in a bad and inaccurate image reconstruction.

2.2.3 Electrical Impedance Tomography

During the mid-1980's, many scientists involved in the medical world began to realize the potential of electrical impedance tomography (EIT). This was because it was a safe, low cost method of imaging the human body. Because of EIT's potential, many institutions took interest and began research in the field. The success of this early work triggered the start-up of an European Union (EU) program in 1988 which coordinated activity with respect to EIT for medical use, and is still active today [39]. It was during this same year that the University of Manchester Institute of Science and Technology (UMIST) started on the development of EIT systems for the imaging of process vessels containing electrically conducting fluids [39]. Because of the fact that medical EIT and process EIT have some common problems, and because so much research was being done on medical EIT systems, much progress was made with process EIT. It must also be stated that although there are some common issues between the medical and process EIT systems, there are also some differences:

- Medical EIT aims to measure the locations of objects in space

Whereas

- Process EIT is required to measure the location of objects, velocity of movement, and the internal density profiles of a medium.

[39]

Nowadays EIT is being researched at many large institutions worldwide and as a result, much progress is being made with respect to both the

hardware and the image reconstruction software. Some of the hardware is even capable of running up to speeds of 1000 frames per second [32, 34]. Electrical impedance tomography is referred to as an ill-conditioned problem, and therefore systems designers need to have a quantitative knowledge of the sensitivity of the reconstruction with respect to the measurement noise present [18].

The aim of an EIT system is to recover the internal structure of a different phase or object from within a process vessel via means of surface measurements [24, 25]. These surface measurements are obtained from a number of electrodes placed around the periphery of the process vessel. These electrodes may or may not be in contact with medium inside the process vessel, depending on both the medium properties and measurement strategy.

EIT is essentially a two step process, where the sensors provide the data which characterize the electrical response of a medium due to arbitrary excitations, and then the distribution of the electrical properties is then reconstructed and displayed in some form [18]. At UCT, Capindissa [27] referred to EIT as a dual modality measurement system using both the permittivity (used in capacitance tomography) and conductivity (used in resistance tomography) measurements to do image reconstruction. This is not necessarily the case. Lemonnier et al. [18] states that there exists both resistive EIT and capacitive EIT.

Resistive EIT, also referred to as electrical resistance tomography (ERT) is used when the fluid medium is conducting, whereas capacitive EIT is used mainly when the fluid medium is non-conductive and has dielectric properties. Capacitive EIT is also known as electrical capacitance tomography (ECT).

As can be seen in table 2.2.1 on page 21, ECT is used externally around the discharge spray to measure a cyclonic separator's performance by the discharge profile and spray angle, whereas ERT measures (internally) the air core size and shape, and the separator's internal density profile. Therefore it is ERT that is of interest to the UCT De Beers group with respect to this research project.

An ERT system is said to be made up out of three key elements: electrodes, a data collection system, and an image/data processing algorithm [36]. These elements all fit into the general description of a process tomography system in the following way:

- The electrodes are the sensors
- The data collection system is part of the input signal/data control and data acquisition system
- The image/data processing algorithm takes place within the PC host system and the results are displayed on the graphics display monitor.

Each of these three elements can be broken down further into their constituent parts. Figure 2.2.6 shows a block diagram of a typical ERT system.

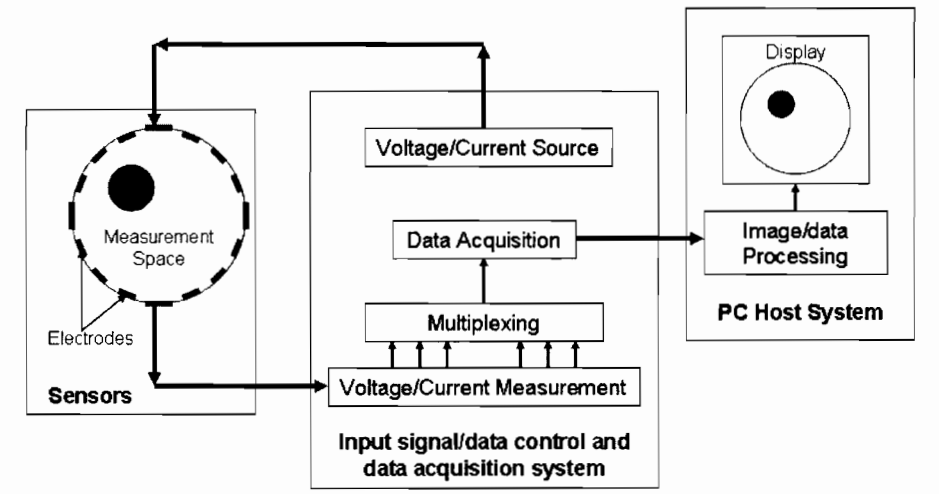

Figure 2.2.6: A block diagram showing the key elements and their constituent parts of a typical ERT system. The arrows represent the signal paths.

Voltage or Current Source:

In an ERT system there exists the choice of either injecting a current into the measurement space and measuring the resultant voltage, or applying a voltage and measuring the resultant current [28]. There are various factors that have to be considered when this decision is made. These factors will be dealt with in a later section.

Voltage or Current Measurement:

In ERT one is trying to find the conductivity distribution in the measurement space and since V = IR, if current has been injected the resultant voltage must be measured. If a voltage has been applied, then the resultant current must be measured.

Multiplexing:

In order to obtain an image from within the measurement space, one needs to place a number of equally spaced electrodes around the periphery of the process vessel. The resolution of this image increases with an increase in

the number of electrodes, therefore one tries to place as many electrodes around the vessel as is possible. This means that there is normally a large amount of data (over 100 measurement readings for a 16-electrode system) that needs to be captured, and because it would be impractical to read this data in parallel, some form of multiplexing is needed to capture each frame. [28]

Data Acquisition:

Most ERT systems nowadays make use of data acquisition modules to capture the data used to reconstruct a single frame. This data acquisition card has to be synchronized with the multiplexer.

Image/data Processing:

Once an entire frame of data has been captured by the ERT system, it is transferred to the host PC. Here the data is manipulated in various ways in order to get it ready for processing. These pre-processing steps often include tasks like normalization and/or calibration. Once this preprocessing is complete, the data is then fed into some form of image reconstruction algorithm or process controller via some intelligent system [28].

Display:

In most ERT systems, the output of the data processing is an image displaying the spatial conductivity distribution of the measurement space. This image can then be analyzed by the human eye and an informed decision or conclusion can then be made. However, with the emergence of machine vision and artificial intelligence, there is no need for an image to be reconstructed. Instead the data can be processed and a resultant decision or conclusion made without the reconstruction of an image. [28]

2.2.4 Multi-Modality Tomography and Data Fusion in Multi-Modality Tomography

A multi modality tomography system uses two or more different sensing techniques in order to measure and locate different phases or objects within the measurement space (a process vessel). By fitting different modality systems to a process, it enables the process engineer to take advantage of the best features from each system and combine them in some form to get a much better and more accurate resultant tomogram [22]. Multi-modality tomography is used in many different disciplines. Some of these disciplines include: medicine, robotics, machine vision, remote sensing and non-destructive testing [22]. Multi modality tomography has also been used in various process applications as well.

Teague [20], Giannopoulos [26] and Capindissa [27] all used an electrical impedance system that took both resistance and capacitance readings. The EIT system was originally based on an electrical capacitance system designed by Smit [19]. Teague used the system to image, make volume fraction predictions and differentiate between air and gravel pockets in an air lift. Giannopoulos used the same system Teague used, but used sine wave excitations instead of square wave excitation input signals in order to make the EIT system results more accurate. In Capindissa's case, he used the EIT system to image and make volume fraction predictions for an air core within a hydrocyclone.

In another hydrocyclone application, Williams et al. [22] fused data from an ERT and a reflection mode ultrasound tomography system. In this same paper, he stated that it would also be possible to combine these two modalities with X-ray tomography.

Ultimately, in multi-modality tomography, data is fused to give a single final result. Data fusion is defined as "the assimilation of information from different modalities" [22]. The aim of data fusion is to use different sensing techniques which provide complimentary information on the process, so that each technique yields a significant contribution.

In data fusion, there are various levels that the process can be performed at, these being:

- Signal Level: the signals from the measurements are fused
- Image Level: pixel values or weights of other image components are fused
- Feature Level: image features (e.g. boundaries) are fused [22]

Often data is fused at 'signal level' so that the greatest accuracy can be achieved. This is because when signal level fusion is performed, there is no information loss due to reconstruction or feature extraction. However, with signal level fusion, all the different signals must be transferred to a central processor which can cause a bottleneck [22].

It was mentioned earlier that Williams et al. [22] made use of ERT and UST to measure the radius of a hydrocyclone air core. In fact, they actually used signal level fusion. Here the potential difference measurements from ERT and the time-of-flight measurement from UST were parameterized and the images were represented as parametric models. They also stated that it would be possible to use reconstruction methods to give pixilated tomograms and hence proceed to an image fusion level. The only problem with this approach would be that extra work would have to be done to first derive a common pixellisation [22]. Therefore only feature level fusion is left. With respect to this it is believed that there are many advantages, these being that at feature level:

- There is no need to standardize reconstruction procedures or image format.
- Distributed processing is facilitated at each modality unit.
- The amount of information to be transmitted to a central processor unit can be reduced. [22]

Therefore it can be seen that for the case of a hydrocyclone data fusion can be performed at any level, and with various sensing techniques [27, 22]. This means that one needs to consider the speed of processing required by the application, and exactly what measurement protocol is being followed [22].

2.2.5 Time Domain Multiplexing vs. Frequency Domain Multiplexing

In an EIT system, the input current/voltage needs to be injected into the measurement space from one or two of the electrodes and then the resultant voltage/current can be measured on the remaining electrodes. In fact all the electrodes in the measurement space need to get a turn to inject the signal, therefore a signal injection method is required. There are two methods for this: Time Domain Multiplexing (TDM) and Frequency Domain Multiplexing (FDM).

Time Domain Multiplexing

Almost all EIT systems use TDM to inject and measure a signal from within the measurement space. In TDM, a single signal with a fixed frequency is injected through one or two (in most cases two) of the electrodes and the resultant signal measured on the remaining electrodes. Figure 2.2.7 shows exactly how the TDM scheme functions.

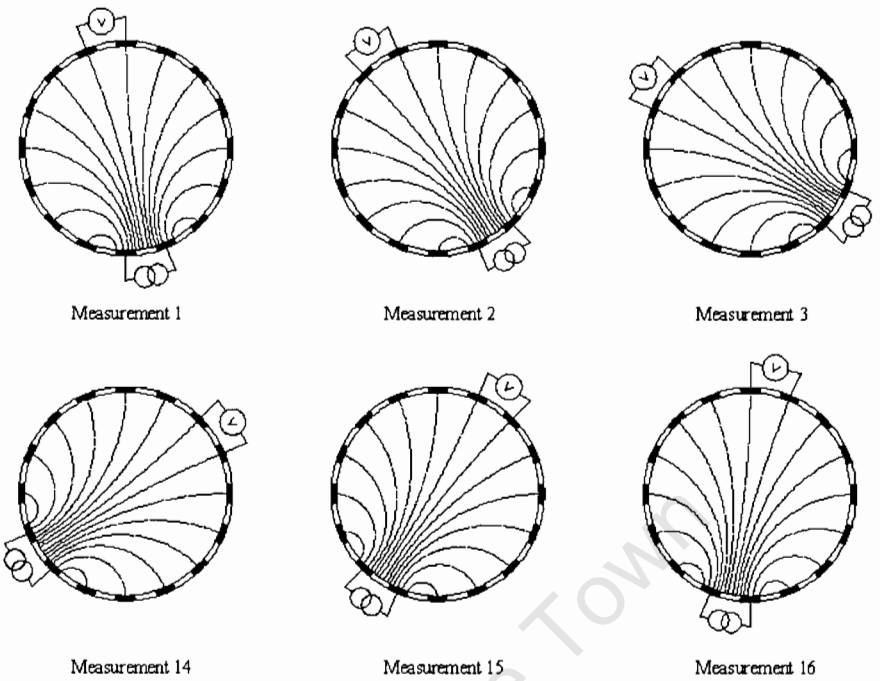

Figure 2.2.7: Diagram illustrating the time domain multiplexing scheme.

The input signal is then shifted to the next electrode(s) and the remaining electrodes measure the resultant signals. This continues until every electrode or pair of electrodes has had the chance to inject the input signal into the measurement space.

It can be said that one of the drawbacks from a TDM system is that one frame of data requires the sequential switching of the signal source between all the electrodes [28]. Therefore the finite amount of time between switching electrodes (small as it may be) means that it is assumed that the medium is stationary during this time. Although the errors introduced by this assumption are insignificant in static situations, they can become much more significant in a dynamic situation where the medium is moving or changing very rapidly. Therefore a TDM system is ultimately limited by the speed at which signals can be switched between the electrodes. However there are now TDM ERT systems capable of measuring up to 1000 frames per second [33].

Frequency Domain Multiplexing

Frequency domain multiplexing has a set number of dedicated transmitters and receivers. Therefore all the transmitters transmit different frequency input signals at the same time, and each receiver then receives all the different input signals at once. In a 16-electrode system, there will be eight transmitters and eight receivers. The eight transmitters will each inject a signal with a frequency that is different to the remaining seven transmitters. This means that at any instant, there are eight (different frequency) input signals in the measurement space. Now, each of the eight receiver electrodes will receive eight (different frequency) output signals. In a FDM EIT system with N electrodes, one can produce $(N/2)^2$ independent measurements. Therefore for a 16-electrode system, one will be able to produce 64 independent measurements. Figure 2.2.8 shows an example of a 16-electrode FDM EIT system.

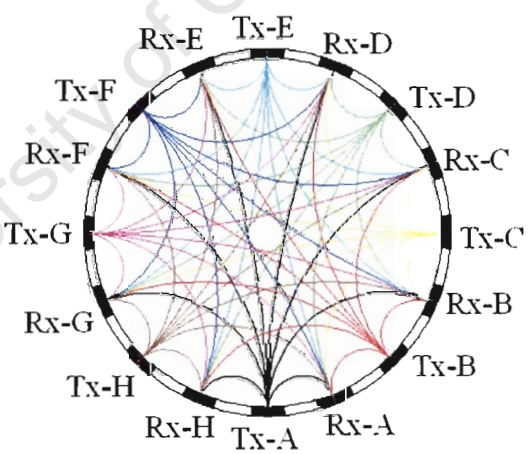

Figure 2.2.8: A diagram illustrating a 16-electrode FDM EIT scheme. Transmitters are marked Tx and receivers are marked Rx.

One of the major disadvantages of a FDM EIT system is that in order to obtain a resolution that is the same as a TDM EIT system, more electrodes are needed. Although this is the case, one major advantage is that theoretically a FDM system should be able to capture a single frame of

data faster, as no switching between the electrodes is required. Because of this advantage, FDM has been the data collection technique used by the De Beers research group prior to the author's involvement. It has thus far proved to be a very effective tomographic method and the results are documented in [20, 26, 27, 28].

2.2.6 Voltage Driving vs. Current Injection

It was previously mentioned in section 2.2.3 that when designing an EIT system, one can either inject current into the measurement space and measure the resultant voltage, or, one can apply a voltage and measure the resultant current. The single most significant parameter to consider when making this choice is the output impedance of the driver and the input impedance of the receiver [28]. If the driver has a high input impedance like that of a current source, then the contact impedance (between the electrode and electrolyte) is less significant than for the case of a voltage source, which would result in a low input impedance. Likewise, a voltmeter has a high input impedance – therefore creating a negligible contact impedance on the on the receiver, while an ammeter has a low input impedance, and hence creates a more significant contact impedance.

Another factor which plays a role in the design of the system with respect to the input source is the ease with which the input driver can be implemented [28]. A voltage source is much easier to realize than a current source. In addition to this, if the system is a FDM system and a current source is used, complex demodulation circuitry is required. For these final two reasons, when Teague [20] started the project, he decided that voltage drivers and current receivers should be used. Further justification for Teague's choice originated from the type of flows the De Beers research group are dealing with. This is because it has been shown that if the input signal has a sufficiently high excitation frequency and if

the flow only has one conducting phase, and then the contact impedance becomes negligible [20].

Although the FDM systems should theoretically have speed advantages, in industry TDM systems are more widely used. These TDM systems predominantly use current injection and voltage measurement. With current injection, the current can either be induced by an AC signal or a pulsed DC signal, of which the latter is now being used in systems capable of measuring up to 1000 frames per second [32, 33, 34]. Nowadays there are many different current injection patterns such as neighboring (adjacent) method, cross method, opposite method, and multi-reference method, of which it is known that the multi-reference method is the best [37].

In the adjacent method, currents are applied through two neighboring electrodes and then the voltages are measured at all the remaining pairs of adjacent electrodes. This method obtains good sensitivity at the periphery of the measurement space as it forces most of the current to travel near the peripheral electrodes [38].

In the opposite method, currents are injected through diametrically opposed electrodes and the resultant voltages are measured with respect to the reference at all the electrodes. With this method better sensitivity for targets far from the electrodes is achieved [38].

In the multi-reference method, predetermined current patterns are injected through all the electrodes simultaneously and at the same time activated boundary voltages are measured on the electrodes simultaneously [37]. This method uses various current amplitudes in each of many current sources to make the current distribution more uniform throughout the

measurement space [38]. In this method a trigonometric current pattern is often used [38].

In addition to the various current patterns used in EIT, it has now become possible to inject current between layers in multi-plane EIT systems. Some of the electrode combinations possible are as follows: injection on one layer and measurement on the same layer; injection on one layer and measurement on any layer; injection between two layers and measurement on the any layer (of the multi-plane electrode vessel); and finally injection between two layers and measure any adjacent pair between two layers.

As can be seen, there are advantages and disadvantages to both current and voltage injection. However, current injection is more widely used.

2.2.7 Reconstruction Techniques

It has already been said in chapter 2.2.3 that one of the three key elements of an electrical impedance tomography system is a good data/image processing algorithm or reconstruction technique. It should also be emphasized that the final output from this reconstruction technique need not be an image. In most cases an image is advantageous, as it can help determine system performance and can prove to be very useful when training neural networks or other computational intelligence. Nowadays there are a number of different reconstruction techniques for process tomography systems.

For ultrasound process tomography systems, various techniques have been used. These include the back-projection technique, the model-based parametric reconstruction technique, and the Hough transform. All of these techniques have already been discussed in section 2.2.2 and a result

will not be discussed here. If a more complete explanation is needed, one can refer to references [11, 12, 13, 14].

For electrical impedance tomography there are also a number of different reconstruction techniques or algorithms used. In the previous decade, most reconstruction algorithms were based on a simple back-projection technique [36]. Linear back projection does have speed advantages [21], but because the technique has a very limited accuracy, most researchers now use the more conventional modified Newton-Raphson (mNR) method. There is also the conjugate gradients (SCG) method, which has an improved accuracy because it doesn't use conventional regularization and hence minimizes the artificial errors introduced by the regularization processing [36]. Other methods also include that of parametric modeling [21], Kalman filter and its variations [30], Neural Networks and Kernel Ridge Regression [28].

The methods that are going to be discussed in more detail in this paper are that of the conventional mNR, Parametric Modeling and Neural Networks.

2.3 Conventional Imaging vs. Parametric Modeling vs. Neural Networks

Once data has been captured from the measurement space, it is then sent to the host PC for processing. Here the data is fed into an algorithm and some type of output is produced. In most cases the output is an image. This is because an image helps humans understand exactly what is going on inside the process vessel. In the case of ERT, the image produced takes the form of a spatial conductivity map of the measurement space. In this section the author will review three different reconstruction techniques: Conventional EIT imaging, Parametric Modeling and Neural Networks.

2.3.1 Conventional EIT Imaging

It has been stated that the most popular type of conventional imaging for an EIT system is that of the modified Newton-Raphson method [28]. This method has been described by Hua and Woo [47] as being "one of the most theoretically sound algorithms".

The modified Newton-Raphson (mNR) is a numerical minimization method which is used to search for the conductivity distribution which minimizes the difference between the measured potentials and the computed potentials (those obtained by means of the finite element method) [25].

Mathematically, conventional reconstruction methods for EIT are composed of both a 'forward problem' and an 'inverse problem'. In the following summarized explanation of the conventional reconstruction method, where a particular paper has been specifically drawn from, it is cited in normal fashion; elsewhere the explanation follows that of Goldswain [28].

The Forward Problem

The forward problem obtains the voltage distribution subject to the assumed resistivity distribution [37]. Therefore, when electrical currents are injected into the measurement space through the electrodes on the boundary $\partial\Omega$ of the measurement space and the resistivity distribution ρ is known over the measurement space Ω, then the electric field within this region can be described by Poisson's equation:

$$\nabla \cdot \rho^{-1} \nabla V = f \tag{2.3.1}$$

with boundary conditions

$$V = V_0 \text{ on } \partial\Omega \tag{2.3.2}$$

$$\rho^{-1} \partial V / \partial n = J_0 \text{ on } \partial\Omega \tag{2.3.3}$$

where f = the impressed current source distributions within the measurement space. V_0 and J_0 are the voltage and current density respectively, at the boundary. This equation can be used for both the two-dimensional and three-dimensional case. Now, because no current source exists within the measurement space, $f = 0$ and equation 2.3.1 then becomes:

$$\nabla \cdot \rho^{-1} \nabla V = 0 \tag{2.3.4}$$

and the potential V can be determined. This equation is known as the 'governing equation'.

Now, because the equation cannot be solved analytically, it has to be solved numerically with a method such as the Finite Element Method (FEM). The FEM is a method commonly used for solving partial differential equations (PDE's) and achieves this by changing the calculus problem of the equation into a linear system of algebraic equations.

This is done by means of dividing the domain on which the solution exists into a finite number of elements [30, 37].

Dividing the domain into elements is also known as discretisation of the domain or meshing. It is the first step in FEM and is accomplished by systematically defining a number of nodes in the region. These nodes are then numbered. Each element in the domain has nodes at each corner and when the nodes are all joined, a mesh-grid is formed. It is assumed that that the conductivity distribution is constant within each element [34]. An example of an FEM mesh showing the individual elements with the nodes at each corner can be seen in figure 2.3.1.

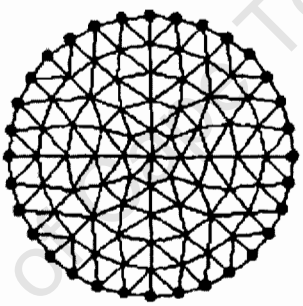

Figure 2.3.1: Diagram illustrating an example of an FEM mesh.

When the final image is taken into consideration, each of these elements can actually be considered as pixels. For a detailed explanation on node numbering and matrix assembly refer to [28].

The Inverse Problem

The inverse problem reconstructs the resistivity distribution with respect to the measured boundary voltages. In general, conventional reconstruction algorithms seek to find the inverse of a so-called 'Sensitivity matrix' or 'Jacobian matrix'. This matrix then describes the relation of the changes in boundary voltages or currents with respect to each pixel's resistivity. Because the modified Newton-Raphson method is

the most popular reconstruction method, it will be the only method discussed here.

Newton-Raphson Method

The Newton-Raphson algorithm is an iterative reconstruction algorithm which seeks to minimize the error between the measured boundary voltages or currents and those predicted by the forward solver:

$$\Phi(\sigma) = \frac{1}{2}(f(\sigma) - f_0)^T (f(\sigma) - f_0) \tag{2.3.5}$$

where $f(\sigma)$ is the estimated current or voltage response for a given conductivity distribution σ, and f_0 is the measured response to the conductivity distribution. Now, in order to minimize the error Φ, the derivative Φ' is set to zero, giving:

$$\Phi'(\sigma) = (f'(\sigma))^T (f(\sigma) - f_0) = 0 \tag{2.3.6}$$

Here, $f'(\sigma)$ is known as the 'Jacobian matrix'.

A Taylor series expansion is then taken from the derivative Φ' and all the insignificant terms are cancelled. This yields the update equation which informs on how to update the conductivity distribution:

$$\Delta\sigma^k = -\left[f'(\sigma^k)^T f'(\sigma^k)\right]^{-1}\left[f'(\sigma^k)\right]^T\left[f(\sigma^k) - f_0\right] \tag{2.3.7}$$

where k is the conductivity element number.

In an EIT system, large changes in conductivity towards the centre of the measurement space result in small changes in the captured boundary measurements. The small changes near the boundary can easily be swamped by noise and as a result the system will become insensitive to changes towards the centre. Therefore in reconstruction there is a need for

smoothing or regularization. For a more detailed look at regularization refer to [28]. Although the Newton-Raphson method is an iterative algorithm, by pre-computing some terms and making various modifications to the basic algorithm, visually accurate real-time results may even be achieved with a single-iteration algorithm [33].

2.3.2 Parametric Modelling

The more conventional methods of image reconstruction deal with pixel based tomography. In a pixel-based tomography system the measurement data is reconstructed and visualized first and then an interpretation is made [21]. Figure 2.3.2 illustrates the pixel-based approach. The problems that this pixel-based reconstruction method faces are that with high noise levels the tomogram may become unreliable, and the overall reconstruction speed is reduced because of the iterative approach [21].

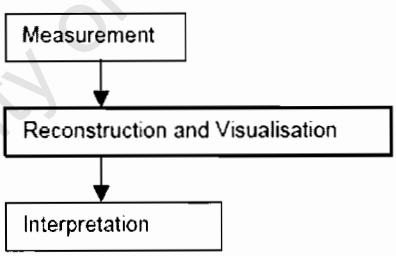

Figure 2.3.2: Pixel-based approach for EIT.

Therefore a better approach for control purposes is that of parametric modelling. There is not nearly as much literature available on the parametric modelling reconstruction technique as there is on conventional reconstruction methods. Therefore there is not as much information available. Where information has specifically been drawn from another paper, it will be cited in the normal manner; elsewhere all the rest is cited from [21].

In EIT, a tomogram can be built up from basis functions that either suit the geometry of the problem, or the geometry of features (e.g. boundaries). The weights of these functions are known as parameters and the determination of these parameters is then known as the parameter identification problem. In practice the subset of the basis functions is used to reduce the number of parameters to be determined.

The basic idea of the parametric approach is to include all the features of the process that the tomogram is intended to clarify. Therefore the same parameters that are identified during reconstruction, are the ones required for image interpretation. It then follows that if the number of parameters is small, then the reconstruction problem will be better posed and interpretation will be accomplished more efficiently. Figure 2.3.3 illustrates the Parametric-model approach.

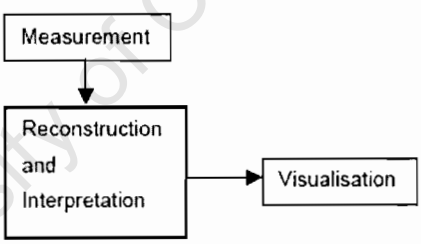

Figure 2.3.3: Parametric-model approach for process tomography.

Here, from the measurements, reconstruction and interpretation are first done, and then an image is displayed for visualization.

The parametric model approach has been used with both EIT and UST systems to visualize the air core on hydrocyclones.

For UST, a circular air core model is directly fitted. The model, with a given radius can then be judged with respect to its suitability by a measure of the goodness of fit between the calculated (from theory) and observed

time-of-flight data from the system. In this manner, an image can be displayed without any reference whatsoever to pixels.

For EIT, if a brine solution is used, the same model can be fitted. This is because the conductivity of the brine is known and the air core is non-conducting. Therefore in order to obtain an image, one needs to obtain the position (two parameters) and the radius (one parameter) of the air core. However there is a problem if the air core is not circular.

Image reconstruction is a simple matter because for a given state defined by a set of parameter values, a goodness-of-fit can be used to compare the measured voltages with the ones calculated by the electric field calculations. Figure 2.3.4 illustrates the procedure for image reconstruction in the Parametric-model approach.

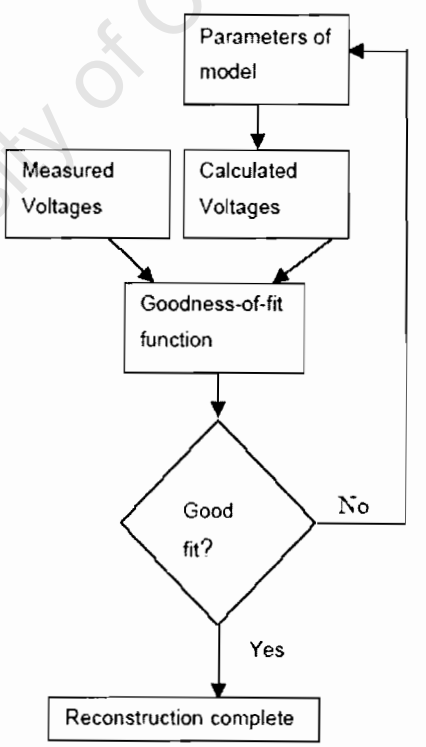

Figure 2.3.4: Diagram illustrating the reconstruction procedure for the Parametric-model approach.

For EIT imaging a slurry solution, the process is different though. This is because the conductivity throughout the solution will vary as a result of the varying slurry concentration. Now a one-dimensional conductivity profile is sought, where the central part will have an area of zero conductivity, corresponding to the air core.

The conductivity profile is modelled on a quadratic function requiring three parameters:

$$\sigma(r) = a + b(3r - 2) + c(10r^2 - 12r + 3) \qquad [21]$$

where σ is the conductivity, a,b,c are the parameters and r is the position between the air core and the boundary such that 0 corresponds to the air core boundary and 1 corresponds to the measurement space boundary. Now, given a certain state of the system defined by the four parameters (air core radius, a, b, c), then by means of numerical simulation of the electric field equations it becomes possible to determine the expected voltages. After this is done, it is then time to calculate the goodness-of-fit measure. There are optimization schemes to find the parameters that give the 'best fit' and these include the quasi-Newton scheme and the Metropolis scheme, each of which have their own advantages.

Figure 2.3.5 shows typical stacked tomograms reconstructed by means of the linear back projection and parametric modelling methods. In each case, 8-planes are displayed.

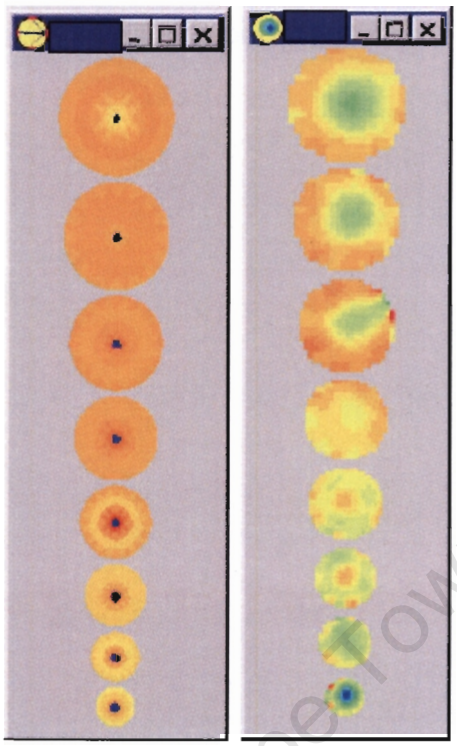

(a) (b)

Figure 2.3.5: Diagram showing stacked tomograms reconstructed by means of (a) parametric modelling and (b) LBP. The same voltage data were used for both reconstruction techniques. [21]

It has been found that the parametric modelling technique gives better detail with respect to the reconstructed images, not only of the air core, but also of distribution of solids within the measurement space.

Other advantages of this technique include faster reconstruction (because fewer parameters are used) and the inverse problem can be better posed (because restricting the number parameters has a regularising effect).

The final method of reconstruction is that of neural networks and will be dealt with in the next section.

2.3.3 Neural Networks in EIT

It has been said that there are two steps towards successful identification in process flows: the first is to develop a non-intrusive instrument and the other is to develop a non-linear mapping approach to perform identification of objects and density profiles within these flows [17].

It has been shown that with suitable training, neural networks are capable of non-linearly mapping arbitrary input to output [17].

From MATLAB's Neural Networks Toolbox, a neural network is defined as: "a network composed of simple elements (neurons) operating in parallel. These elements are inspired by biological nervous systems. As in nature, the network function is determined largely by the connections between elements. We can train a neural network to perform a particular function by adjusting the values of the connections (weights) between elements." [45]

Neural networks can be trained so that particular inputs lead to particular output targets. Below, one can see a diagram illustrating how a network is adjusted (based on the comparison of the output and target) until the output and target are matched.

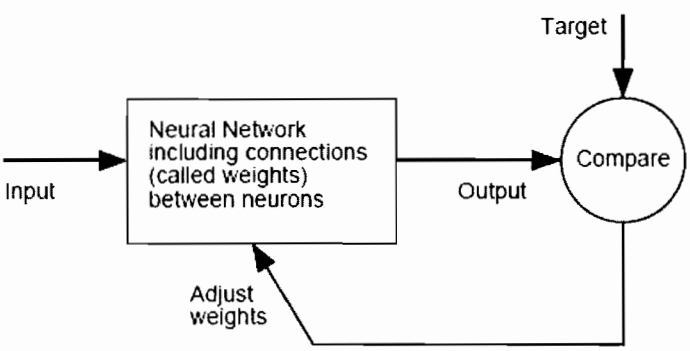

Figure 2.3.6: Diagram illustrating how a network is trained. [45]

Neural networks can be trained to perform complex functions in many different fields for many different applications. Some of these applications include: pattern recognition, identification, classification, speech, vision and control systems [45].

A simple neural network can consist of a couple of input neurons, an activation function and an output. The input neurons are joined to the activation function by weights which can be adjusted in order to achieve a desired output. There are various activation functions, of which the hard-limit, linear, log-sigmoid and tan-sigmoid transfer functions are probably the some of the most commonly used. Figure 2.3.7 illustrates a basic neural network with the addition of a scalar bias.

The input neuron p, is first multiplied by the weight w, the product is then summed with the bias b. The bias can viewed as simply being added to the product wp by the summing junction or as shifting the function f the left by the amount b. ultimately the bias is very much like a weight, but it has a constant input of 1 [45]. After the bias has been added, the sum is then multiplied by the transfer or activation function and an output is given.

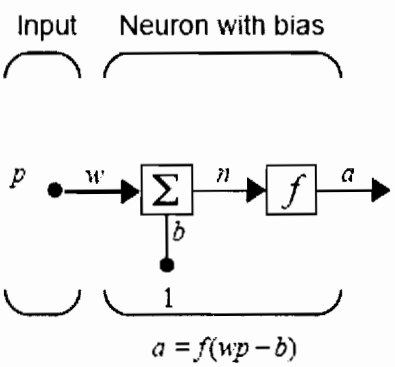

Figure 2.3.7: A simple neuron model with a bias. [45]

A neural network may contain multiple layers of neurons all separated by weights, transfer functions and output vectors. For a more in depth explanation of neural networks, refer to [45].

It is now time to look at how neural networks have been used in the past to identify objects and void fractions within flows.

Research on using neural networks for image reconstruction in process tomography is not nearly as common as it is for medical imaging tasks. It has been suggested that this may be because of the fact that conventional methods have been the industry standards since long before neural networks became accepted engineering tools [28].

In most of the available documented research on using neural networks in process tomography, neural networks were used to solve the inverse problem with respect to the image reconstruction [24, 25, 28]. Here, the networks were trained with simulated measurements. The boundary measurements were simulated using finite element modeling of the systematically created impedance distributions. It was found that the performance of these networks in a real situation was only satisfactory if additional noise (similar to that of the systems measurement noise) was added to the training data [28]. Other neural network papers which did not fall in line with the above included methods such as a Neurofuzzy Methodology, a Boundary Estimation Approach and finally methods where no images are reconstructed but void or volume fraction predictions are given.

In the Neurofuzzy Methodology approach, filtering and the interpolative capabilities of neural networks were combined with the representational advantages of fuzzy systems in order to map idiosyncratic area-averaged impedance measurements to the multiphase flow [17].

In the Boundary Estimation approach, the boundary is approximated by a truncated Fourier series whose coefficients were estimated by means of a multilayer neural network [34]. This approach consists of two stages. First, the network trains weighting matrices using a series of forward problems and their solutions. For this FEM was used to generate the training set numerically by solving the forward problem.

Then, in the second stage, the weighting matrices are incorporated in the inverse solution to estimate the unknown Fourier coefficients from the measured boundary voltage data. The results from this approach showed great advantages in image reconstruction speed and robustness to measurement noise.

In all of the above mentioned techniques, the neural networks are trained with simulated data and not real data. Therefore in most cases the performance and accuracy of the system deteriorates when measurement noise is present. Therefore research into a more practical approach where neural networks are trained using real data [31] was initiated by the De Beers research group. This research was started by Teague and has since been applied to a number of other projects within the group [26, 27, 28]. A brief description of the reconstruction technique follows.

Teague's Reconstruction Method

Teague researched both Multi-Layer Perceptron and Radial Basis Function neural networks for image reconstruction. He found that the Multi-Layer Perceptron network consistently outperformed that of the Radial Basis Function network and therefore stopped using the later in his research.

A Multi-Layer Perceptron network is defined as a densely interconnected, layered network of neurons (as referenced by Teague [20]). Where each neuron consists of a combination function which forms the sum of the

neuron inputs, and an activation function introduces a non-linearity into the network and restricts the output to lie within a certain range [20].

Teague designed two neural networks. The first was to do the image reconstruction, and the second was to give a volume fraction prediction. Teague's EIT system had 56 measurement readings which corresponded to the 56 input neurons for both neural networks.

For the image reconstruction, each pixel in the image was considered to be an output of an individual neural network. Therefore, by combining these outputs in parallel, an image of the overall vessel could be obtained. Teague's image contained 100 pixels, however only 88 of them were situated within the cross-section of the vessel. Figure 2.3.8 illustrates this. Because only 88 pixels fall within the cross-section of the vessel, the network has 88 output neurons.

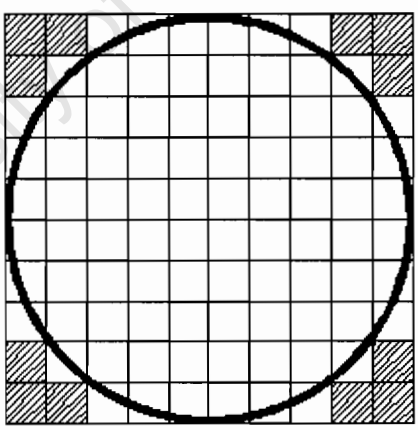

Figure 2.3.8: Image illustrating the pixels which fall within the cross section of the vessel (the cross-hatched pixels are disregarded pixels).

Teague's best results for 3-phase image reconstruction were obtained by using a single-layer feed-forward neural network. The network consisted of 57 input neurons (56 corresponding to the measurement values and an additional input neuron (offset neuron) equal to unity). These input

neurons were then connected to the 88 output neurons (corresponding to the pixels). Teague used hyperbolic tangent activation functions which were employed in the output layer. A Gradient Descent algorithm was used to train this network, and the output pixels either represented air, gravel or seawater.

For the volume fraction prediction, Teague revealed that the neural network could predict the volume fraction of the 3-phases directly. Therefore the volume fraction results can be achieved much faster than if they are worked out from an image. For the volume fraction prediction, Teague had to change his neural network structure to a double-layer feed-forward network. The inputs remained the same, but an additional 'hidden' layer of 25 neurons was added. These were then followed by two output neurons: one to give the volume fraction of air, and the other to give the volume fraction of gravel. The decrease in output neurons and interconnecting weights is actually what causes the decrease in computation time. Now it is time to look at the training of the network.

The training of the network was done by creating a cross section view (like that of figure 2.3.8) of what the vessel might look like in different scenarios. Teague then constructed a number of different size 'bubbles' from both polystyrene (representing air volume fraction) and gravel. These bubbles were then submerged in the saltwater in various positions inside the vessel and at each position boundary measurements were recorded. This was done until all possible bubble positions for both gravel and air were recorded. Because of the static nature of the training, the 'trainer' recorded the bubble positions in the image cross-section and also inputted the volume fraction of each bubble manually. The network was then trained.

Once the network had been trained, Teague needed to test the network and see exactly what his results were like. To do this, different performance measures had to be used. These performance measures are 'Threshold error' and 'Volume fraction error'.

Threshold error refers to the percentage of pixels that are not predicted correctly.

Volume fraction error refers to the percentage error of the volume fraction predictions for each of the three phases.

Goldswain's [28] modifications to Teague's work and neural networks are not included here, as they do not form a basis for the research, but they will be reviewed in the next section.

2.4 History of the Project

The history of all the past research projects by the De Beers research group that are relative to the authors research will be documented in this section. The projects will be presented in chronological order.

The research of Q. Smit – 2000 [19]

The main purpose of Smit's research was to establish whether capacitance data would be useful in gaining information on the interior of a process vessel containing a 3-phase mixture of air, gravel and seawater. He determined that the use of neural networks for image construction would provide promising results.

The research of G. Teague – 2002 [20]

Teague implemented a 16-electrode (16-resistance and 16-capacitance electrodes), bi-modal, FDM EIT system to image the vessel containing the 3-phase mixture. Most of Teague's tests were performed in static situations, however there were also tests performed on simulated bubble movements (this was done by pulling bubbles through the vessel using servo-motors). Teague designed a novel image reconstruction technique using neural networks. Using this technique, he showed that his system could be trained to predict low resolution images of the process vessel. Teague also designed another neural network which would enable the system predict volume fractions of the air and gravel in the measurement space directly. Both these networks were very significant to the requirements of the final airlift application for the project.

The research of A. Giannopoulos – 2003 [26]

In Teague's FDM EIT system, he used square-wave excitation. Giannopoulos re-designed the system to use sign-wave excitation. By doing this, Giannopoulos proved Teague's predictions correct i.e. that the

performance and accuracy of the system would be improved by using 'harmonically clean' sine waves. He used Teague's neural network image reconstruction software to obtain all his results. However Giannopoulos only implemented an 8-electrode bi-modal system.

The research of V. Capindissa – 2005 [27]

The purpose of Capindissa's research was to fit Giannopoulos's hardware to an industrial hydrocyclone and determine whether the software and hardware were adequate to monitor the internal processes of the hydrocyclone. Similar results to those of Giannopoulos were obtained justifying the continuation of this branch of research. The author's current project is a continuation of Capindissa's research.

The research of G. Goldswain – 2005 [28]

Goldswain's research started with modifying Giannopoulos's 8-electrode system to a 16-electrode resistance tomography system capable of measuring 'real' flows. Goldswain upgraded both the data acquisition system and the measurement hardware. He then designed a new electrode set using 16 line electrodes (instead of point electrodes) with a set of guard electrodes on either side of the line electrodes. In terms of the reconstruction software, Goldswain moved away from reconstructing an image, and instead focussed on predicting volume fractions. He designed some new software using a Kernel Ridge Regression (KRR) technique to predict the volume fraction in two phase flows.

Goldswain found that data captured using the line electrodes showed improved results compared to the data captured with point electrodes, when using MLP's to predict volume fractions. He performed two different dynamic experiments, one with a laboratory scale airlift, and the other with a high velocity pumping loop. The results obtained from both

MLP's and KRR for volume fraction predictions were poor for the air lift. Therefore Goldswain simulated boundary measurements with added Gaussian noise and used them as training data. Here, the results were much better.

On the high velocity pump rig, Goldswain's results from both MLP's and KRR were good, with KRR achieving more accurate results.

3 Electrical Impedance Tomography System Structure

The Author's project commenced on 1st March 2005. At this stage Goldswain was still busy with the FDM EIT system, and it could not be used. Because of this, the author started reading up on EIT and other forms of process tomography in order to gain some knowledge on the subject. During this time the author took great interest in two forms of process tomography: Ultrasound Process Tomography (UST) and Electrical Resistance Tomography (ERT). However, because Goldswain was busy with an ERT system which could be used at a later stage, more attention was directed towards understanding UST systems and deciding whether a UST system would be viable for the project (measuring the diameter of a Cyclonic Separator's air core).

After much research and some discussion with the project supervisor, it was decided that it would be better to concentrate purely on EIT systems and wait for Goldswain to finish his research first. Some of the reasons for not going ahead with a UST system were:

- A UST system would have to be designed from scratch.
- Much time and money would be required to design and build the system.
- Once built, the system may not be as accurate as required for the project.
- The UST sensors might not work properly when the cyclone is used with ferrosilicate slurry (echoes might be reflected and scattered, resulting in incorrect measurements).

At the same time that it was decided to leave the UST system out of the project, the author learnt that there was another ERT system being used at the University of Cape Town (UCT). This second ERT system was a TDM based system and was capable of measuring processes at rates of up to 1000 frames per second. Therefore meetings were set up with Dr Wilkinson (project supervisor for second ERT system) in order to find out more about this new ERT system, and if it would be possible to incorporate the system in this project. Wilkinson agreed to let the author use the TDM ERT system and introduced him to the research group that was using this new system.

This meant that there now existed two different ERT systems which the author could use to take measurements of the cyclonic separator's air core.

This section deals with the system structure of both the FDM ERT and TDM ERT systems. It should be noted that because the author had nothing to do with any of the circuitry design or construction, no circuit diagrams will be included in the description. For more information on circuit diagrams, one can refer to [26, 27, 28] for the FDM system and to [32, 33, 35] for the TDM system.

3.1 Frequency Domain Multiplexed ERT System

The FDM EIT system was initially developed by Teague [20], following the work of Smit [19]. Giannopoulos [26] then changed Teague's system from using square-wave excitation signals to sine-wave excitation signals. Goldswain [28] then took over and changed the FDM EIT system into an FDM ERT system. In this section, all information on the FDM ERT system has been taken from the following references [26, 27, 28].

The main components of the FDM ERT system are:

- The primary sensor system.
- The ERT sensor electronics.

The primary sensor system is common to both the FDM and TDM systems and as a result will be dealt with in section 4.2. Therefore only the ERT sensor electronics will be dealt with in this section.

The FDM ERT system is a 16-electrode system which applies voltages on 8 transmitter electrodes and measures the current from all of the transmitter electrodes on each of the 8 remaining receiver electrodes. The voltages are all

applied at the same time but with different frequencies, which means that the system can take a total of 8×8 = 64 measurements. These measurements can then be used in the required reconstruction process.

The main components of the ERT sensor electronics (as can be seen in figure 3.1.1) are:

- The frequency generation boards.
- The transmitter and receiver boards.
- The synchronous detection boards.
- The sample controller board interfacing with the ERT system and data acquisition card.

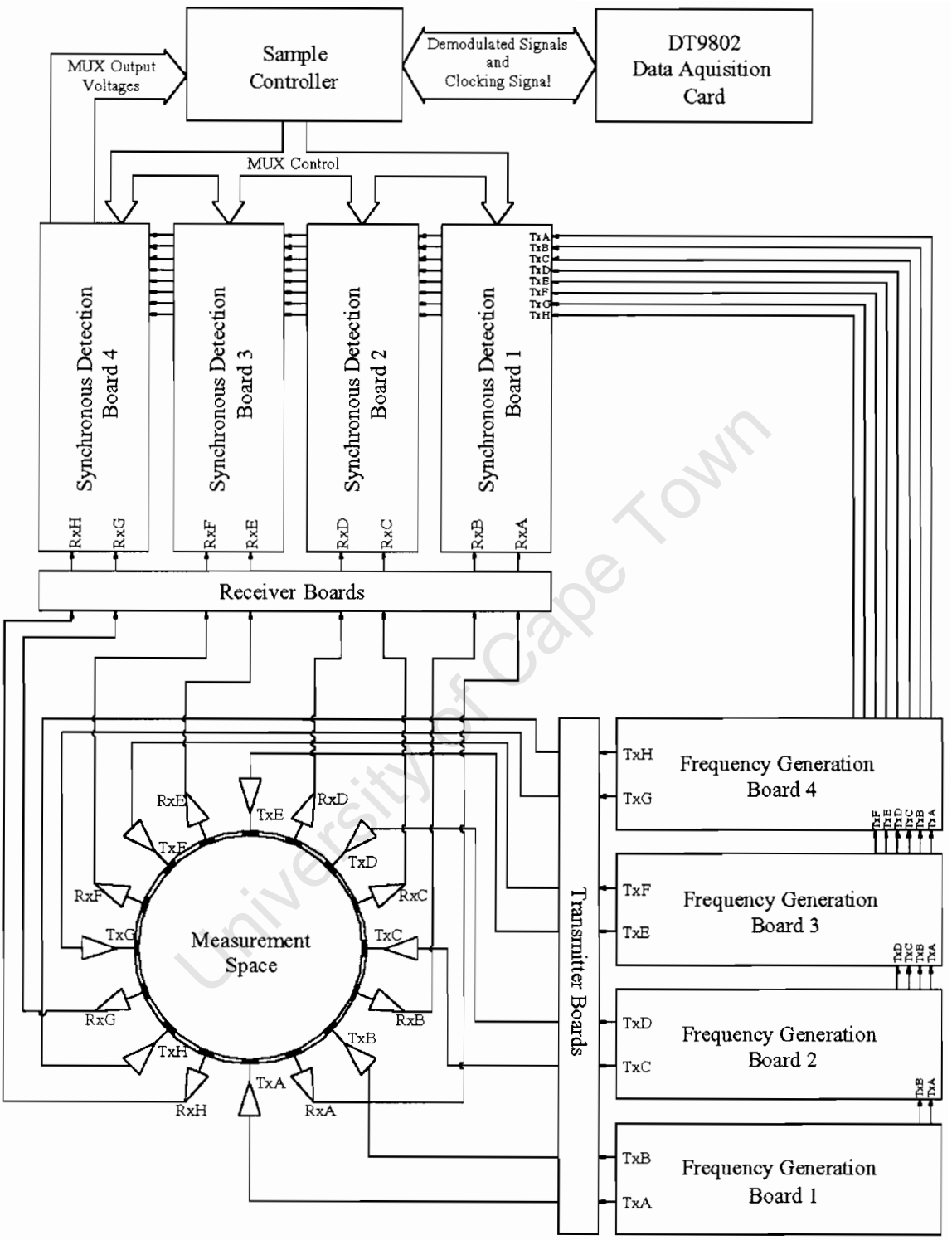

Figure 3.1.1: Block diagram illustrating the FDM ERT system structure.

Frequency Generation Boards

The FDM ERT system uses sine-wave excitation signals that are generated from a PIC microcontroller. Originally, each of Gianopoulos's [26] frequency generation boards (he used two boards) were designed to output four discrete frequencies – two transmitter frequencies and two 90° phase shifted versions of these frequencies. The phase shifted versions were only used as reference signals in the demodulation of the capacitance data. Goldswain extended the system to a 16-electrode (8-transmitter and 8 receiver electrodes) ERT system. Therefore he needed four more frequencies to drive the transmitters. In order to obtain these frequencies, Goldswain had two new frequency generation boards (exact copies of Giannopoulos's boards) made and populated. With four boards, it now became possible to generate eight discrete frequencies and their respective quadrature signals. The frequencies generated are shown in table 3.1.1.

Table 3.1.1: The eight discrete frequencies generated by the FDM ERT system.

Sine Waves Frequencies for the 16-Electrode FDM ERT System		
Board Number	**Transmitter**	**Frequency (kHz)**
1	TxA	24.375
	TxB	37.5
2	TxC	39.375
	TxD	46.875
3	TxE	50
	TxF	56.875
4	TxG	62.5
	TxH	78.125

The Transmitter Boards

From the frequency generation boards, the signals are sent to transmitter boards which amplify and inject the signals into the measurement space. Goldswain intended using the FDM system on small diameter pipes containing fresh water. Therefore he had to re-designed the transmitter boards, as the ones used by

Giannopoulos were originally designed for use on large diameter (>200mm) pipes containing seawater. The currents expected in the small diameter pipes should be are much lower and therefore regular op-amps are be used to drive the transmitter electrodes. Goldswain chose to use AD797 op-amps which offer ultra low distortion, wide bandwidth and a high current output.

The Receiver Boards

Once the signals have been injected into the measurement space, they have to be collected on the receiver electrodes by the receiver boards. The receiver boards used by Goldswain remained almost the same as the ones used by Giannopoulos, with the exception that because the magnitude of the received current is much smaller, no buffer is required in the feedback path of the transimpedance amplifier. Goldswain also used an improved LF411 amplifier on the new receiver boards.

Synchronous Detection Boards

The synchronous detection system of the ERT system consists of four synchronous detection boards. Originally, each board would perform synchronous detection for one complete channel (where a channel consists of resistance and capacitance signals from one frequency). However, with the change of the FDM system from an EIT to an ERT system, changes had to be made to the boards to incorporate the extra frequencies. Goldswain decided for various reasons that it would be too much effort to re-design, test, print and populate entirely new boards. Therefore he decided to populate the empty half of the existing boards. Now each synchronous detection board is a demodulation board for two receivers in the FDM ERT system.

The Sample Controller Board

In order to make the data capturing process faster and more efficient, a sample controller is used. A sample controller allows streaming, and thus a large amount

of data can be transferred from the synchronous detection boards to the data acquisition system. Meaning higher sampling rates are now possible.

One of the major problems that Teague and Giannopoulos experienced was that there was a loss of synchronisation between the sample controller and the data acquisition card (DAC). The reason for this was that there was an external line which in the presence of noise, would cause false triggering of the DAC. Goldswain solved this problem by using a common source for the sampling trigger scan and counter clock as apposed to an external clock source. This source was from the 'new' DAC (DT9802) output trigger. The result of the new trigger line is that if noise occurs, both the counter and trigger scan are affected; hence there is no loss of synchronisation, only a bad data point.

Data Acquisition Card

For data acquisition, Goldswain used a DATA TRANSLATION DT9802 card. The DT9802 is a USB data acquisition module with high functionality. Initially it seemed like an attractive option, however with a little experimentation, it was revealed that for high sampling rates and for the sampling to be perfectly synchronised with the external hardware, the module had to be hard coded in **C**. The coding for the module was outsourced and the following requirements were met:

- 256 analogue voltages can now be sampled per frame.
- Data can be captured at a rates of 200 frames per second.
- The card controls the address lines for the 8 16-channel multiplexers.
- The card can average the data from a number of frames.
- The code can accept a mask file which tells it which samples to use in reconstruction.

In the case of the first point, one can see that the card can sample 256 voltages. It should be noted that for one plane of resistive data there are 64 corresponding

voltages. The reason that the card must be able to sample 256 voltages is so that the FDM system can be extended to a 2-plane, 16-electrode FDM EIT (capacitance and resistance measurements) system.

3.2 Time Domain Multiplexed ERT System

The TDM ERT system that the author used was developed by Wilkinson et al. [32, 33, 35]. It is also a 16-electrode system, however, it utilises a technique where a switched DC current pulse is injected into the measuring space by an adjacent pair of drive electrodes and the resultant voltage waveforms are then measured across the remaining 'sense' electrode pairs. The system uses an adapted adjacent pair measurement strategy where current is injected into the measurement space through 16 'drive pair' electrodes and the resultant voltage is measured between 13 'sense pair' electrodes. Using this strategy, the system is able to obtain a total of 208 voltage measurements which can be used in the reconstruction process. It should be stated that the hardware does allow current injection on any required pair of electrodes; however the sense electrodes are hardwired to adjacent measurement pairs. The TDM system is capable of running at speeds of up to 1000 frames per second for a single plane, and because the system design incorporates a multiplexor allowing a total of 8 planes of electrodes (16 electrodes on each plane) to be sampled sequentially, the system can capture data from all 8 planes at a rate of 125 frames per second. One of the major advantages of having a system that can image 8 planes is that one can do both 2D (of each individual plane) and 3D image reconstructions.

The TDM ERT system can be seen to consist of the following main electronic components (figure 3.2.1):

- A micro-controller
- Current Source
- Current drive multiplexor
- Amplifier/sample and hold (16 channel)
- Layer select multiplexor
- Data Acquisition Card (ADC/DAC)

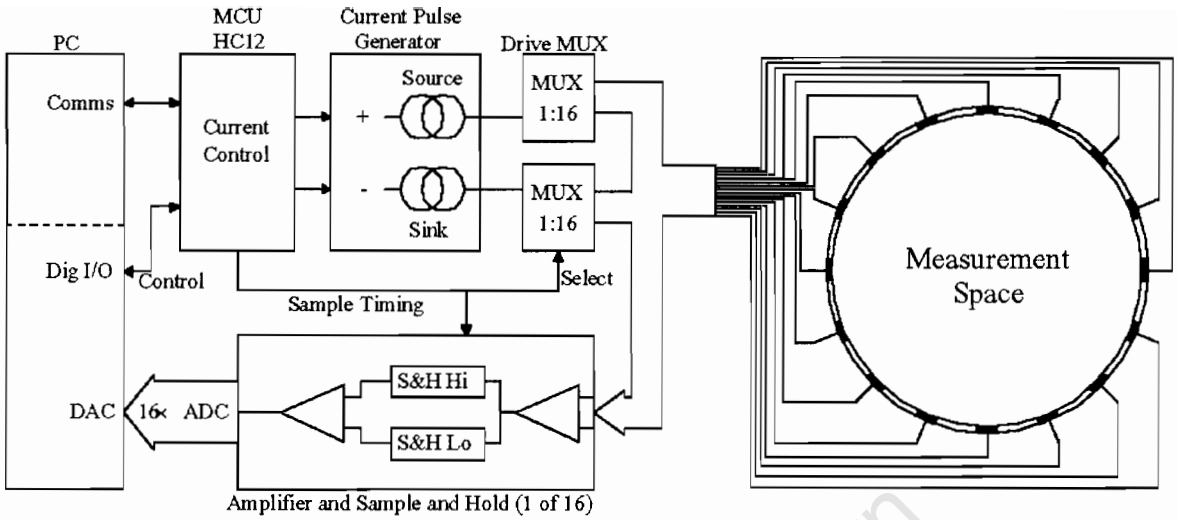

Figure 3.2.1: The TDM ERT system for a single plane of electrodes.

The Micro-controller

The purpose of the micro-controller is to control all the surrounding hardware and carry out all critical timing operations. These timing operations include the current pulse duration, gate time of sample and holds, and the triggering of the ADC/DAC. One of the major advantages of using a micro-controller is that the timing issues that one usually faces with PC operating systems can be avoided.

The Current Source

For successful operation, the TDM system relies on the generation of both noise-free and transient-free current pulses for injection into the drive electrode pairs. For this a separate current source and sink are used (as can be seen in figure 3.2.1) which enable a set current to be delivered continuously unless the current is not required. If the latter is the case, then the current is forced to bypass the load by means of transistor switches.

If the system is required to run at 1000 frames per second, current pulses with a period of 12μs are required. With these current pulses, it is critical that the current settles to a constant value during the gate period of the sample and hold.

The Current Drive Multiplexor

In order to make image reconstruction possible, one needs to first acquire data from the measurement system. Therefore one needs to connect the electrode array to the measuring hardware in a specific sequence. For this purpose multiplexing strategies, which are generally a compromise between hardware complexity and flexibility in the measuring sequence, are used.

For the current drive, there are two 16-way multiplexors which are used to select the adjacent electrode pair used for current injection. One multiplexor source/sinks the current while the other grounds the second electrode of the selected electrode pair.

Amplifier/Sample and Hold (16 Channel)

Instead of multiplexing all the electrodes to a single channel, the TDM system uses multiple amplifiers and thus largely reduces the time for measurements to be taken. The differential inputs of the amplifiers are all hardwired to adjacent electrode pairs in order to implement the desired measurement scheme (in this case, the adjacent pair method). Now, the peak to peak amplitude is determined by means of sampling and subtraction in the hardware and as a result of this technique, the DC offset (voltage) is removed. This in turn means that subsequent amplification can be done so as to utilise the ADC/DAC's full dynamic range. It should also be stated that only one ADC reading is required to yield the amplitude and as a result data acquisition time is greatly reduced.

For a more in depth explanation, refer to [32].

The Layer Select Multiplexor

The layer select multiplexer enables the system to switch between each of the 8 electrode planes in between each frame capture sequence. To do this, it is required that each of the 16 electrode input/output connections of a single plane must be switched to the electrode system of a specific layer as required. Therefore each of

these 16 I/O connections requires a 1:8 way device. In principle, this seems like a relatively simple task. However, in practice it can only be realised by means of some complex wiring.

The layer multiplexor basically makes it possible for images to be reconstructed from each layer independently, or from measurements made between electrodes from different layers which in turn make it possible to do 3D reconstructions. Some of the current injection patterns employed by the TDM system are: injection on one layer and measurement on the same layer; injection on one layer and measurement on any layer; injection between two layers and measurement on any layer; and finally, injection between two layers and measure any adjacent pair between two layers. For a full description of these techniques, one can refer to section 2.2.6.

Data Acquisition Card

There are three different data acquisition cards that Wilkinson's research group have been using with the TDM system. Two are PCI cards, and the other is a USB2 data acquisition module. The first PCI card that was used was an Eagle PCI-703. The second PCI card is a National Instruments PCI-6070E and the USB2 module is an Eagle microDAQ Data Acquisition Module. It should be stated that the two PCI cards can achieve slightly faster data rates than the data acquisition module.

The software that both the FDM and TDM ERT systems use will be discussed in section 5.

4 Apparatus Design and Construction

When the author's project commenced, various goals were set including using Capindissa's existing hydrocyclone and sensor systems, and performing various tests with them to determine if they were adequate for the author's use. This section deals with Capindissa's hydrocyclone and sensor designs, and the new improved sensors designed and constructed by the author.

4.1 The Hydrocyclone

The hydrocyclone that was available for use was a 50mm diameter Krebs hydrocyclone. It has already been stated in section 2.1.1 that a hydrocyclone consists of three main parts: a tangential inlet, a cylindrical section and a conical section. For the case of the Krebs hydrocyclone, it consists of 2 main parts: the tangential inlet and then the remaining cylindrical and conical sections which are merged together to form the remaining part of the hydrocyclone. Figure 4.1.1 shows a picture of the two main parts of the Krebs hydrocyclone.

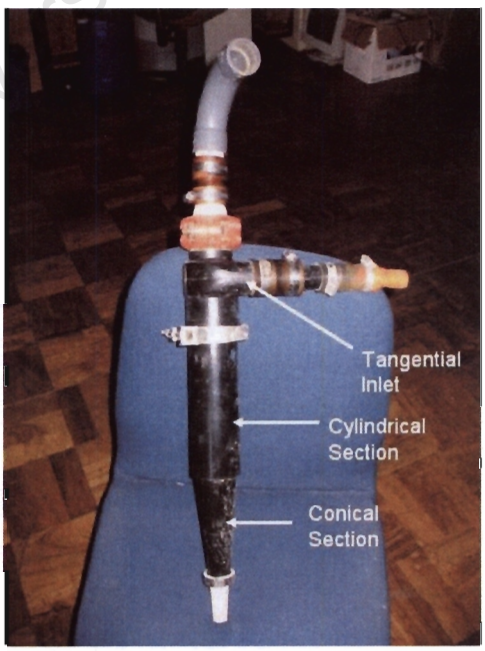

Figure 4.1.1: Picture of the Krebs hydrocyclone showing the different sections.

Due to the nature of an EIT system, conductive electrodes have to be mounted through the walls of the process vessel so that they can be in contact with the fluid. Therefore, Capindissa decided that it would be best to build new cylindrical and conical sections (that could be attached to the existing tangential inlet) for the hydrocyclone. To do this, Capindissa made all the necessary measurements of the existing sections (with respect to the lengths of both the cylindrical and conical sections and the spigot diameter) of the hydrocyclone. It was decided that the new sections be constructed from clear Perspex acrylic plastic. The reason for this being that it would enable one to make visual observations of the process and make a rough comparison between these observations and the measurements taken by the tomography system. Figure 4.1.2 shows the Perspex sections. For the drawings showing the design dimensions, one can refer to appendix A.

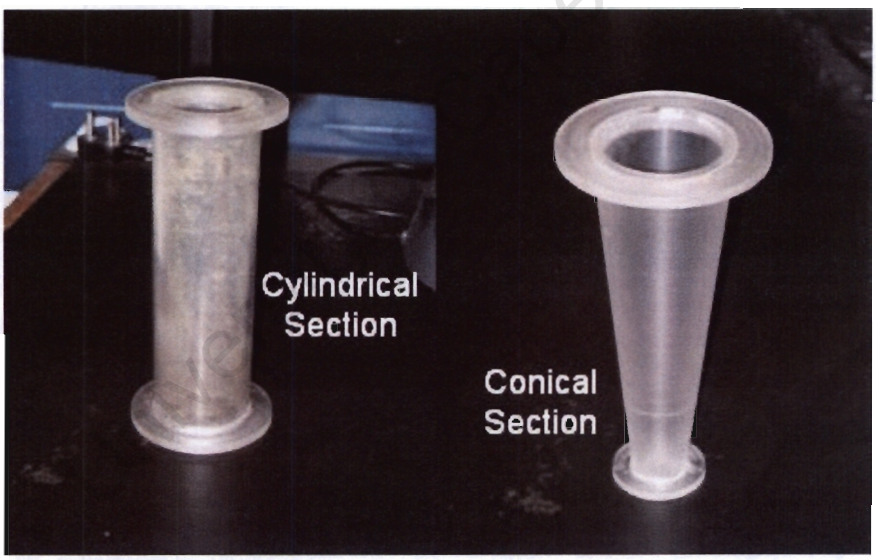

Figure 4.1.2: Picture of the Perspex sections designed for the hydrocyclone.

Both the new sections were fitted with Perspex disks so that they could be connected to the tangential inlet by means of Krebs clamps. The cylindrical section was clamped underneath the tangential inlet, and then the conical section was clamped underneath the cylindrical section. The hydrocyclone's spigot could then be clamped to the underside of the conical section. A picture of the assembled sections can be seen below.

Figure 4.1.3: Picture of the Perspex sections connected together.

The next step in construction was to fit the sections with electrodes.

4.2 The Sensor System

When Capindissa designed the new hydrocyclone sections, he commissioned UCT's Mechanical Engineering workshop to construct five cylindrical sections and one conical section. This was done so that it would enable the project group to construct a number of different sensor units for the hydrocyclone. Capindissa found that the cylindrical section was ideal for fitting the rectangular capacitor plates. Therefore he used one of the cylindrical sections to construct an 8-electrode (8 capacitor electrodes and 8 conductive electrodes) EIT sensor system. The capacitor plates were mounted on the exterior of the cylindrical section while

the conductive electrodes were drilled through the walls. Capindissa decided to uses three layers of conductive sensors for the reason that the three sets would give a volumetric sensing region [27]. Capindissa then constructed a second sensor rig, this time for a 16 electrode ERT system. These were the rigs with which the author was first meant to perform tests, but since Goldswain had proved that using line electrodes gave better results than point electrodes, Capindissa's electrode rigs were discarded.

The reason that the line electrodes perform better in an ERT system is that they reduce the effects of fringing and provide a more volumetric sensing region than point electrodes. The concept of fringing is illustrated in figure 4.2.1.

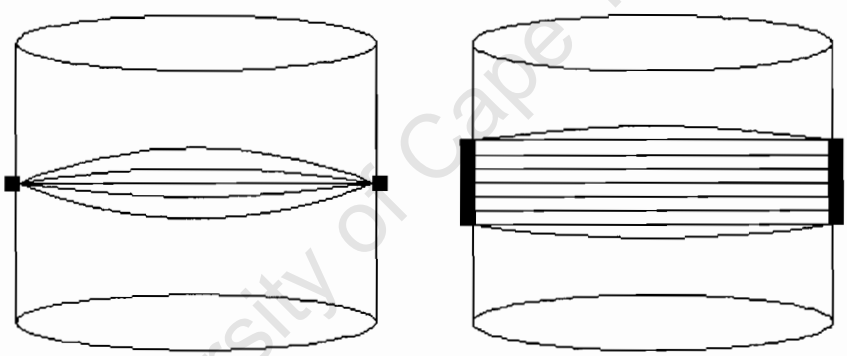

(a) (b)

Figure 4.2.1: A diagram illustrating the fringing effects on both (a) point and (b) line electrodes. As on can see, the fringing effect on the line electrodes is reduced relative to the main electric field.

When a line electrode rig is designed, two important parameters that have to be considered are the length and width of the electrodes. The reasons for this are that the length should take into account such considerations as the required frame rate, and the maximum expected flow velocity in the process vessel. The width of the electrodes is important because for the FDM ERT system there is a compromise between thin electrodes required for the receivers, and broad receivers required for transmitters. [28]

Goldswain's new sensor rig design was implemented on a 57mm diameter PVC pipe section. His rig design incorporated 16 line electrodes with a set of 16 guard electrodes on either side of the line electrodes. These guard electrodes were designed to further reduce the fringing effects of the field. This rig achieved better results than the ones Capindissa had designed, and as a result were taken as a basis for the future design of sensor systems. The only problem with Goldswain's sensor rig was that the pipe diameter was too large to be fitted to the hydrocyclone, having been designed for use in a mini-airlift. This resulted in the need to design a new line electrode rig specifically for the hydrocyclone. Therefore the author took to the task and designed both a single-plane and multi-plane rig.

4.2.1 Conductive Sensors

The aim of conductive sensors is to place electrodes on the periphery of the process vessel in such a way that they are in contact with the fluid being imaged, but do not restrict or influence the fluid flow in any manner. The electrodes are all placed equidistantly around the boundary of the process vessel. There are two important parameters to consider in the design process. These are the dimensions of the electrodes (Goldswain showed that line electrodes perform best [28]) and the material from which the electrodes will be made. The first parameter has already been discussed, so there is only the second parameter to consider. For the second parameter, the issue of contact impedance and corrosion need to be avoided. For contact impedance, the material used needs to be more conductive than the fluid being imaged (the size of the electrodes also influences contact impedance), and for corrosion purposes, one needs to consider the whether the fluid will cause the electrodes to corrode or not.

4.2.2 Single-Plane Sensor Rig

With all of the above information taken into account, the author could now go about designing the new electrode sets. The first electrode set to be designed and built was the single-plane sensor rig.

Because there were three Perspex sections for the hydrocyclone that Capindissa had not used in his constructions, the author decided to use one for the new rig. The first step in the design process was to decide on the dimensions of the electrodes. The final dimensions were based on educated guesswork as well as dimensions from the sensor rigs built by Goldswain and Wilkinson's research group.

It was decided that the electrodes would be 15mm in length and 5mm in width. For the drawing showing the dimensions of the electrodes, one can refer to appendix A. Once a decision had been made with respect to the dimensions, it was time to decide what material the electrodes should be constructed from. There were two materials that could be used: brass or stainless steel. Both materials are good conductors. Brass has the advantage that it is easier to cut and work with, stainless steel has the advantages that it is less corrosive and harder, and will therefore be better in an abrasive environment. Although in the long run stainless steel would be a better choice, brass was chosen. This was because the rig was a test rig and was going to be used in a fresh water environment. Therefore the brass would make it easier to shape and fit the electrodes.

In order to fit the electrodes into the Perspex section, milling needed to be done. UCT's Mechanical Engineering workshop milled the 16 holes required. It should be stated that great care should be taken when milling Perspex as it is brittle and has the ability to crack very easily. Once the holes had been successfully milled and the electrodes shaped (by hand),

they were then glued in place (flush with the interior wall of the vessel) with Pratley's Quickset Epoxy.

A picture of the completed rig can be seen below.

Figure 4.2.2: Picture of the single-plane electrode rig.

Finally holes were drilled into the electrodes so that the shielded cables (for noise reduction) could be connected (by means of screws) to the electrodes.

4.2.3 Multi-Plane Sensor Rig

For the multi-plane sensor rig, another one of the Perspex sections was used. It was decided, based on the length of the Perspex section and the length of the electrodes, that the section should house six planes of electrodes. UCT's Mech. Eng workshop once again milled all the holes in the section. A total of 96 holes were milled. Because of the number of

electrodes required, and because shaping them from brass would take an extremely long time, the electrodes were laser cut from a 10mm thick brass sheet so that they would fit snugly into the milled holes. The electrodes were once again glued in place with Pratley's Quickset Epoxy. Once all the electrodes were in place it was decided that solder tags be soldered to the electrodes. The shielded cables could then be attached to the solder tags by means of small spade connectors. For the drawing showing the dimensions of the multi-plane section, one can refer to Appendix A.

A picture of the completed vessel can be seen below.

Figure 4.2.3: Picture of the six-plane electrode rig.

4.2.4: Cables and Socket Attachments

The cabling used to connect the sensor rigs to the hardware systems was standard 2.5mm (diameter) shielded cable. The hardware systems used two types of connectors: male DB25 connectors and 36 pin male Centronics connectors. The schematic diagrams showing the wiring configurations for each type of connector can be viewed in appendix A.

4.3 The Blender Unit

After a progress meeting with De Beers took place, it was decided that both the ERT systems imaging capabilities should tested with ferrosilicate slurry in addition to testing them with water. The reason for this was that De Beers uses ferrosilicate slurry in their cyclonic separators.

The slurry consists of finally ground ferrosilicate and has a dense, opaque nature. Therefore, the slurry makes it impossible to see the air core formed in a cyclonic separator, even if all the sections are made from Perspex. This means that no comparison can be made between the visual observations (as none would exist) and the tomography measurements.

In order to solve this problem, the author decided to design a special unit with a fast spinning impeller at the base of the sensor rig. When spinning quickly enough, the impeller would create an air vortex in the centre of the fluid, much like that of an air core within a cyclonic separator. After some consideration, it was decided that a blender would do the job. Most blenders nowadays have a variable speed setting which enables the user to choose the speed according to the type of food being processed. This variable speed has the advantage that it can also be used (for the case of this project) to control the size of the air vortex.

A 500W blender was purchased by the author and the impeller system was dismantled and re-designed so that the sensor electrode sections could easily be fitted to the impeller base. The design for the new impeller base can be seen in appendix A. The new base was constructed from polypropylene plastic. Figure 4.3.1 shows pictures of the new impeller base for the blender. Once construction of the new impeller base was finished and the blender had been tested, it was decided that power to the blender should first be routed through a Variac so as to enable even greater control of the impeller speed.

Figure 4.3.1: Pictures of the new blender base. The electrode rigs are fitted to the top of the base and then the base is fitted to the blender.

5 System Software and Neural Network

This section covers all the software used and designed by the author for the two ERT systems. It should be noted that the author did not design any of the software used in operating or for online use of the two ERT systems, he only designed the neural network reconstruction software.

5.1 FDM ERT Software

The FDM ERT system that that was used by both Goldswain and the author currently has no online reconstruction software. When the system was initially developed by Teague, it functioned as a FDM EIT system (ERT and ECT). For the EIT system, Teague developed online neural network reconstruction software which was coded in Delphi. Teague's software was then used by both Giannopoulos and Capindissa. When Goldswain took over the research, he changed the FDM EIT system to a FDM ERT system and hence the code developed by Teague became incompatible. Therefore new online code needed to be developed. No code was however developed by Goldswain for online reconstruction and therefore the only software that exists and is compatible with the FDM ERT system is the software used to capture measurement data from the ERT system to a PC for offline reconstruction.

The software used for data capturing is called 'continuous.exe'. When this software is started up, it communicates with the FDM system via the USB data acquisition module. A screen capture of the software interface can be seen in figure 5.1.1. To capture data to the PC, the software has to be set up as follows:

1. The user must choose a file name. To do this the user must browse under the 'Data Filename' field and then input the name of the file and the location of where the file must be saved. The file will be saved as a

Comma Separated Value (.csv) file which can be opened in Microsoft Office Excel.

2. The user must then browse for the correct 'Mask filename' (the purpose of the mask file is explained in section 3.1). The filename for the mask file is 'gareth.msk'.
3. Next the user must choose the number of frames to average.
4. Finally, the user must choose the overall number of frames that the system must capture. It should be noted that if the user chooses average every 3 frames and to capture 3000 frames, the system will actually measure 9000 frames. But because of the averaging, only 3000 frames of data will be saved to the .csv file.

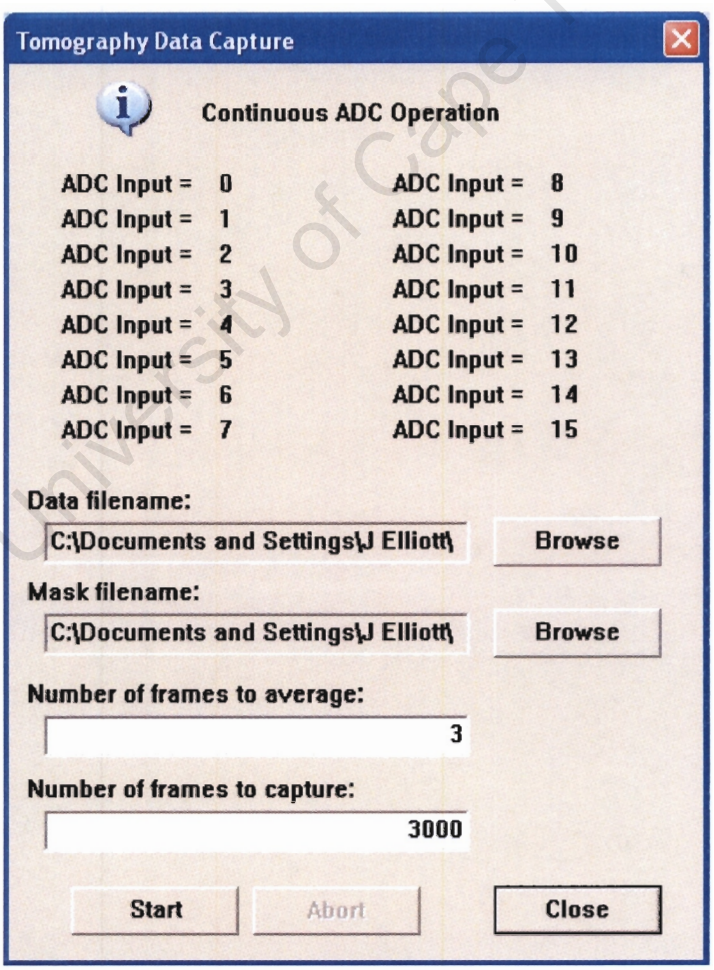

Figure 5.1.1: Screen Capture of the 'continuous.exe' software used to capture FDM ERT data to the host computer for off-line reconstruction.

Once the .csv file has been saved to the host computer, continuous.exe can be used again (run through steps 1-4 again) to capture more data or the application can be closed.

For the reconstruction software, Goldswain used MATLAB to code both his neural network (based on Teague's neural network design) and Kernel ridge regression software to predict the volume fractions. The author's reconstruction software will be dealt with in section 5.3.

5.2 TDM ERT Software

When the TDM ERT system software was designed by Wilkinson's research group, there were three requirements: real-time visualization, data storage for subsequent analysis, and reconstruction at a high frame rate for real-time applications. It found that a real-time flicker-free image of the process vessel could be obtained by displaying 15 frames per second. The images are obtained by using a real-time reconstruction algorithm based on a single iteration of the Newton Raphson algorithm with regularization implemented on a 2D finite element mesh grid. [32, 33]

When data is acquired from the TDM system hardware by the DAC, it is first transferred by the card's driver software to a RAM buffer. Wilkinson's group wrote two independent programs in C++ to deal with the data.

The first piece of software transfers the data to a (single) frame buffer. This frame can either be data from a single frame or the average of multiple frames.

The second piece of software then reads the frame from the buffer and does the image reconstruction and drives the real-time display. Figure 5.2.1 shows the data flow and program (thread) functions for the TDM system using an Eagle PCI703 data acquisition card.

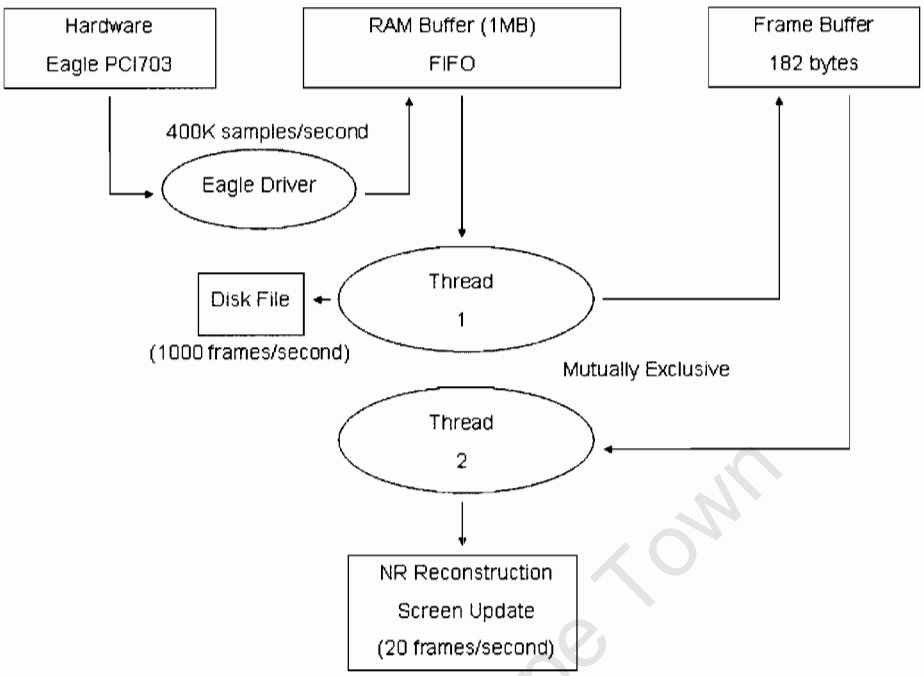

Figure 5.2.1: Diagram showing the data flow and program functions for the TDM system. In this diagram it can be seen that the system is using an Eagle PCI703 data acquisition card. [33]

The FEM model used in the forward problem of the image reconstruction for the TDM system assumes that the process vessel is circular, and has 16 electrodes around its circumference. Regardless of how accurate the FEM model is, there will always be some form of error resulting from one or a combination of the following: mismatch of amplifier gain, contamination and corrosion of electrodes, imperfect process vessel and electrode geometry, and lastly the process vessel may contain mixing devices etc. These errors introduce artefacts in the reconstructed images and as a result make it difficult to detect smaller disturbances in the conductivity. [32, 33]

Therefore to overcome these errors, some form of calibration is needed. The calibration implemented by the TDM system scales the measured data points to

precisely match the ones predicted by the forward model for a uniform conductivity cross section. The scaling factors are then applied to the disturbed system and enable the changes in conductivity to be resolved. The calibration technique used largely eliminates the effects caused by mismatched gain and process vessel irregularities. It also significantly compensates for the effects caused by impellors within the vessel. [32, 33]

For a more detailed explanation on the calibration technique used, one can refer to [33].

A screenshot from the TDM system's software for a single plane image can be seen in figure 5.2.2. It should be noted that the software is much more complex than that used for the FDM system, and as a result only a basic explanation of how to use the software follows. For a more detailed explanation of the software and how to use it, one can refer to [48].

When the author used the TDM system software, it was set up as follows:

1. The first step is to choose how many planes the user wants to image.
2. Next the system is calibrated.
3. The user then opens the data capture wizard. Here the user enters the destination folder where all the data must be saved to, as well as how many frames should be averaged for the image reconstruction.
4. Next the amount of time for the system to capture data is input.
5. The system can now be started and will automatically stop once the data is captured. While the system is capturing the data, images are being displayed (real-time) at a rate of 20 frames per second on the display monitor.

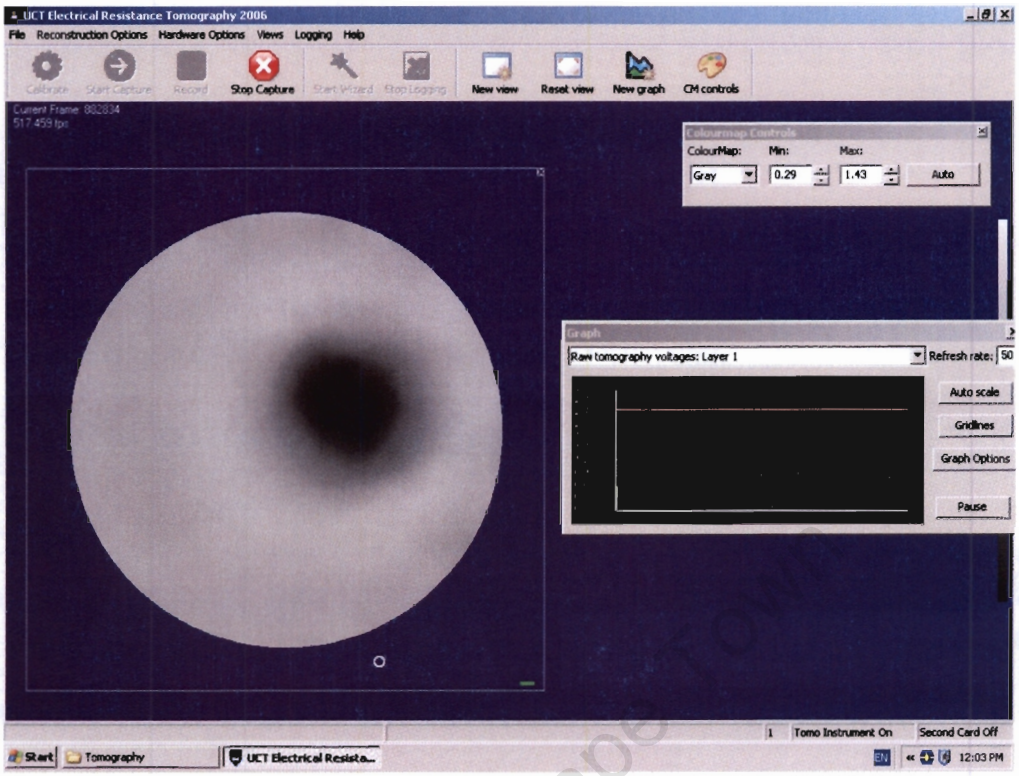

Figure 5.2.2: Screen Capture of the software used to capture and reconstruct the TDM ERT data on-line. The grey image with a black dot is a cross-section image of the single-plane vessel and the graph to the right of the image is a plot of the measured voltages between the electrode pairs.

Because the FDM system data is all reconstructed off-line, it was necessary to use the TDM system's data off-line in order to make a comparison between the accuracy of the two tomography systems. With the TDM system software, it is possible to reconstruct the captured data and store it in a two different files. The first file (.con or .bin) contains all the data that is needed to reconstruct the conductivity distribution images frame-by-frame, and the remaining file (.tom) contains all the voltages measured at the respective electrodes.

For the offline reconstruction of the TDM data, the author was able to obtain some MATLAB skeleton code for the reconstruction of the images and for loading the .tom files into matrices displaying the respective voltages. This code will be discussed further in section 5.3.

5.3 Off-line Reconstruction and Neural Network

Both the TDM and FDM tomography systems use very similar offline reconstruction software. The only difference is that the TDM system needs extra code to do the image reconstruction from the saved files. This section will start with a brief description of the offline image reconstruction software used for the TDM system. All code for the offline processing of data and image reconstruction was done in the MATLAB coding platform.

5.3.1 Image Reconstruction Code

The skeleton code used for reconstructing and displaying the saved image files was mostly obtained from Wilkinson's research group. There are currently two different pieces of code being used for this purpose.

The first piece of code (convertbinconductivityfile.m) loads either a '.bin' or a '.con' file into the MATLAB platform and displays an image of the conductivity distribution from within the measuring space taken in a static situation. The code can be seen in appendix B and works as follows:

1. First the code calls the function 'open_mesh_file.m' which opens a mesh file (.mes) saved by the TDM system and returns the required mesh structure.
2. Then the code opens a standard 'open file' dialog box which prompts the user to choose the file (.con or .bin) which is to be reconstructed and the resultant image displayed.
3. The file, and all data contained in the file, is then loaded into various matrices and finally into the mesh-grid.
4. The code then re-grids the data and a final matrix (map_) containing all the conductivity values is formed.

5. Lastly, the 'imagsc' function is called which scales the data contained in map_ and displays it as a conductivity distribution image.

The second piece of code (convertbinconductivityfile2.m) loads either a '.bin' or a '.con' file into the MATLAB platform and initially displays 3 images. The first image is a standard deviation in the image with no averaging. The second image is a graph displaying the time sequence of the reconstructed conductivity in one pixel element. Finally the third image is a graph displaying the Fast Fourier Transform (FFT) of the second image. All in all these three images are not of interest to the author and his project and thus can be eliminated. Ultimately this piece of code is used to load all the frames saved from a dynamic measurement set (from the TDM system) into the MATLAB platform. The code can be seen in appendix B and works as follows:

1. First the code calls the function 'open_mesh_file.m' which opens a mesh file (.mes) saved by the TDM system and returns the required mesh structure.
2. Then the code opens a standard 'open file' dialog box which prompts the user to choose the file (.con or .bin) which is to be reconstructed and the resultant image displayed.
3. The file, and all data contained in the file, is then loaded into various matrices containing the number of frames etc.
4. Lastly the code plots the three images mentioned earlier, which are not further processed.

Now that all the frames of data have been loaded, the author decided that a nice way of displaying the conductivity distribution images frame by frame would be to load them into an '.avi' movie file which could be played back on any PC and hence show the dynamic measurements. To do

this, a function was written by the author and T. Long (a member of Wilkinson's research group). The code can be seen in appendix B and works as follows:

1. First the user must enter the file name under which the movie must be saved.
2. Then the frame-rate and the colour-map range for the movie are set.
3. The code then retrieves the number of frames of conductivity data (number of images which will ultimately be loaded into the movie) and calls the 'avifile' function, which then creates the AVI movie file.
4. Finally a loop runs which re-grids and loads all the images of the individual frames into the AVI file and the movie is saved.

The movie file can then be played back in any Windows based media player.

5.3.2 Neural Network Design and Related Code

It has been mentioned previously that Teague used a neural network to predict the volume fractions of both air and gravel when using the FDM EIT system. When Goldswain changed the FDM EIT system to a FDM ERT system, the ability of the system to predict a 3-phase mixture was lost and the system was only able to predict the volume fraction of a two-phase mixture (air and the continuous fluid) within the process vessel. Therefore Goldswain had to change the structure of Teague's neural network as well. Where Teague originally had 56 input neurons (28 capacitance and 28 conductance), Goldswain increased the number to 64 (the number of conductance measurements). Goldswain then changed the number of output neurons from two (gravel and air volume fractions respectively) to

one (air volume fraction). For the hidden layer, Goldswain left it the same as Teague's design with a layer of 25 hidden neurons as this network structure achieved the most accurate results. Therefore, based on the results from the changes made by Goldswain, it seemed pointless to redesign the entire neural network structure, and hence the network structure for the TDM ERT system remained almost the same as the one used by Goldswain. The only difference was that the output changed from a volume fraction prediction to a diameter prediction.

For the TDM ERT system however, the network structure had to change as there were no longer only 64 input measurements, but 208. Therefore the number of input neurons was increased from 64 to 208. The number of output neurons remained the same as both system ultimately have the same goal (trying to predict the air core diameter of an air core). Because of the increase in the number of input neurons, it only seemed logical that the number of neurons in the hidden layer should also be increased. Therefore after some calculations and some testing, the author found that the best output results were obtained with a hidden layer of 33 neurons. Figure 5.3.1 below shows the structure of the two neural networks.

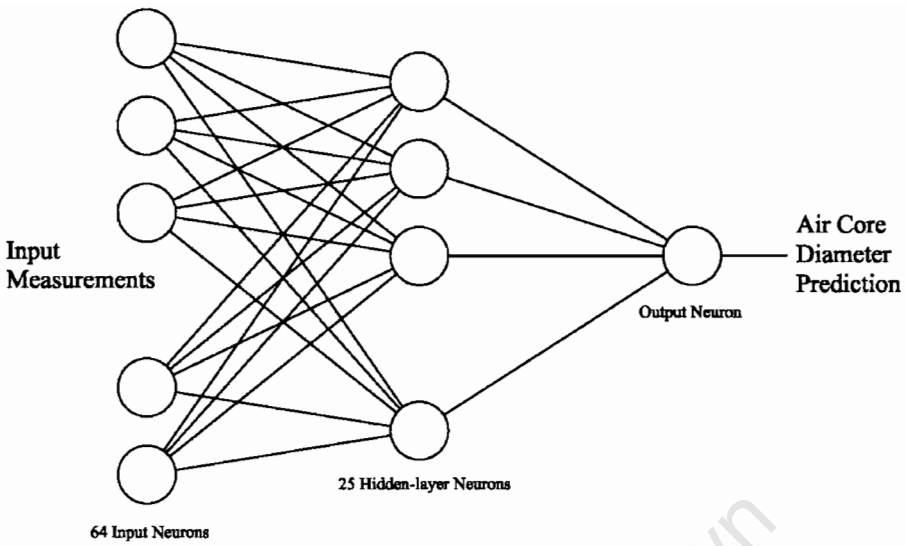

(a)

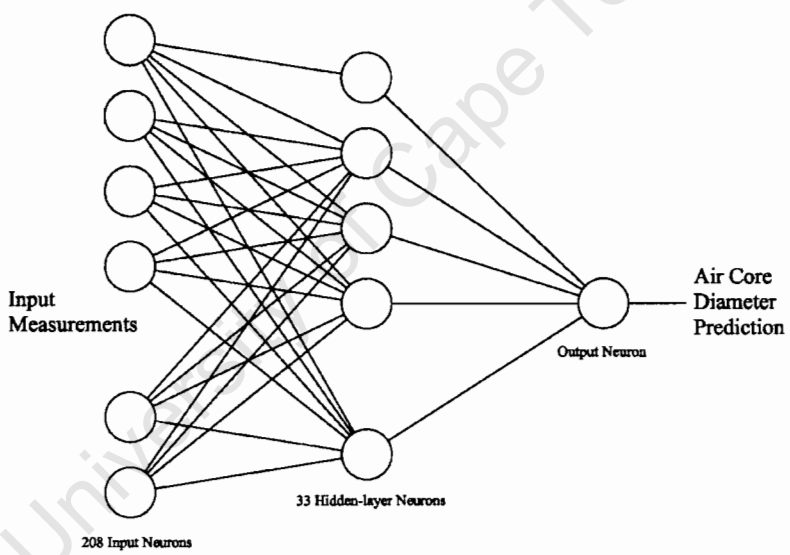

(b)

Figure 5.3.1: Diagram illustrating the structure of both the feed-forward neural networks used for predicting the air core diameter for the (a) FDM ERT and (b) TDM ERT systems respectively.

Now that the neural network structure has been addressed, it is time to look at the various functions and code written and used for training and simulating the neural networks and predicting the air core diameter.

The main reason that MATLAB was actually chosen as the coding platform, is because of MATLAB's neural network toolbox and the many built in neural network functions. This meant that all the complex neural network functions already existed and hence the author would not have to code them himself. In addition to this, Goldswain had also used MATLAB as his coding platform and as a result a very similar neural network had already been coded by him. This meant that some skeleton code existed and the author merely had to change and add code for both the FDM and TDM systems. Figure 5.3.2 shows a flow diagram which illustrates the process that was used for training and simulating the neural networks for both systems.

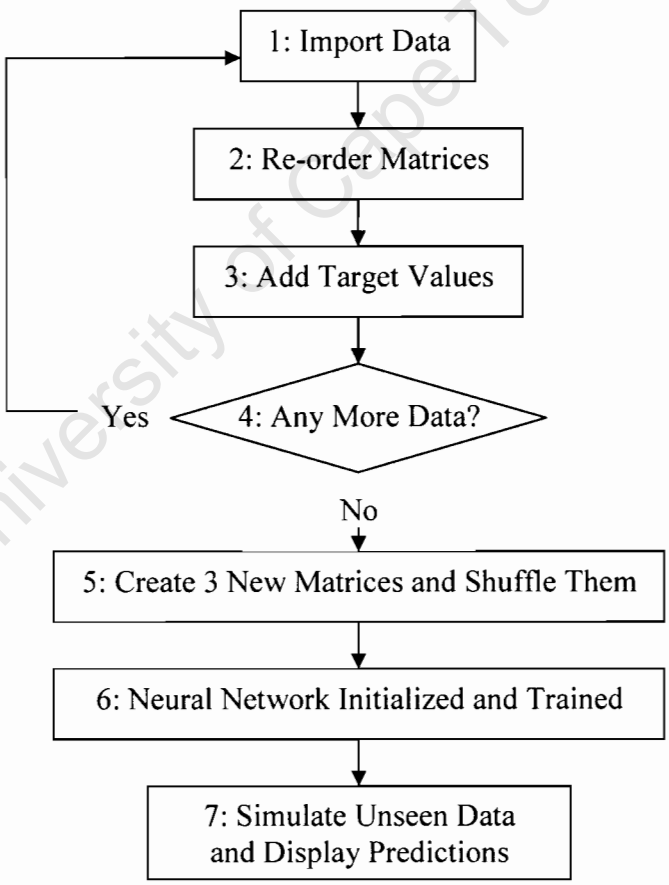

Figure 5.3.2: Flow diagram illustrating the process used for training and simulating the neural networks for both systems.

Data for training and simulation is captured in a dynamic manner. Polyethylene rods with various diameters are used to simulate air cores with the corresponding diameters. For each polyethylene rod (14 in total ranging from 5mm to 20mm in diameter) 7000 frames of data is collected. The rods are moved around inside the measurement space in random directions so that the entire measurement space can be covered. Each system saves the files containing the data under their specified file extension (TDM system - .tom and FDM system - .csv). It should be noted that the neural networks for both systems are trained separately and therefore no data is mixed up. The networks are then trained and simulated as follows (all relevant code can be found in appendix B):

1. First the data for one diameter size is loaded into the MATLAB workspace. In the case of the FDM system, the data is simply imported. For the TDM system, the 'LoadDataFile.m' function is used.
2. Then for the FDM system, the data is re-ordered (Re-order.m) so that it is presented to the network in a more orderly manner. In the case of the TDM system, the voltage data for each frame consists of 256 values. However only 208 of the 256 values actually correspond to measurement voltages. Therefore in this step the extra values imported for the TDM system are removed.
3. Thirdly the target values (diameter of the rod) are added to every frame of data.
4. Then it is time to see if all the data for each diameter rod has been imported. If there is still data remaining, steps 1-3 are performed until all data has been imported. If there is no more data to import, one can move on to step 5.
5. In the fifth step, three new matrices are created which correspond to training data (3000 frames), validation data (1000 frames) and simulation data (3000 frames). Each of the three matrices' rows

(each row corresponding to a frame) are then shuffled. This is so done so that the neural network is trained with randomized data, therefore making the training more realistic.

6. Now a feed-forward backpropagation neural network is created and the required training procedure is called to train the network. In this step it should also be noted that the targets and inputs for the network are separated. Four different training procedures were tested: standard training (no normalization), training with normalized data (inputs and targets), training with validation data (no normalization), and finally training with normalized data and validation data. All data which normalized is, is normalized with MATLAB's 'prestd' function. It should be noted that Goldswain wrote his own functions for normalizing data. Of the four training procedures it was found that the last option gave the best results. It should be noted that the resilient backpropagation technique is used to train the network.
7. In the final step, all the data which is held back for simulation is then simulated. This can be done in two different manners: one way is to simulate the data all at once, the other way is to simulate the data as if it were been done in a dynamic system, frame-by-frame. In the second manner, the data can be loaded into an AVI file and then played back. The major advantage of simulating the data in the second manner comes when simulating data from the TDM system. This is because the data can be simulated and each diameter prediction can be loaded into a movie file with the corresponding conductivity distribution image. Therefore when the AVI file is played back, for every frame you can see the diameter of the air core.

6 System Testing and Results

It was mentioned previously that when this project commenced, Goldswain was busy with the FDM ERT system and therefore the author would have to wait to do tests with the FDM system. Therefore, testing started on the TDM ERT system belonging to Wilkinson's EIT research group.

The initial tests on the TDM system were performed simply to see whether the system would be adequate in terms of its imaging capabilities for the De Beers research group's purposes. The tests consisted of simply placing different diameter polyurethane rods into the single-plane measurement vessel described in section 4.2.2. The measurement data from these preliminary tests was then reconstructed with the offline image reconstruction software and the images were examined to see whether one would be able to see the different diameter rods from the conductivity distribution. A screenshot of an image reconstructed from the measurements taken from the 5mm diameter rod can be seen in figure 6.1.

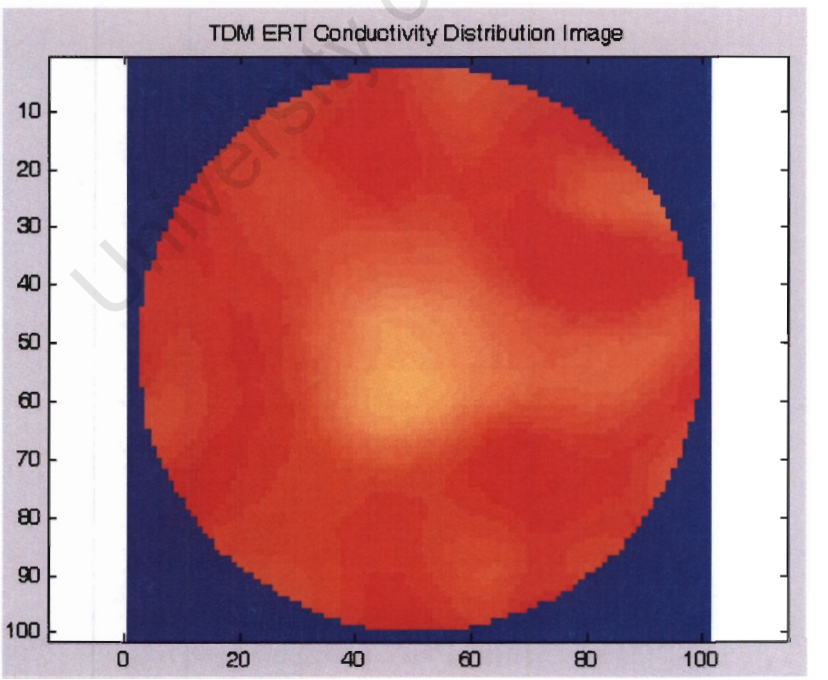

Figure 6.1: An image reconstructed in MATLAB showing the conductivity distribution caused by placing a 5mm diameter rod in the centre of the measurement vessel.

In the image in figure 6.1, it can be seen that conductivity decreases towards the centre of the image where the rod has been placed. It should be stated that all the initial tests were conducted in a static manner. No tests were conducted with rods of less than 5mm as it was assumed that the air core size for a cyclonic separator does not get smaller than that, and from the image one can see that the instrument is not very sensitive to non-conductive rods of less than 10% of the measurement vessels overall diameter (50mm). Figure 6.2 shows the comparison between 6 different diameter rods. The rods ranged from 5mm – 13mm in diameter. Each rod was placed in the centre of the vessel and the resultant data captured. The images were then reconstructed offline.

From the images, one can see that as the diameter of the rods increases, so the conductivity in the centre of the vessel decreases. In the images, red is associated with the maximum conductivity and navy blue is associated with a very low conductivity. Because these tests were successful the author decided that pixel-based approach to finding the air core diameter should be investigated at some stage.

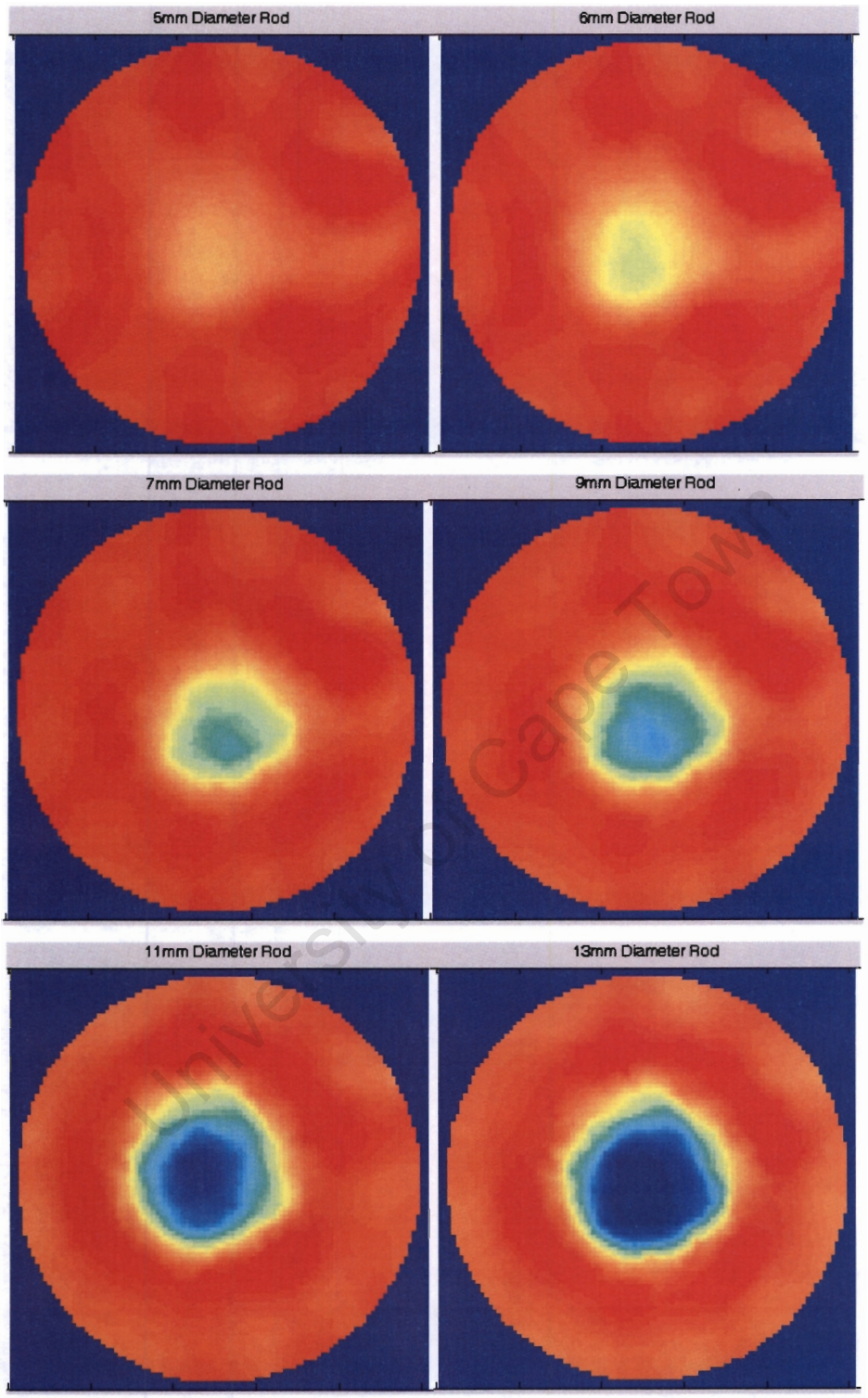

Figure 6.2: Reconstructed images showing how the conductivity distribution is affected by means of placing different diameter rods into the centre of the measurement vessel. Red is associated with high conductivity while blue is associated with a very low conductivity.

The next test was to see how the sensitivity of the TDM system was affected when the same diameter rod was placed in different positions within the vessel. The measurement strategy employed suggested that the instrument should be more sensitive when the rod is placed near the walls of the measurement vessel. Figure 6.3 shows the reconstructed images of these tests.

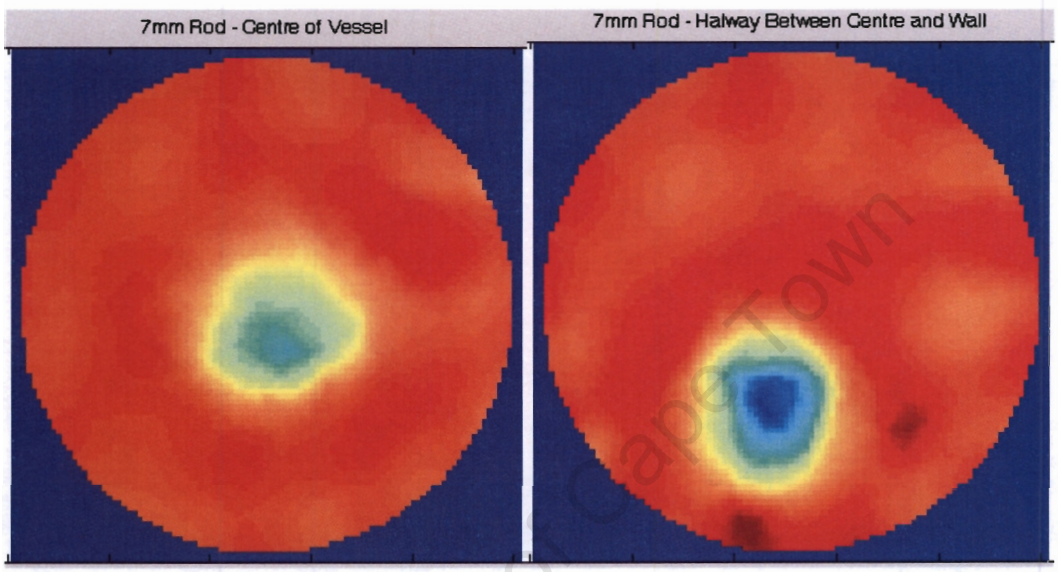

Figure 6.3: Reconstructed images showing the difference in sensitivity of the TDM ERT system when the same size rod is nearer to the vessel wall.

From the above images, one can see that the measurement strategy employed does indeed affect the sensitivity of the image.

After the above tests had been completed, it was decided that the pixel-based approach would be investigated on the images already acquired. All the reconstructed images have an image resolution (not true resolution) of 100×100 pixels. But because the vessel is circular, only 7500 of the 10000 pixels fall within the measurement space. Therefore if the diameter of the vessel is divided by the number of pixels pertaining to this diameter, one will find that each pixel is equal to 0.52mm. Therefore if the pixel-based approach is possible, the TDM system should be able to predict air core diameters to within a 0.52mm accuracy range. When the above images (figure 6.2) are considered it can be seen that a definite edge to the air core can not be distinguished. Therefore in order to

achieve a definite edge for visualization purposes, a conductivity threshold value needs to be engaged. Figure 6.4 show two reconstructed images where the threshold values have been engaged so that the correct diameter of the rods is shown in the images. Form the reconstructed images it can be seen that the rods do not appear perfectly circular, even though they are in reality.

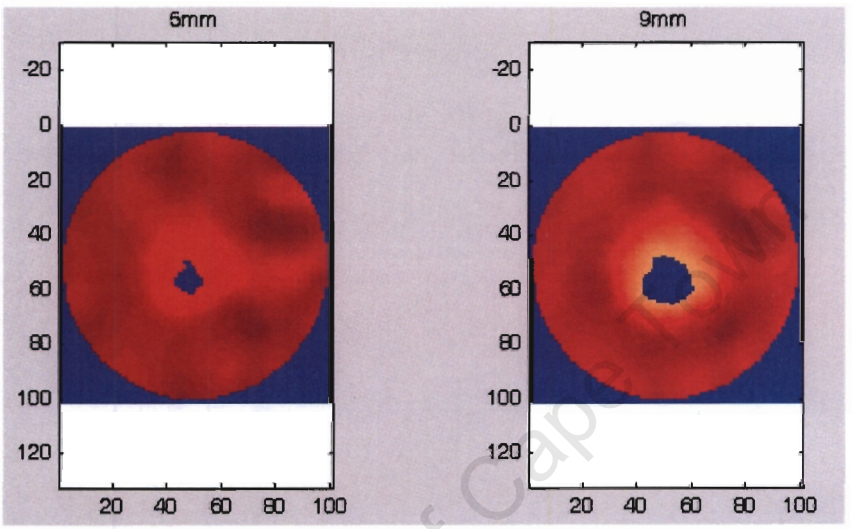

Figure 6.4: Reconstructed images with threshold values engaged.

Threshold values were engaged on all of the images displaying the different rod diameters used previously, both where the rods appeared in the centre, and near the walls of the measurement vessel. The threshold value for each diameter rod and the placement of the rod in the vessel was then recorded. These threshold values were then plotted in a 'Conductivity vs. Diameter' graph so that a conclusion could be made as to the relationship between the diameters and resulting conductivity values. Figure 6.5 illustrates this relationship. From the graph it can be seen that the threshold conductivity decreases in a rough logarithmic manner as the diameter of the respective rod increases.

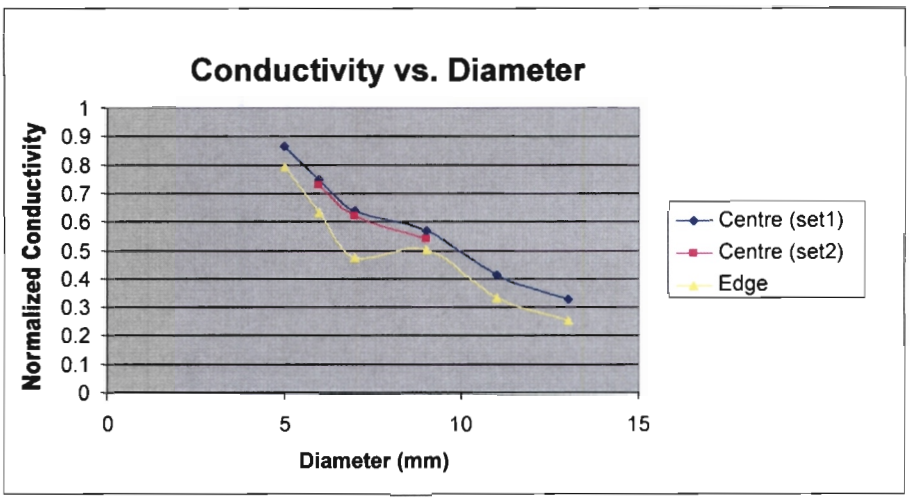

Figure 6.5: A plot showing the relationship between the threshold conductivity and rod diameter.

The above tests were all performed with water as the continuous fluid within the measurement vessel. Therefore based on the test results and from the plot, it can be concluded that if the conductivity of the continuous fluid remained the same throughout the measurement process, a pixel based approach to determine the air core diameter may be possible. However, because the project aims at determining the size of an air core within a cyclonic separator using ferosillicate slurry, and because the conductivity of the slurry depends on the slurry concentration, the pixel-based approach becomes a lot more complicated and unreliable. In addition to this, the pixel-based approach means that one has to wait for the images to first be reconstructed and would therefore slow the process of predicting the air core diameter down. Based on this it was decided that neural networks would give faster and more accurate results.

When a progress meeting with De Beers was held, the De Beers personal stressed the point that thus far, most of the testing for all the projects had been done in a static manner. Therefore they wanted to see dynamic testing and results with both water and slurry as the continuous fluid.

The initial dynamic testing was all done by means of moving the different diameter rods around the measurement vessel by hand. New reconstruction code was written that

enables the images to be reconstructed frame-by-frame and loaded into a movie sequence which could be played back in Windows Media Player. A screenshot of one of the movies can be seen in figure 6.6. In this movie, the 11mm diameter rod was used.

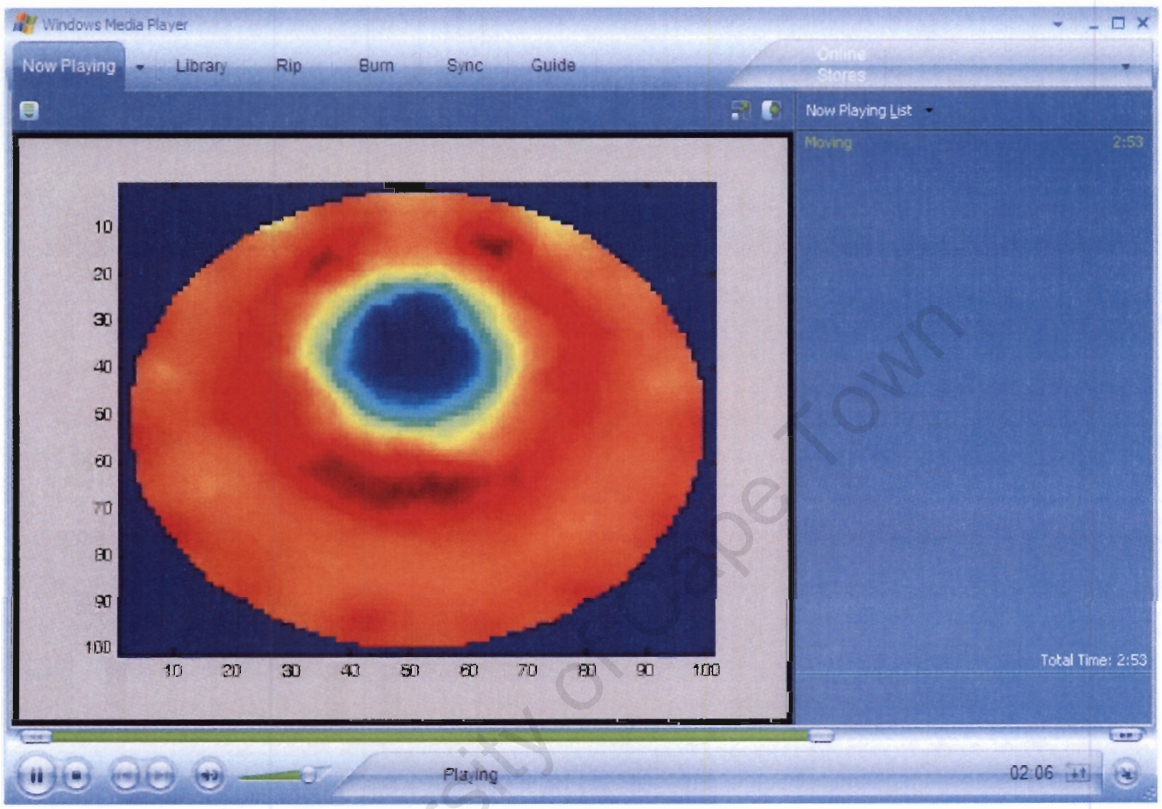

Figure 6.6: Screenshot showing on of the initial dynamic tests performed on the TDM ERT system. Here an 11mm rod is moved around the measurement vessel by hand.

Once the offline reconstruction code was working correctly, testing the newly constructed blender attachment became a priority. Shortly after the blender construction finished, the ferrosilicate powder from De Beers arrived. Therefore two tests had to be done with the blender. The first test was to see if the TDM system would be able to image the air vortex created by the blender when using water, and the second test was to see if the system would 'see' the vortex in the less conductive ferrosilicate slurry.

Figure 6.7 shows screenshots from movies of the two initial blender tests. It should also be noted that the movies can be reconstructed with surface plots instead of standard images. Screenshots of the surface reconstructed movies can be seen in appendix C.

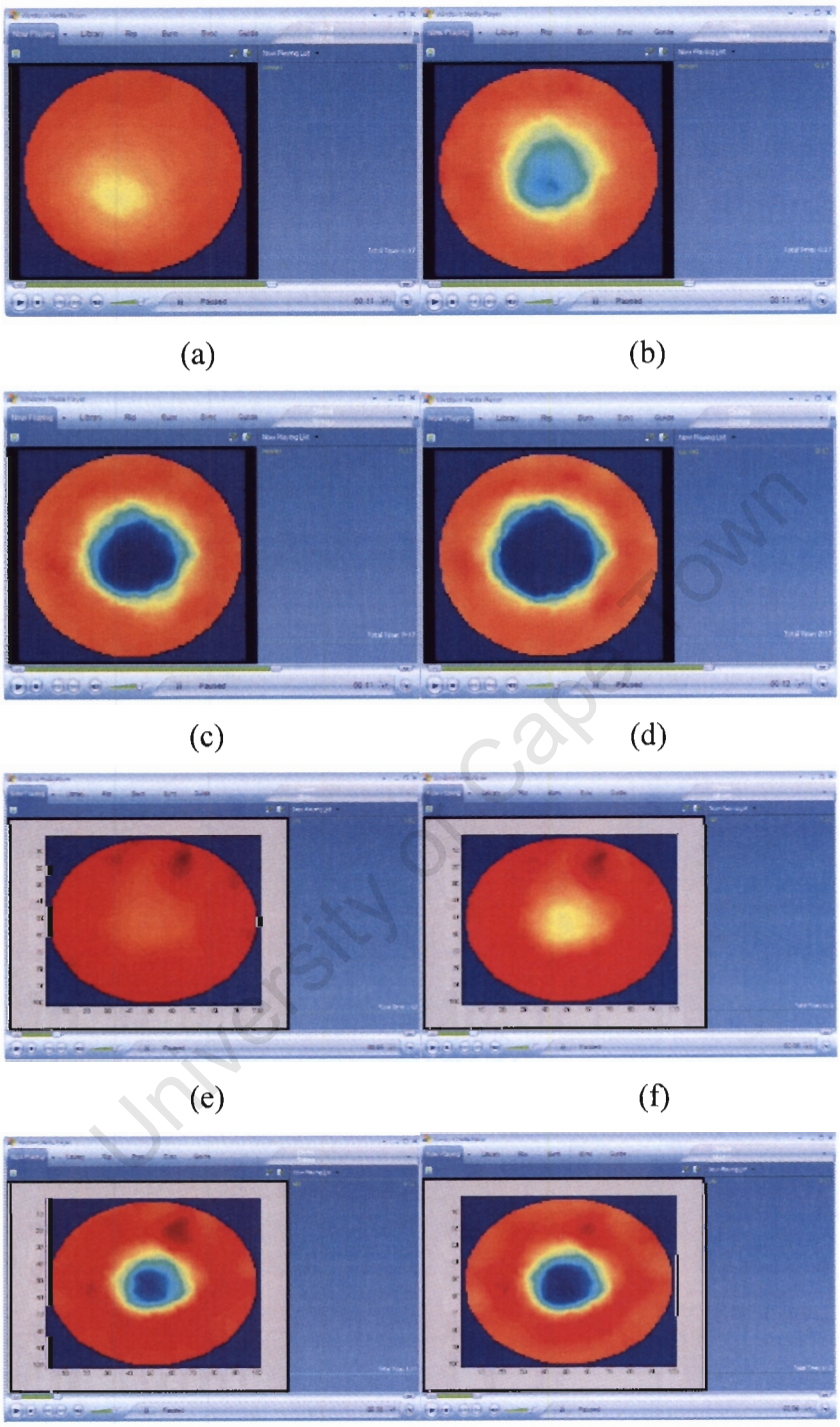

(a) (b)

(c) (d)

(e) (f)

(g) (h).

Figure 6.7: Screenshots from movies of the two initial blender tests showing the formation on the air core in water (a-d) and ferrosilicate slurry (e-h).

From figure 6.7, it can be seen that the air core appears to be much larger for water than for the ferrosilicate slurry. This is partly true. The reason the air core is smaller, is because the slurry is much denser. It should be noted that when the air core was observed through the top of the blender attachment, it was only slightly smaller than the air core formed in the water but it was much more unstable and oscillated greatly. Another reason that the air core appears smaller in the image is because the overall conductivity of the slurry is less than that of the water. By the time the author had completed the initial tests with the blender, Goldswain had finished his tests with the FDM ERT system. Therefore both systems were now available. However the next step in testing involved testing the 6-plane electrode rig which had been constructed.

The first test to be done on the six plane rig involved connecting the rig to the TDM system and just imaging ordinary water to see whether the electrodes were all wired correctly. Figure 6.8 shows a 6-plane reconstructed image captured from water.

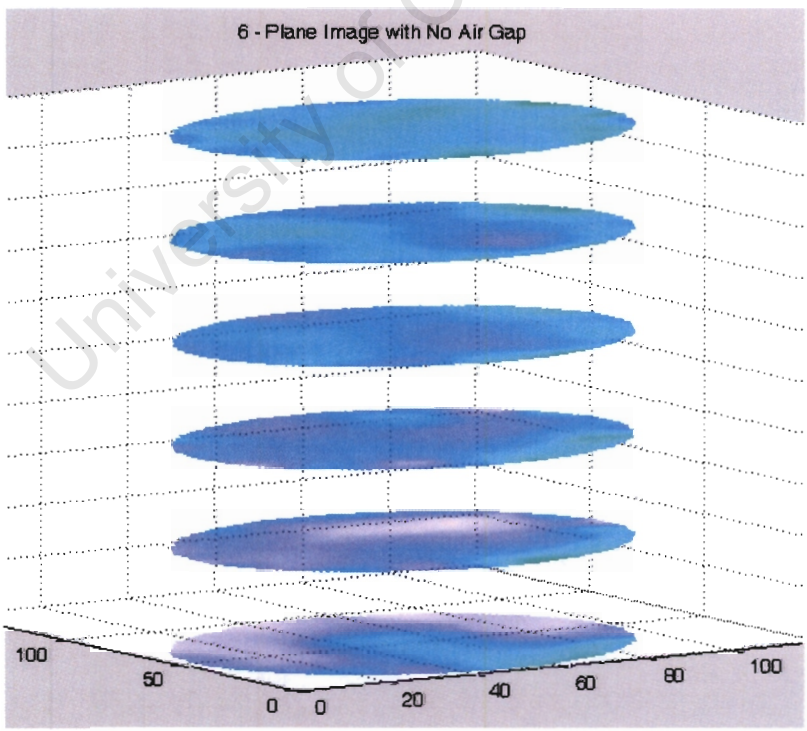

Figure 6.8: Reconstructed image showing the conductivity distribution on 6 different planes within the measurement vessel (data captured with the 6-plane electrode rig). The vessel contained ordinary water.

After the 6-plane rig was working, it was decided that more tests on the rig could be done after the neural networks were finished. Therefore, all focus shifted to coding, training and simulating the neural networks in order to make air core diameter predictions.

The first task in terms of the neural networks was to write new code or adapt the existing skeleton code so that the neural networks could be trained and simulated. Therefore once all the functions for pre-processing the data and training the networks had been written, it was time to construct new polyethylene rods. This time the rods ranged between 5mm-20mm in diameter. Fourteen rods in total were used in capturing the data. Figure 6.9 shows a picture of two of the rods.

Figure 6.9: Picture of two of the polyethylene rods used to train the neural networks. The rods ranged in diameter from 5mm to 20mm.

It was now time to capture all the data. The First Data that was captured was from the FDM ERT system. 7000 frames of data were captured for each individual rod and then 7000 frames of data were captured with the blender for simulation. For the FDM system no slurry was used. Once the data had been captured it was imported into MATLAB and the neural networks trained. Each of the neural networks for both the FDM and TDM system were trained for 400 epochs. Figure 6.10 shows a plot of the Mean Generalisation Error vs. Number of epochs and figure 6.11 shows the results of the unseen simulated data.

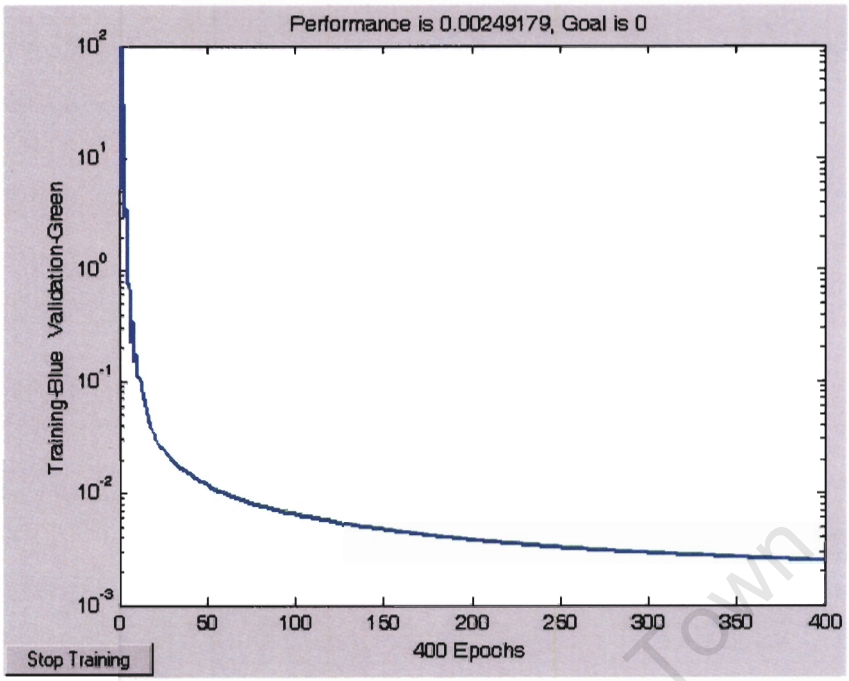

Figure 6.10: A plot of the mean generalisation error vs. number of epochs for the training of one of the networks. All training was done with validation data and early stopping so that the network could not be over-trained.

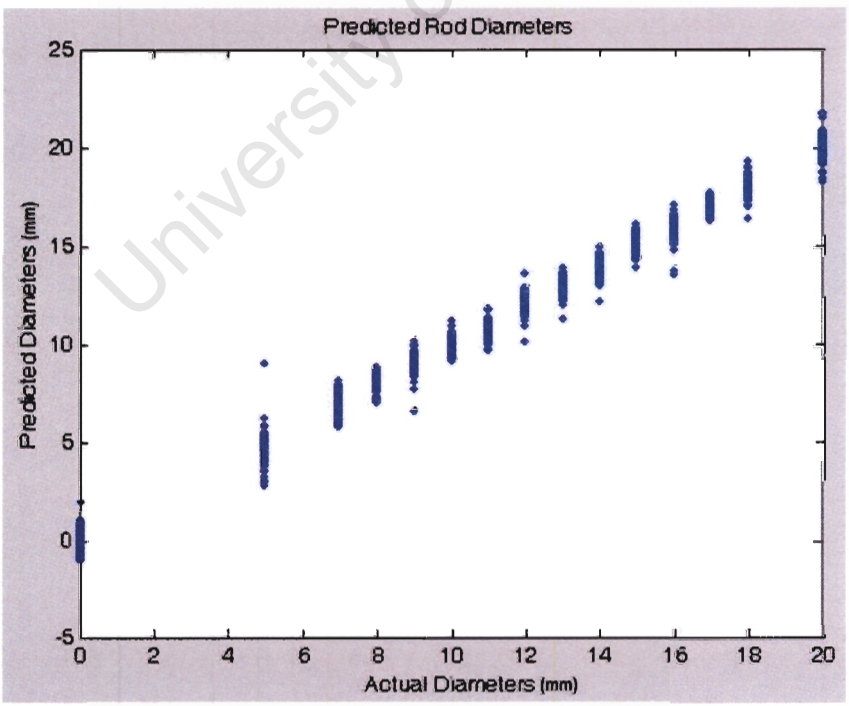

Figure 6.11: Plot of the predicted rod diameters (unseen data) vs. the actual rod diameters. Each diameter is represented by a blue dot.

From the results shown above, the trained network seems to have predicted the rod diameters fairly well. However to get a better idea of the network performance, one needs to look at the mean squared error (MSE) of prediction.

In order to make a complete evaluation of the training method, and in order to compare the FDM and TDM systems, it was decided that 10 separate networks should be trained for each of the two systems. Then, from these 20 networks, the best performing network for each system can be compared and a conclusion on the two tomography systems can be made. In addition to the comparison, these two networks will also simulate data from the blender to see how the systems cope with true process data.

The FDM systems networks were all trained first and the results can be seen in table 6.1 below.

Table 6.1: Mean squared error results for the FDM ERT system diameter predictions.

MLP Number	1	2	3	4	5	6	7	8	9	10
MSE on Diameter (mm)	0.0665	0.0682	0.0638	0.0818	0.0704	0.0940	0.0519	0.1155	0.0655	0.0728
Average MSE (mm)	0.0750									

From the above table, one can be seen that the all the networks predictions for the FDM system are very satisfactory as they yield low MSE's. It can also be seen that MLP 7 gives the best prediction results and will thus be used to simulate the blender data. Basically a MSE of 0.0519 means that the FDM system's diameter predictions are on average 0.2278mm off the actual diameter of the rods.

The average MSE above (FDM system) will be compared against the average MSE from the TDM system in order to determine which tomography system is more accurate. Figure 6.12 shows the results obtained when simulating the unseen data through the MLP 7.

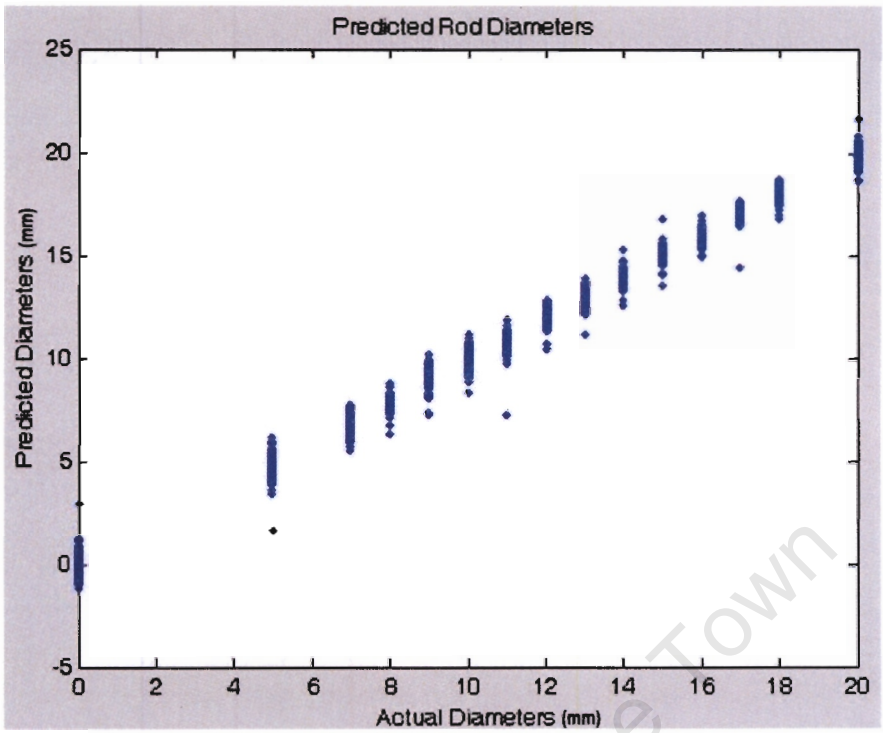

Figure 6.12: Plot of the predicted rod diameters (unseen data) vs. the actual rod diameters for the best performing MLP. Each diameter is represented by a blue dot.

Next, the blender data captured by the FDM ERT system was imported into MATLAB and simulated. The results were as follows:

Figure 6.13: A picture of the blender in motion. One can see the air core created in the centre of the single-plane electrode rig.

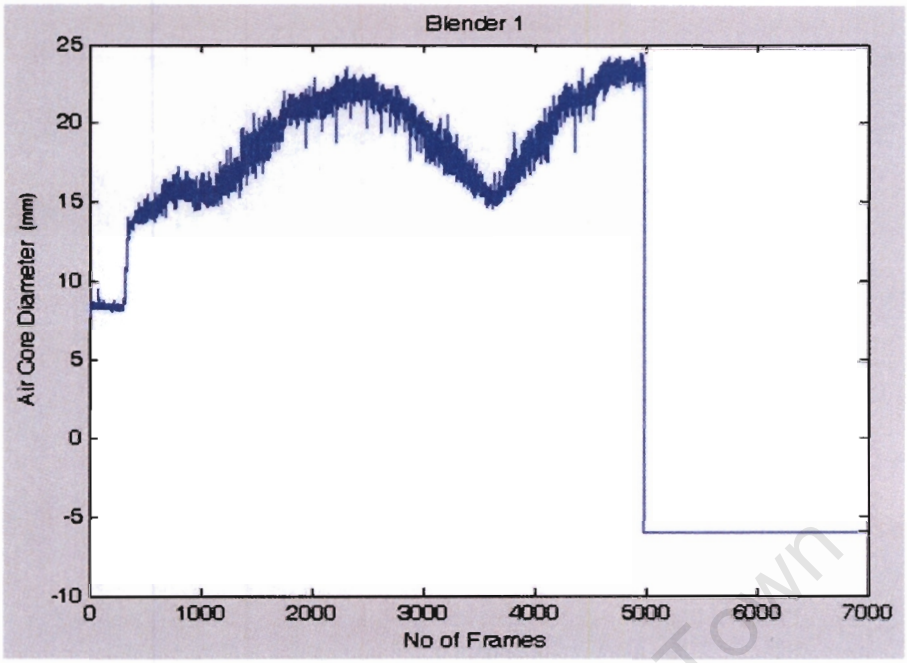

Figure 6.14: Plot of the air core diameter predictions (second set of blender data), predicted by the most accurate neural network for the FDM ERT system.

In figure 6.14 one can see the plot of the air core diameter predictions for the first set of data captured. If one looks at the graph, it can be seen that the FDM system predicts the following:

- Frames 0-312: An air core fluctuating between 8mm and 9mm.
- Frames 312-5000: Air gap increasing in size and fluctuating.
- Frames 5000-End: Air core diameter prediction of -6mm.

The visual observations made by the author while capturing the data for the above graph were as follows:

- Frames 0-312: No air core present, impeller rotating at a minimal velocity.
- Frames 312-5000: Air core begins to form until it becomes stable. Speed of impeller is then increased and air core increases as a result. Speed of impeller is then decreased and increased again and the air core follows respectively.
- Frames 5000-End: Impeller stopped and air core disappears completely

The second set of results from the FDM data were as follows:

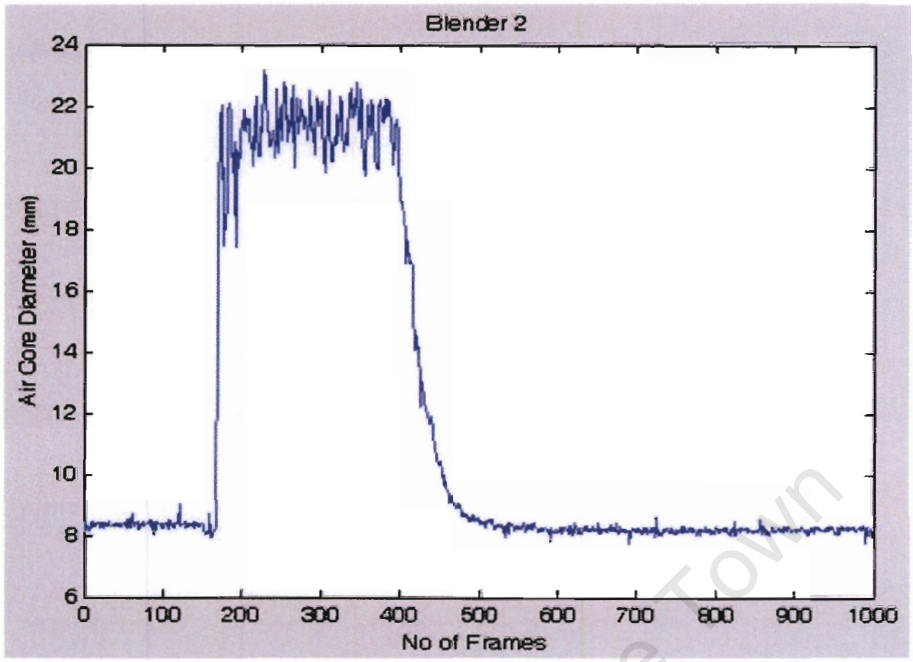

Figure 6.15: Plot of the air core diameter predictions (second set of blender data), predicted by the most accurate neural network for the FDM ERT system.

In figure 6.15 one can see the plot of the air core diameter predictions for the second set of data captured. If one looks at the graph, it can be seen that the FDM system predicts the following:

- Frames 0-166: An air core fluctuating between 8mm and 9mm.
- Frames 166-397: Air core increasing in size and then fluctuating.
- Frames 397-545: Air core diameter decreasing in size to between 8mm and 9mm.
- Frames 545-End: Air core fluctuating between 8mm and 9mm.

The visual observations made by the author while capturing the data for the above graph were as follows:

- Frames 0-166: No air core present, impeller rotating at a minimal velocity.
- Frames 166-397: Air core begins to form until it becomes stable. Speed of impeller is then kept constant.
- Frames 397-545: Impeller stopped and air core starts to disappear.
- Frames 545-End: Air core disappeared completely, no air core present.

When the predictions of the data captured by the FDM ERT system are compared with the visual observations, it can be suggested that the noise created by the blender motor causes small changes in the measurement signals captured and thus when there is no core present (visually), an air core is predicted (by the FDM system). However no conclusion can be made as to how the noise affects the predicted diameter of the air core when the air core forms. This is because the exact diameter of the air core, once fully formed, is unknown and a separate external measurement system would be needed to determine the exact visual size of the core.

By simply altering the code which displays the images (from the TDM system) dynamically and places them into an AVI movie file, the author was able to get the neural network to predict the blender data in a dynamic manner and then save it to a movie file which could be played, at a later stage, in Windows Media Player. It should be noted that for each diameter prediction, the corresponding input signals for the neural network were plotted underneath and saved into the movie file. Figure 6.16 shows a screenshot of the movie file created.

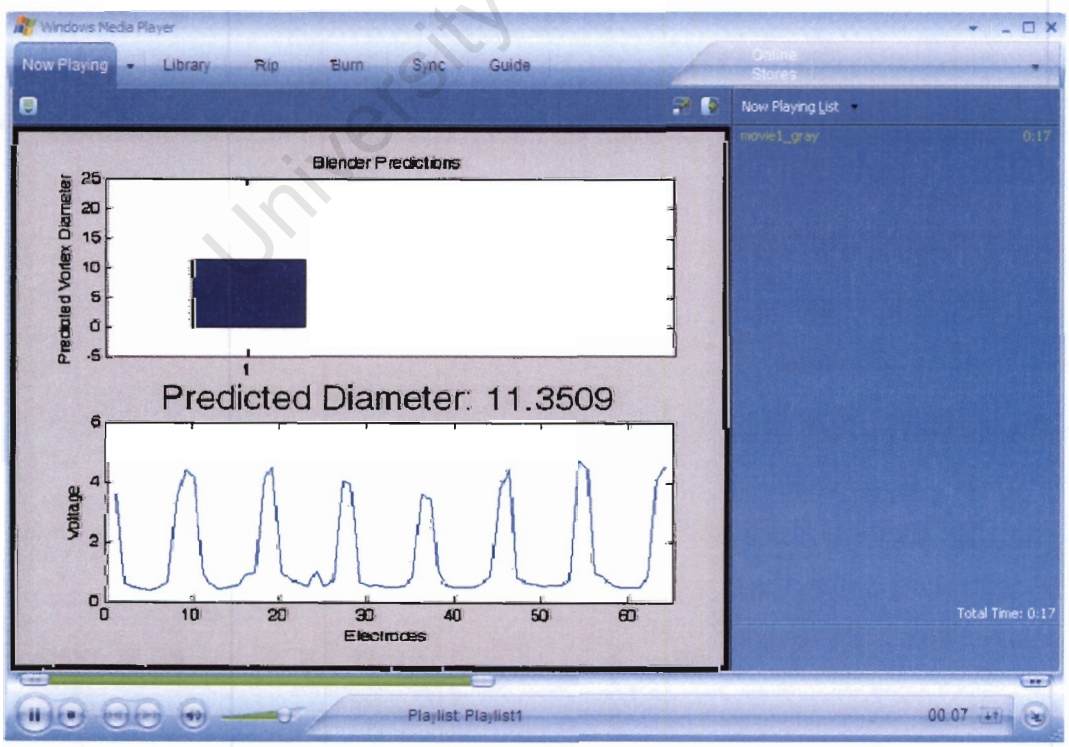

Figure 6.16: Screenshot from movie showing dynamic air core predictions.

Once all the FDM networks had been tested, it was time to train and simulate the data captured by the TDM ERT system. First the networks were trained with the captured rod data from the single-plain electrode set. Then the unseen rod data was simulated.
The MSE results from the 10 trained networks were as follows (table6.2):

Table 6.2: Mean squared error results for the TDM ERT system diameter predictions.

MLP Number	1	2	3	4	5	6	7	8	9	10
MSE on Diameter (mm)	0.2802	0.2802	0.3792	0.3384	0.4640	0.3415	0.2945	0.3460	0.2930	0.3576
Average MSE (mm)	0.3375									

From the above table, it can be seen that the network diameter predictions are not nearly as impressive as the FDM ERT system prediction results. It can also be seen that MLP 1 and MLP 2 give the best prediction results. It can also be seen for the results that the MSE of MLP 1 and MLP 2 is 0.2802, meaning that the TDM system's diameter prediction will be on average 0.5293mm off the actual diameters of the rods. Because MLP 1 and MLP 2 both had the same MSE's, it didn't matter which network was used to simulated the blender data. However, it should be noted that MLP 2 was used. Figure 6.17 shows the results obtained from MLP 2 when simulating the unseen data from the polyethylene rods.

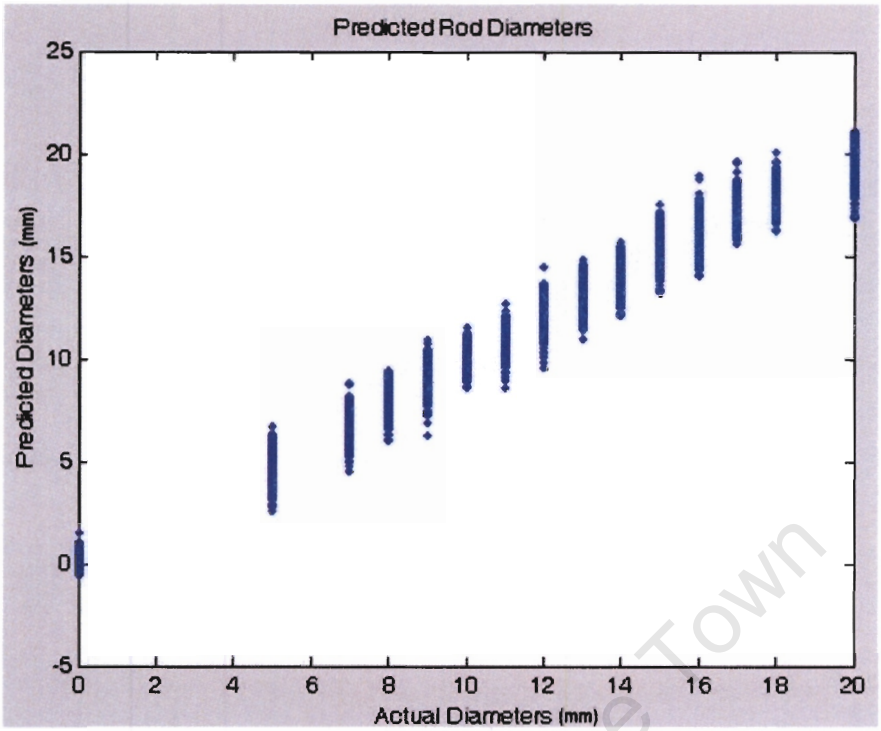

Figure 6.17: Plot of the Predicted Rod diameters (unseen data) vs. The Actual Rod Diameters for the best performing MLP. Each diameter is represented by a blue dot.

Once all the unseen rod data had been simulated, attention moved to processing the blender data captured by the TDM system. First the data captured with the blender containing water was processed, and then ferrosilicate slurry data. It should be noted that as with the FDM system, two sets of data for the blender (containing water) were captured with the TDM system.

The results from the water follow on the next page.

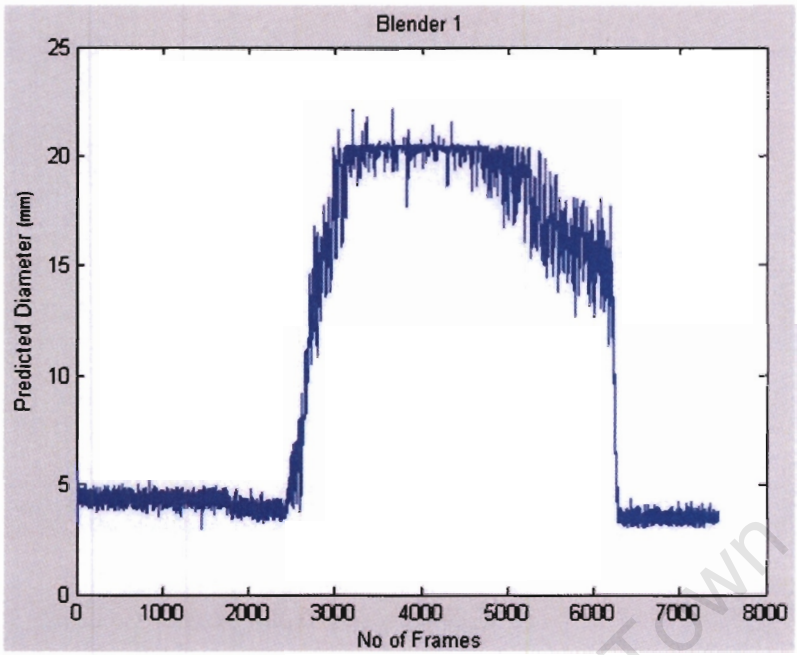

Figure 6.18: Plot of the air core diameter predictions (first set of blender data containing water), predicted by the most accurate neural network for the TDM ERT system.

In figure 6.18 one can see the plot of the air core diameter predictions for the first set of data captured. If one looks at the graph, it can be seen that the TDM system predicts the following:

- Frames 0 – 2450: An air core fluctuating between 3mm and 5mm.
- Frames 2450 - 3110: Air core increasing in size and fluctuating.
- Frames 3110 - 4750: Air core diameter stable and fluctuating in size between 19mm and 21mm.
- Frames 4750 - 6200: Air core gradually decreasing in size.
- Frames 6200 – End: air core decreases in size and fluctuates between 3mm and 4mm.

The visual observations made by the author while capturing the data for the above graph were as follows:

- Frames 0 – 2450: No air core present, impeller rotating at a minimal velocity.

- Frames 2450 - 3110: Impeller speed increased to a maximum and air core begins to form.
- Frames 3110 - 4750: Stable air core, impeller speed constant.
- Frames 4750 - 6200: Impeller speed gradually decreasing and air core gradually decreasing.
- Frames 6200 – End: Impeller slowed to minimal speed and eventually stopped, air core quickly disappears.

The results from the second set data where the blender contained water were as follows:

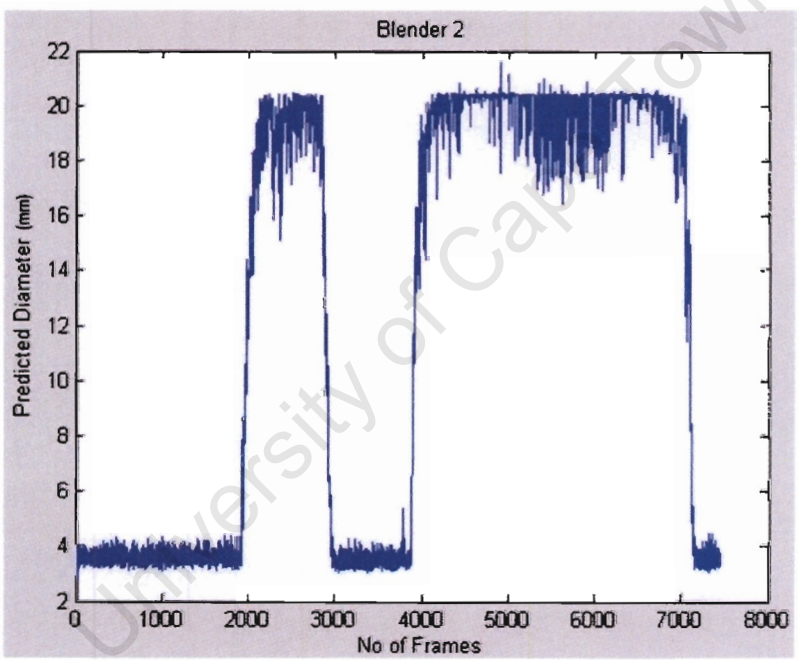

Figure 6.19: Plot of the air core diameter predictions (second set of blender data containing water), predicted by the most accurate neural network for the TDM ERT system.

In figure 6.19 one can see the plot of the air core diameter predictions for the second set of blender data captured. If one looks at the graph, it can be seen that the TDM system predicts the following:

- Frames 0-1900: An air core fluctuating between 3mm and 4mm.
- Frames 1900-2100: Air core increasing in size and fluctuating.

- Frames 2100-2830: Air core diameter fluctuating in size between 18mm and 20.5mm.
- Frames 2830-3860: Air core diameter decreases in size and fluctuates between 3mm and 4mm.
- Frames 3860-6880: Air core increases in size, becomes stable and fluctuates between 17mm and 20.5mm.
- Frames 6880-End: Air core diameter decreases in size and fluctuates between 3mm and 4mm.

The visual observations made by the author while capturing the data for the above graph were as follows:

- Frames 0-1900: Blender switched on and impeller rotating at minimum speed, no air core present.
- Frames 1900-2100: Impeller speed increased to a maximum, air core forms quickly.
- Frames 2100-2830: A stable air core is formed.
- Frames 2830-3860: Blender switched off, impeller stops, air core disappears.
- Frames 3860-6880: Blender switched on again and impeller rotates at maximum speed and a stable air core forms.
- Frames 6880-End: Blender switched off, impeller stops rotating and air core disappears completely.

The results from the third set of data where the blender contained ferrosilicate slurry were as follows:

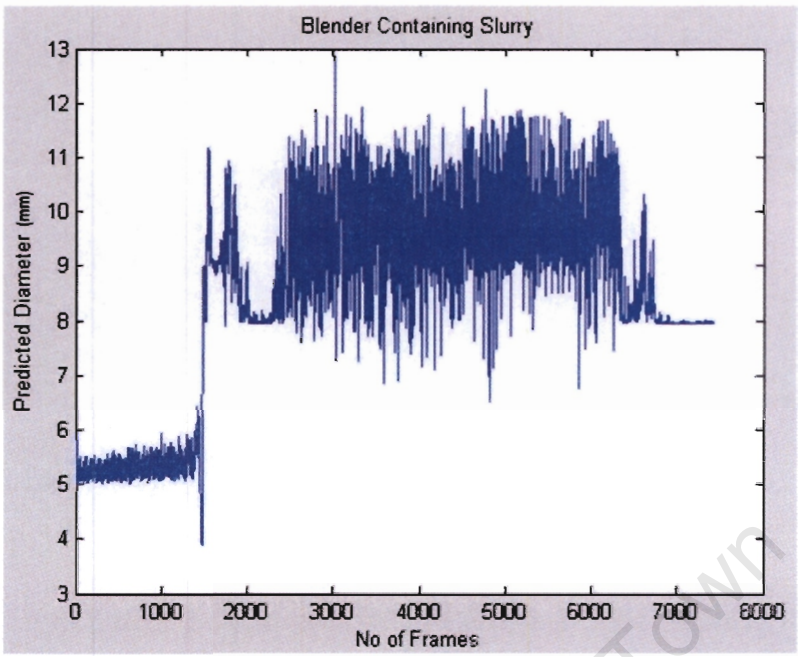

Figure 6.20: Plot of the air core diameter predictions (blender containing slurry), predicted by the most accurate neural network for the TDM ERT system.

From figure 6.19 one can see the plot of the air core diameter predictions for the third set of blender data captured. If one looks at the graph, it can be seen that the TDM system predicts the following:

- Frames 0-1400: Air core diameter fluctuating in size between 5mm and 6mm.
- Frames 1400-2000: Air core diameter increases and fluctuates 8mm and 11mm.
- Frames 2000-2300: Air core stabilizes and fluctuates very slightly between 7.95mm and 8.2mm.
- Frames 2300-6740: Air core diameter increases, becomes incredible unstable and fluctuated between 7mm and 12mm.
- Frames 6740-End: Air core stabilizes and fluctuates very slightly between 7.95mm and 8.2mm.

The visual observations made by the author while capturing the data for the above graph were as follows:

- Frames 0-1400: Impeller rotating slowly, no air core present.

- Frames 1400-2000: Impeller rotating at maximum speed, air core present and oscillating.
- Frames 2000-2300: Impeller slowed down slightly, air core disappeared.
- Frames 2300-6740: Impeller rotating at maximum speed, air core incredibly oscillatory.
- Frames 6740-End: Blender switched off, impeller stops rotating, air core disappears totally.

When all the predictions made by the TDM captured data are compared with the visual observations, it is once again suggested that the blender motor creates interference noise, and as a result the network predicts an air core when no air core exists. The question still remains though as to how much the noise affect the predictions when the air core is present. Therefore an external measurement system (unaffected by noise) is needed to determine the visual size of the air core.

From both the three measurement sets, it was observed that when the blender contains the slurry, the air core is much smaller and much more unstable. This is probably due to the fact that the slurry is so dense.

When the two tomography systems are compared (average MSE's for both systems), it can be seen that the FDM system far outperforms the TDM system when the polyethylene rod data is simulated. In addition to this, the FDM system also seems to be far less susceptible to noise. A possible reason for the FDM system outperforming the TDM system could be that there are extra voltages from the TDM system which influence the training of the neural networks in a negative way and should as a result be disregarded. It should be stated that the extra voltages are definitely needed for improved image reconstruction.

The last two tests performed on the TDM system involved simulating captured data (both water and slurry data) through the neural network in a 'dynamic' manner (for the single-plane rig) and reconstructing the 6-plane image data and loading it into AVI movie files.

For the single-plane dynamic prediction tests, each diameter prediction along with its corresponding reconstructed image for each frame of data was loaded into an AVI movie file which could be played back in Windows Media Player.

Figure 6.21 shows a screenshots of the movie files created where the blender contained (a) water and (b) ferrosilicate slurry.

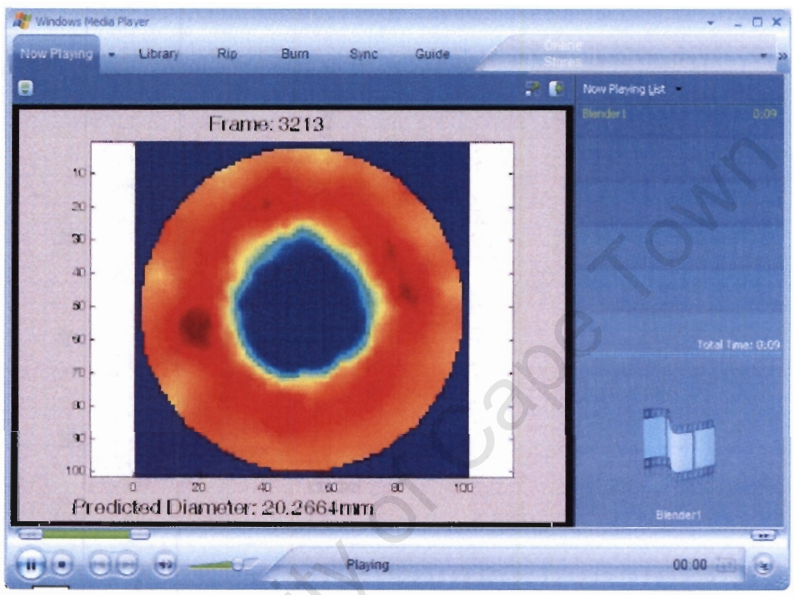

(a)

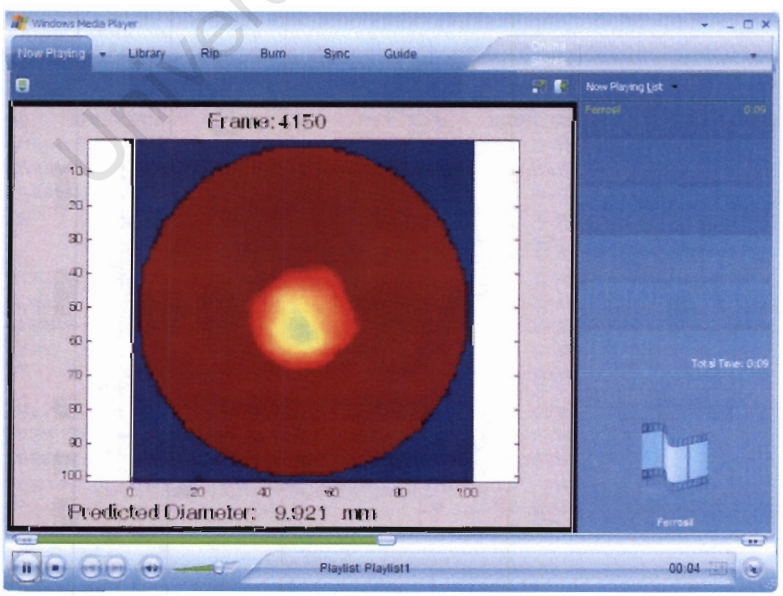

Figure 6.21: Screenshots of the movies showing dynamic air core predictions for TDM system when blender contained (a) water and (b) ferrosilicate slurry.

From the above images it can be seen how much less conductive the slurry is as well as how much smaller the air core is when the blender contains ferrosilicate slurry.

Figure 6.22 on both this and the following page, shows a sequence of screenshots from the movie file created for the 6-plane electrode rig. The movie shows an air core forming as the impellor speed of the blender (containing water) increases.

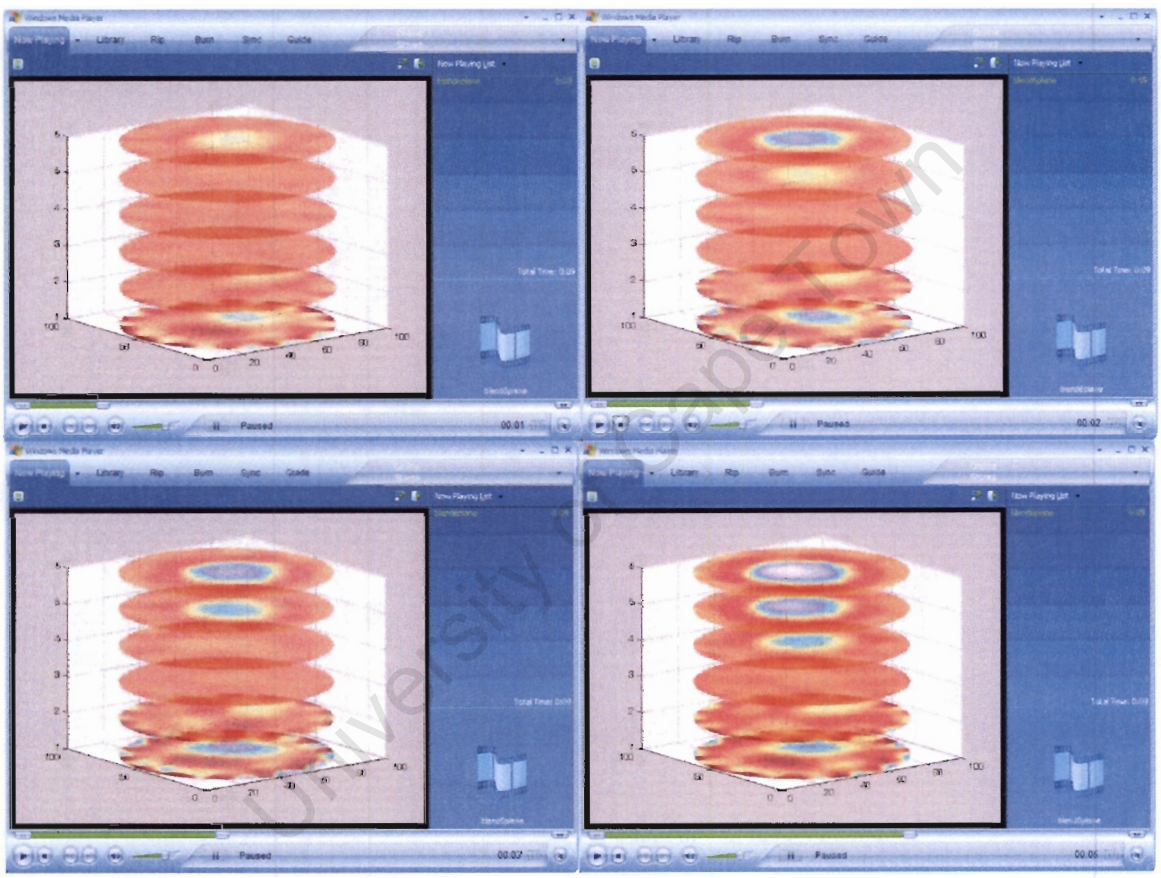

(Figure continued on the following page.)

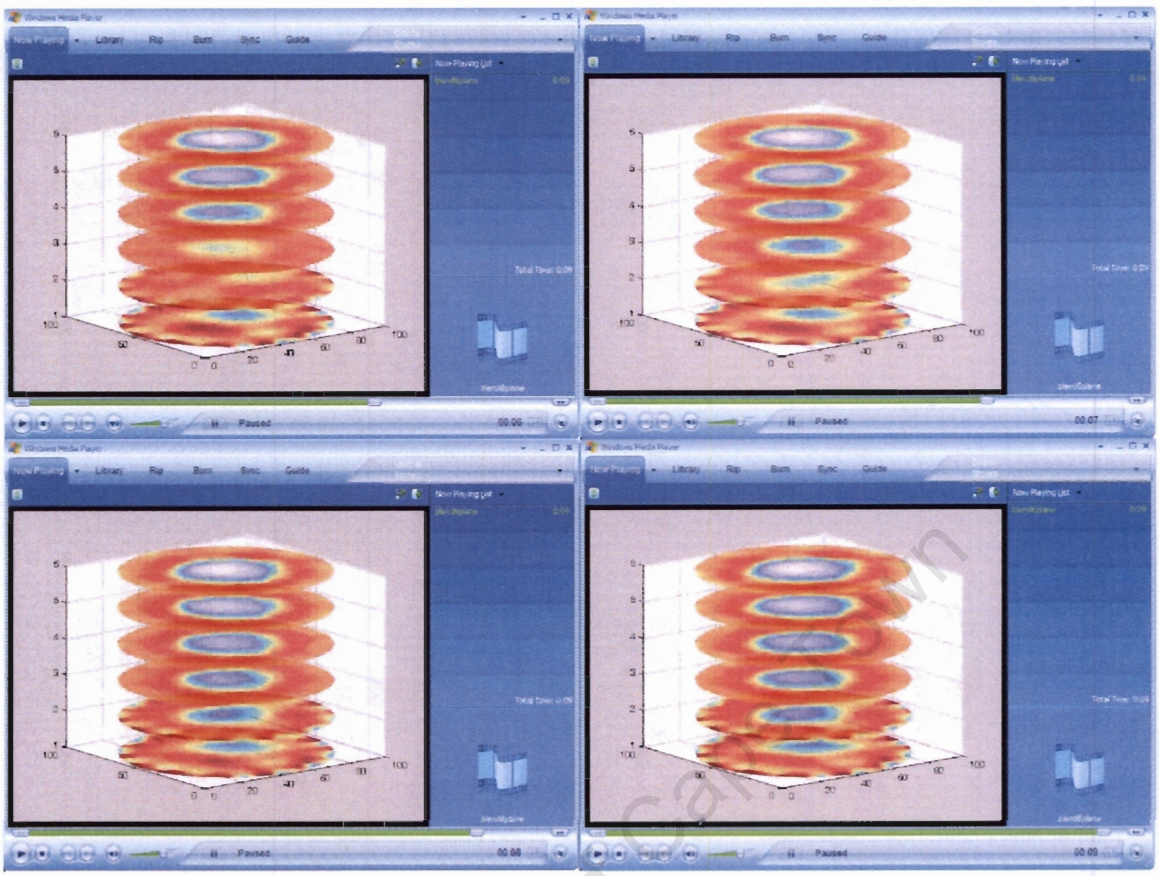

Figure 6.22: A sequence of screenshots from a movie of an air core forming inside the 6-plane rig (containing water). The first two images show the air core starting to form on the top plane and then make its way down to the bottom electrode plane.

It should be stated that one can see some interference on the lower two planes as a result of the impeller.

From all the tests it can be seen that both the FDM and TDM systems have great potential. The 6-plane data still needs to be processed and simulated through the neural network in order to get air core diameter predictions, but first some of the TDM input measurements need to be discarded as they only cause confusion and complicate both the network training and make the diameter predictions less accurate.

7 Conclusions

The ultimate goal of this ongoing project is to control a cyclonic separator by means of monitoring the air core formed inside the process device. Because of the nature of the process for which these separators are used, it is not possible to gain access and place many measurement systems in or on the process vessel. This project dealt with two electrical resistance tomography systems which have non-invasive measurement protocols and therefore can be used to monitor the cyclonic separator air core. Therefore, based on the foregoing information, results and observations, the following conclusions could be made:

7.1 The air core can be used to determine the performance of cyclonic separator.

From all the literary evidence, it can be seen that the air core of a cyclonic separator has a huge influence on the device's operating state, and hence is a good indicator of the device's separation efficiency.

7.2 Both the FDM ERT and TDM ERT systems are capable of detecting the air core.

From the results one can clearly see that both ERT systems can detect the presence of an air core. For the FDM system, no image is present, but a diameter prediction is made based on the signal measurements made by the system. For the TDM system, the reconstructed image shows the presence of the air core and if the measurement signals are observed, they too can be used to show and make a prediction on the diameter of an air core.

7.3 A pixel-based approach to determining the size of the air core is inaccurate.

When the pixel-based approach was used on the conductivity distribution images reconstructed from the TDM ERT system, it was found that there were too many variables that play a role in order to make a quick and accurate air core diameter prediction. These variables include: the fact that the conductivity in a slurry solution is constantly changing, and the conductivity gradient in the reconstructed images does not show a definite air-fluid interface boundary. It was even found that if a conductivity threshold value is set for the interface boundary, as soon as the conductivity or the air core size changes, the threshold value needs to be updated, therefore leading to an inaccurate diameter prediction. In addition to this, with the pixel-based approach, an image first has to be reconstructed before a prediction can be made. As the reconstruction algorithms are complex, much time is needed for the reconstruction and hence the diameter prediction time required is significantly increased. One can conclude from the above factors that this approach is too slow and inaccurate, even with a fast tomography system, to control any cyclonic separation process.

7.4 Neural Networks are good alternative for predicting the air core diameter.

From all the previous research results from the De Beers research group dealing with this project, and from the results and observations made by the author, it can be seen that neural networks provide an excellent approach to predicting the diameter of a cyclonic separator's air core. The reason for this is that the neural network, once trained, takes the initial measurements made by the tomography system as its inputs and because the network is much quicker in processing, a prediction is made very quickly and more accurately than many other methods. Although the networks are not always correct, the results did show that the errors

only varied on average between 0.2278mm and 0.5293mm on the diameter predictions.

7.5 The blender is a good alternative for testing the ERT systems capabilities instead of using the hydrocyclone.

The observations made when using the blender, showed that the air vortex formed displayed many similar characteristics to that of an air core inside a cyclonic separator. These characteristics include: the air core only forms once the fluid has reached a certain critical rotational velocity; the core does not dissipate until the rotational velocity decreases to another critical velocity smaller than the initial velocity needed to form the core; and the air core is very oscillatory. The major advantage of the blender is that one can easily observe the air core, regardless of the fluid being processed. This is because it is easy to gain access to the process from directly above, so one can observe the process or even fit another measurement strategy to the system in order to make a comparison to the tomography system being used at the time.

7.6 The FDM system outperforms the TDM system with respect to accuracy and noise.

From the results it is easy to see that the FDM system (0.2278mm average prediction error) outperforms the TDM system (0.5293mm average prediction error) with respect to the diameter predictions. The FDM also was much less affected by the noise of the blender than the TDM system. The most likely reason for the TDM system not performing as well is the fact that there are so many more inputs into its respective neural network. If some these inputs were selectively chosen and the rest discarded, it would probably result in a much more accurate diameter prediction for the TDM system.

7.7 Both systems have their advantages for monitoring the air core.

The results show that the FDM system is more accurate, but there are some advantages that the TDM system does offer. These advantages include the TDM system being able to capture data at rates of around 1000 fames per second (FDM system only captures data around 200 frames per second) and the fact that TDM system offers an image. With further software development, the FDM system could definitely offer image reconstruction, but the image resolution would be less than that of the TDM system as the FDM system takes fewer measurement readings.

7.8 Monitoring a cyclonic separator can definitely be done by both systems, but the systems need to be further developed in order to control the separation devices.

The results do definitely show that both systems are capable of monitoring cyclonic separation processes with respect to the air core formed inside the separation devices. However both the ERT systems are not nearly accurate enough to control the separation process based on the air core formation. A further question that remains is that even if the systems were accurate enough; would one be able to control the process based on the diameter of the air core? Or would the control of the separation process be based on the fact that a stable air core runs from the underflow to the overflow of the cyclonic separator?
Hence the reason for a multi-plane ERT electrode rig.

8 Recommendations

Although many of the various objectives for the research were met, there are still many aspects that still need to be investigated. On the basis of the above conclusions, the following recommendations are made:

8.1 More image reconstruction techniques need to be researched and tested.

When all the literature is considered, there is only one other technique for ERT that seems to have shown good results in terms of air core diameter predictions. This technique is that of Parametric Modelling employed by Williams et al. [21]. The technique needs to be looked at in greater detail as it may be beneficial if it were combined with the neural network technique used in this paper.

8.2 The neural network for the TDM system needs to be re-designed.

The measured voltage signals captured by the TDM system need to be investigated and some need to be discarded. The neural network then needs to be re-designed. These changes should make the neural network both quicker and simpler to train and would most likely greatly improve the diameter prediction results for the TDM system.

8.3 An additional visual and measurement system needs to be fitted above the blender.

Because one can easily observe the air vortex from above the blender, a camera should be fitted above the unit. This would mean that the recorded video could be played back and the exact diameter of the air core determined frame-by-frame.

This diameter could then be compared to the air core predicted by the neural network for every frame. In addition to this, the data could be used to train the neural network with proper process data, rather than with polyethylene rods.

8.4 The FDM system hardware needs to be re-designed.

The FDM system hardware is older and slower than the TDM system hardware. Therefore the FDM system hardware needs to be re-designed and updated. This would most likely greatly increase the speed that the FDM system can capture data at, and probably increase its accuracy too.

8.5 The 6-plane rig needs to be used to make diameter predictions.

The 6-plane rig has not been used to predict the air core diameter yet. Therefore once the neural networks for the TDM system are more accurate, the 6-plane rig should be used to make diameter predictions with both water and slurry.

8.6 Another blender unit should be designed.

The reason for this recommendation lies with the fact that if the blender motor were to be moved further away from the ERT hardware, and if the impellor is moved further form the electrodes, the captured data may be less noisy and better results will be obtained.

8.7 Once the ERT system's diameter predictions are more accurate, they need to be fitted to a hydrocyclone.

Once both the ERT system's diameter predictions are more accurate, the systems need to be fitted to a hydrocyclone to determine whether the device's separation efficiency would greatly improve if the air core diameter was carefully controlled.

Or whether it would be better to control the device based on an air running from the underflow to the overflow of the cyclonic separator.

References

[1] D.J. Ashlin. *Three phase cyclonic separator*, [Online] Available: http://www.freepatentsonline.com/6348087.html [2005, 15 December]

[2] Metso Minerals, *Separation*, [Online] Available: http://www.metsominerals.com/inetMinerals/mm_home.nsf/FR?ReadForm&ATL=/inetMinerals/mm_segments.nsf/WebWID/WTB-041213-2256F-B42B4 [2005, 15 December]

[3] B. Wilson, J. Zhou, L. Willis, J. Wimer. *Hydrocyclone Separators*, [Online] Available: http://www.wsu.edu:8080/~gmhyde/433_web_pages/cyclones/CycloneRptTeam5.html [2006, January 20]

[4] P.R. Stiffens, W.J. Whiten, S. Appleby, J. Hitchins. *Prediction of air core diameters for hydrocyclones*, International Journal of Mineral Processing 39 (1993) pp. 61-74

[5] A. Barrientos, R. Sampaio, F. Concha. *Effect of the air core on the performance of a hydrocyclone*, XVIII International Mineral Processing Congress (18^{th} : 1993 : Sydney, N.S.W), 1 (1993) pp. 267-270

[6] T. Dyakowski, R.A. Williams. *Prediction of air-core size and shape in a hydrocyclone*, International Journal of Mineral Processing 43 (1995) pp. 1-14

[7] F. Concha, A. Barrientos, J. Montero, R. Sampaio. *Air core and roping in hydrocyclones*, International Journal of Mineral Processing 44-45 (1996) pp. 743-749

[8] E.M. Sevilla, R.M.R. Branion. *The fluid dynamics of hydrocyclones*, Journal of Pulp and Paper Science 23 (1997) pp. J85-J93

[9] W. Kraipech. *The experimental study of the flow within a hydrocyclone*, Department of Chemical Engineering, Srinakharinwirot University Ongkharuk, Nakornnayok 26120, Thailand (2004)

[10] Th. Neesse, V. Golyk, P. Kaniut, V. Reinsch. *Hydrocyclone control in grinding circuits*, Minerals Engineering 17 (2004) pp. 1237–1240

[11] H.I. Schlaberg, M. Yang, B.S. Hoyle, M.S. Beck, C. Lenn. *Wide-angle transducers for real-time ultrasonic process tomography imaging applications*, Ultrasonics 35 (1997) pp. 213-221

[12] M. Yang, H.I. Schlaberg, B.S. Hoyle, M.S. Beck, C. Lenn. *Real-time ultrasound process tomography for two-phase flow imaging using a reduced number of transducers*, IEEE Transactions on Ultrasonics, Ferroelectrics, and Frequency Control 46 (1999) pp. 492-501

[13] H.I. Schlaberg, F.J.W. Podd, B.S. Hoyle. *Ultrasound process tomography system for hydrocyclones*, Ultrasonics 38 (2000) pp. 813–816

[14] F.J.W. Podd, H.I. Schlaberg, B.S. Hoyle. *Model-based parameterisation of a hydrocyclone air-core*, Ultrasonics 38 (2000) pp. 804–808

[15] R.A. Williams, O.M. Ilyas, T. Dyakowski, FJ. Dickin, J.A. Gutierrez,M. Wang, M.S. Beck, C. Shah, A. Rushton. *Air core imaging in cyclonic separators: implication for separator design and modelling*, The Chemical Engineering Journal 56 (1995) pp. 135-141

[16] R.A. Williams, FJ. Dickin, J.A. Gutierrez, T. Dyakowski, M.S. Beck. *Using electrical impedance tomography for controlling hydrocyclone underflow discharge*, Control Eng. Practice 5 (1997) pp. 253-256

[17] L.H. Tsoukalas, M. Ishii, Y. Mi. *A neurofuzzy methodology for impedance-based multiphase flow identification*, Engng Applic. Artif. Intell. 10 (1997) pp. 545-555

[18] H. Lemonnier, J.F. Peytraud. *Is 2D impedance tomography a reliable technique for two-phase flow?*, Nuclear Engineering and Design 184 (1998) pp. 253-268

[19] Q. Smit. *Material phase detection using capacitance tomography*, MSc. Thesis, Department of Electrical Engineering, University of Cape Town, (2000)

[20] G. Teague. *Mass Flow Measurement of Multi-Phase Mixtures by Means of Tomographic Techniques*, PhD. Thesis, Department of Electrical Engineering, University of Cape Town, (2002)

[21] R.M. West, X. Jia, R.A. Williams. *Parametric modelling in industrial process tomography*, 1st World Congress on Industrial Process Tomography, Buxton, Greater Manchester 14–17 April 1999.

[22] R.M. West, R.A. Williams. *Opportunities for data fusion in multi-modality tomography*, 1st World Congress on Industrial Process Tomography, Buxton, Greater Manchester 14–17 April 1999.

[23] J.A. Gutierrez, T. Dyakowski, M.S. Beck, R.A. Williams. *Using electrical impedance tomography for controlling hydrocyclone underflow discharge*, Powder Technology 108 (2000) pp. 180-184

[24] A. Vehtari, J. Lampinen. *Bayesian MLP neural networks for image analysis*, Pattern Recognition Letters 21 (2000) pp. 1183-1191

[25] J. Lampinen, A. Vehtari, K. Leinonen. *Application of Bayesian neural network in electrical impedance tomography*, [Online] Available: http://www.lce.hut.fi/publications/ pdf/P375_LampinenVehtariLeinonen.pdf [2005, September 23]

[26] A. Giannopoulos. *Investigation of sine-wave inputs for an FDM EIT system*, MSc. Thesis, Department of Electrical Engineering, University of Cape Town, (2003)

[27] V. Capindissa. *Monitoring an industrial hydrocyclone using frequency domain multiplexing electrical impedance tomography*, MSc. Thesis, Department of Electrical Engineering, University of Cape Town, (2005)

[28] G. Goldswain. *An Investigation into the dynamic implementation of a 16-electrode FDM electrical impedance tomography system*, MSc. Thesis, Department of Electrical Engineering, University of Cape Town, (2005)

[29] Th. Neesse, M. Schneider, V. Golyk, H. Tiefel. *Measuring the operating state of the hydrocyclone*, Minerals Engineering 17 (2004) pp. 697–703

[30] H.J. Jeon, B.Y. Choi, M.C. Kim, K.Y. Kim, S. Kim. *Phase boundary estimation in two-phase flows with electrical impedance imaging technique*, Int. Comm. Heat Mass Transfer 31 (2004) pp. 1105–1114

[31] G. Teague, J. Tapson, Q. Smit. *Neural network reconstruction for tomography of a gravel-air-seawater mixture*, Measurement Science and Technology 12 (2001) pp. 1102-1108

[32] E.W. Randall, A.J. Wilkinson, T.M. Long, A. Sutherland. *A high speed current pulse electrical resistance tomography system for dynamic process monitoring*, Proceedings of ESDA 2004, 7th Biennial ASME Engineering Systems Design and Analysis, Manchester, UK July 19-22 2004

[33] A.J. Wilkinson, E.W. Randall, J.J. Cilliers, D.R. Durrett, T. Naidoo, T. Long. *A 1000-measurement frames/second ERT data capture system with real-time visualization*, IEEE Sensors Journal 5 (2005) pp. 300-307

[34] H.J. Jeon, J.H. Kim, B.Y. Choi, K.Y. Kim, M.C. Kim, S. Kim. *Electrical impedance imaging of binary mixtures with boundary estimation approach based on a multilayer neural network*, IEEE Sensors Journal 5 (2005) pp. 313-319

[35] E.W. Randall, A.J. Wilkinson, T.M. Long, A. Collins. *The design of a flexible multi-layer ERT system and an evaluation of its performance*, 4th World Congress of Industrial Process Tomography, Aizu, Japan, 2005

[36] M. Wang. *Impedance mapping of particulate multiphase flows*, Flow Measurement and Instrumentation 16 (2005) pp. 183–189

[37] K.Y. Kim, B.S. Kim, M.C. Kim, K.J. Lee, Y.J. Ko, S. Kim. *Electrical impedance imaging of two-phase flows undergoing rapid transient: Part I. Dynamic imaging*, International Communications in Heat and Mass Transfer 32 (2005) pp. 639–647

[38] K.Y. Kim, B.S. Kim, M.C. Kim, K.J. Lee, Y.J. Ko, S. Kim. *Electrical impedance imaging of two-phase flows undergoing rapid transient: Part II. Effect of input current pattern*, International Communications in Heat and Mass Transfer 32 (2005) pp. 648–656

[39] M.S. Beck, R.A. Williams. *Process tomography: a European innovation and its applications*, Meas. Sci. Technol. 7 (1996) pp. 215–224

[40] De Beers Canada, *What is Mineral Processing*, [Online] Available: http://www.debeerscanada.com/files_2/mineral_processing_1.html [2006, January 20]

[41] ITS, *What is Process Tomography*, [Online] Available: http://www.itoms.com/what_is_process_tomography.htm [2006, January 20]

[42] University of Manchester, *What is Tomography*, [Online] Available: http://www.tomography.manchester.ac.uk/whattom.shtml [2006, January 20]

[43] University of Manchester, *Basic Principles of Tomography*, [Online] Available: http://www.tomography.manchester.ac.uk/basic.shtml [2006, January 20]

[44] Pace, *What is Process Tomography*, [Online] Available: http://www.pace.leeds.ac.uk/pace/what.htm#top [2006, January 20]

[45] H. Demuth, M. Beale. *Neural network toolbox for use with MATLAB*, version 4, The MathWorks, Inc. (2005)

[46] Oxford English Dictionary, Tomography, [Online] Available: http://dictionary.oed.com/cgi/entry/50254165?single=1&query_type=word&queryword=tomography&first=1&max_to_show=10 [2006, January 20]

[47] P. Hua, E.J. Woo. *Electrical Impedance Tomography*, Reconstruction Algorithms, IOP Publishing (1990)

[48] T. Long. *A software front end for a real-time electrical resistance tomography imaging system*, B.Sc. Thesis (2003)

Appendix A

Drawings of Hydrocyclone Sections, Electrode Rigs and Connecter Wiring Diagrams

(Conical and Cylindrical Section drawings done by V. Capindissa [27])

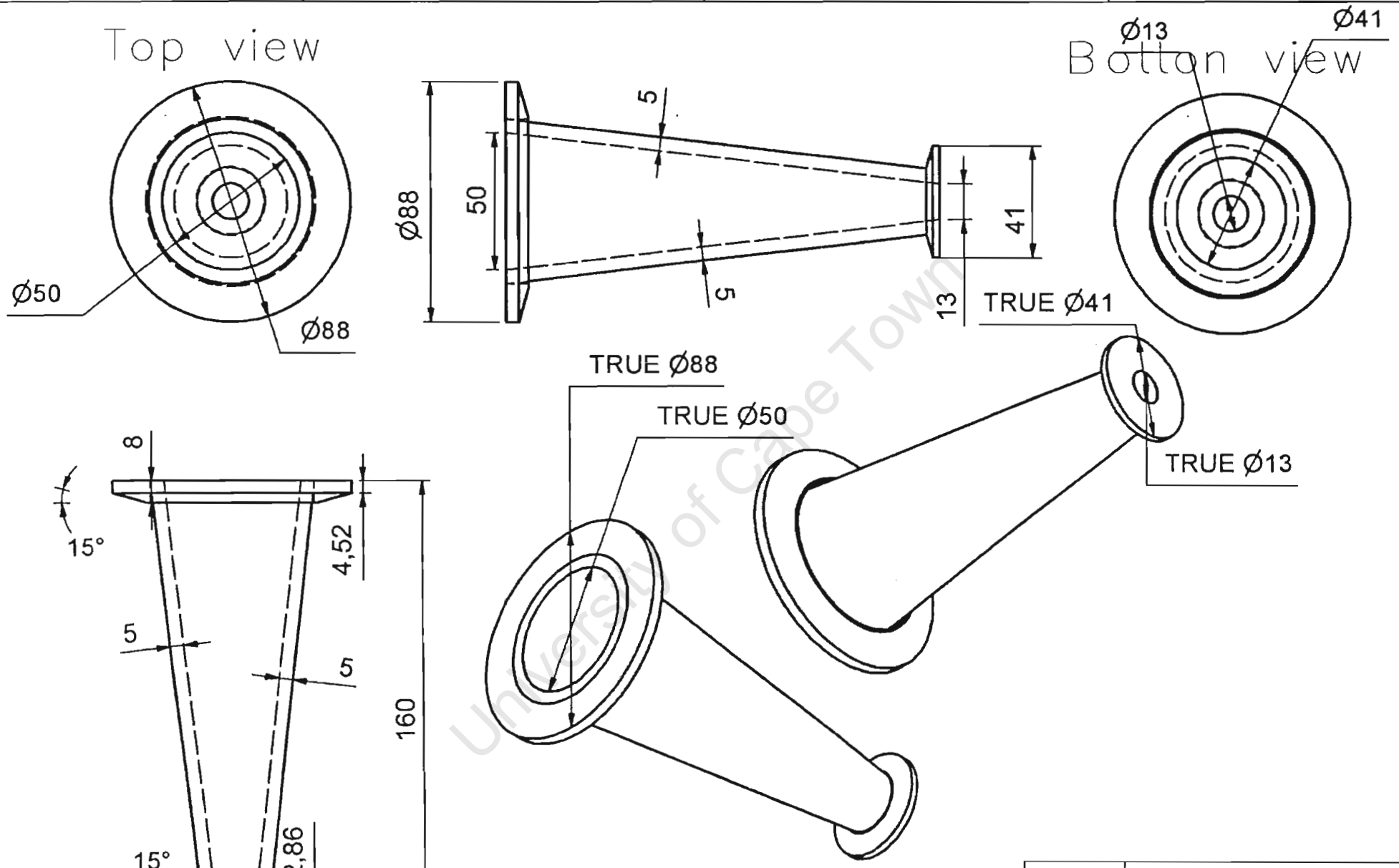

	UNIVERSITY OF CAPE TOWN Department of Mechanical Engineering
	Title: Hydrocyclone
Dimentions in mm Tolerance U.O.S	Scale Date: 01/08/03 Sheet 2 of 2
	Drawn By: Vladimir Capindisso Drawing Number: 2

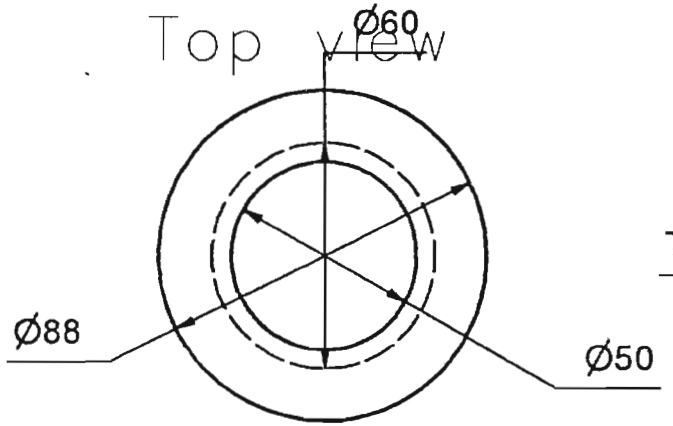

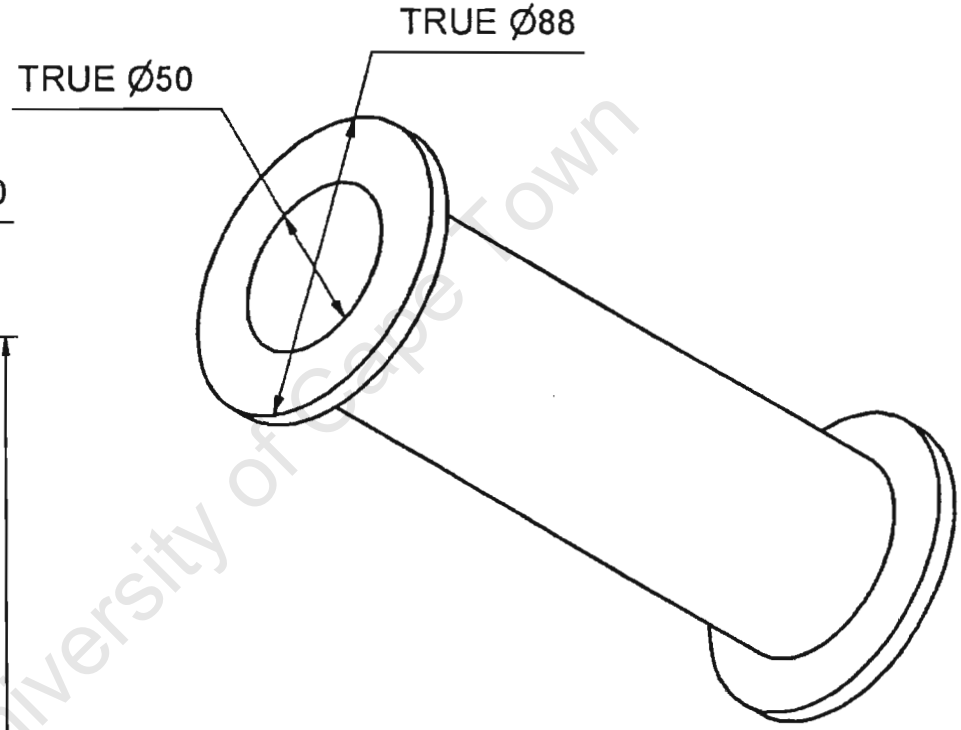

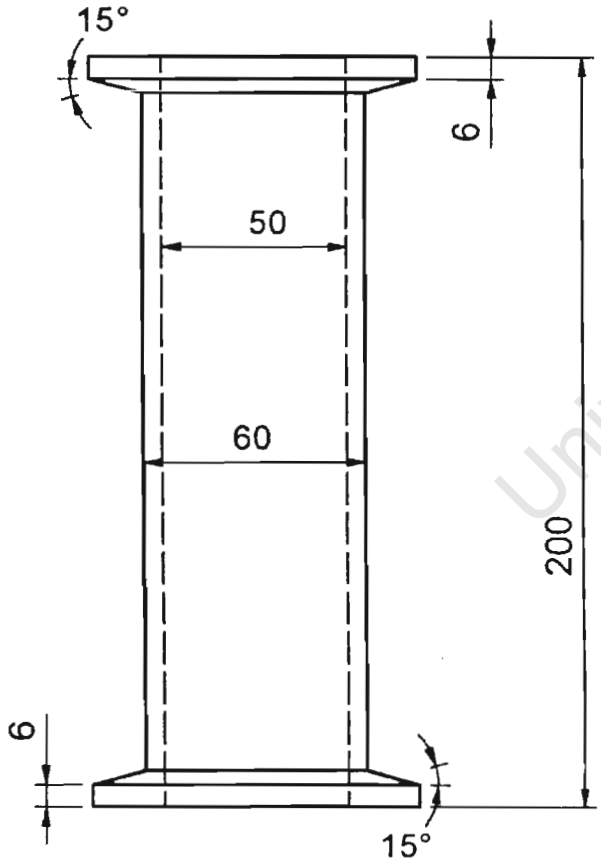

UNIVERSITY OF CAPE TOWN
Department of Mechanical Engineering

Title: Hydrocyclone

Dimentions in mm
tolerance U.O.S

Scale:

Date: 01/08/03

Sheet 1 of 2

Drawn By: Vladimir Capindisso

Drawing Number: 1

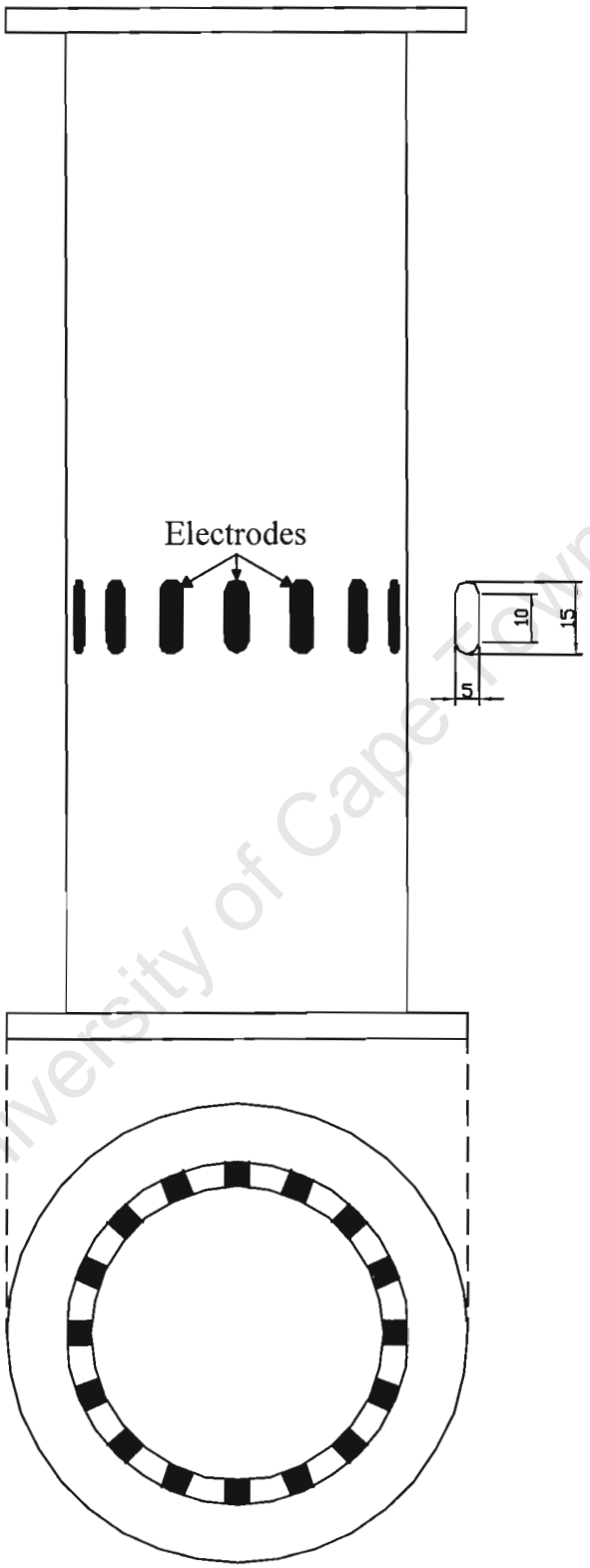

Title	**Single Plane Vessel**	
Size A	Document Number	Rev 0
Date Wednesday, March 30, 2005	Sheet 1 of 1	

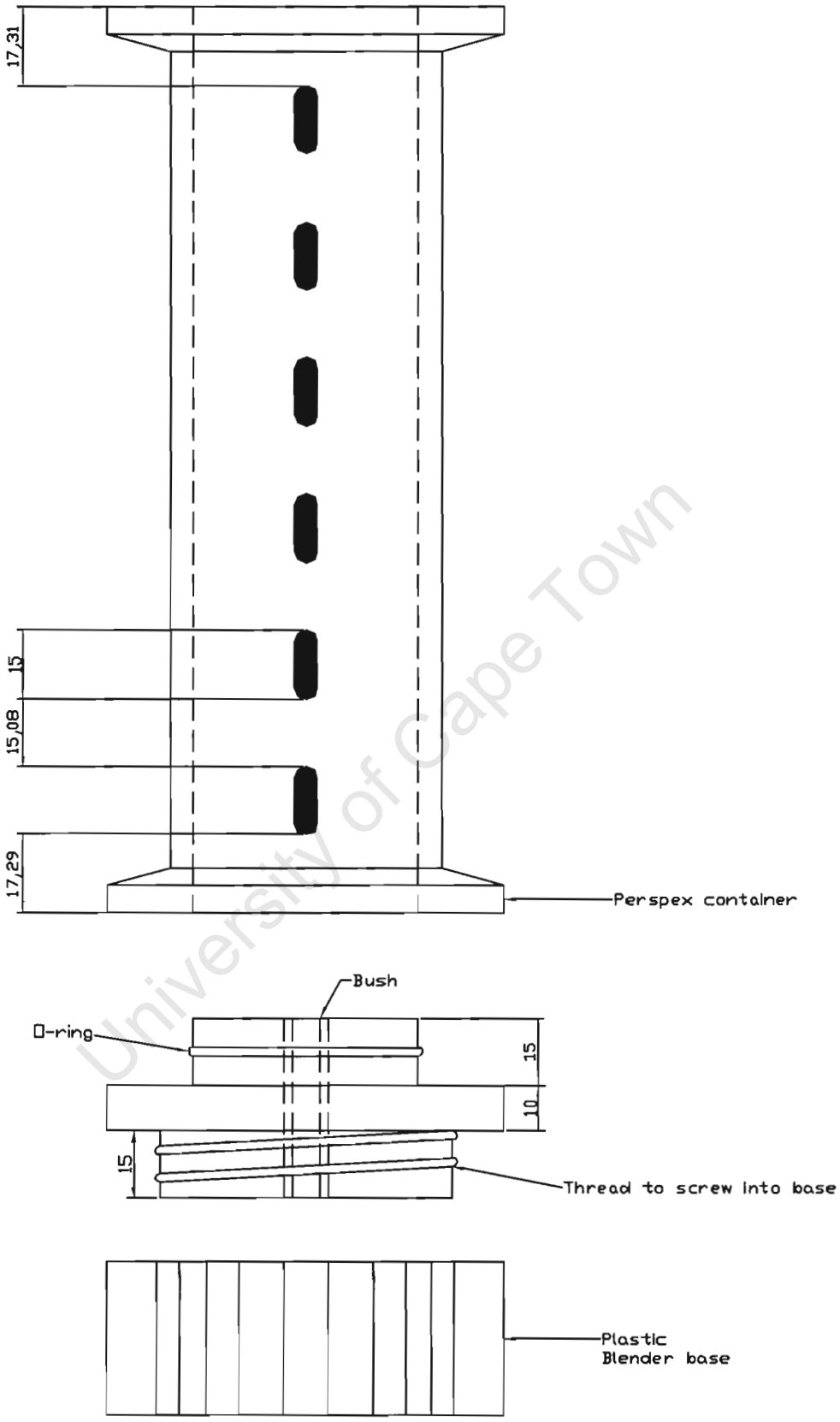

Title	**6-Plane Electrode Vessel and Base**	
Size A	Document Number	Rev 0
Date Tuesday, April 12, 2005	Sheet 1 of 1	

TO ERT
DB25 (male)

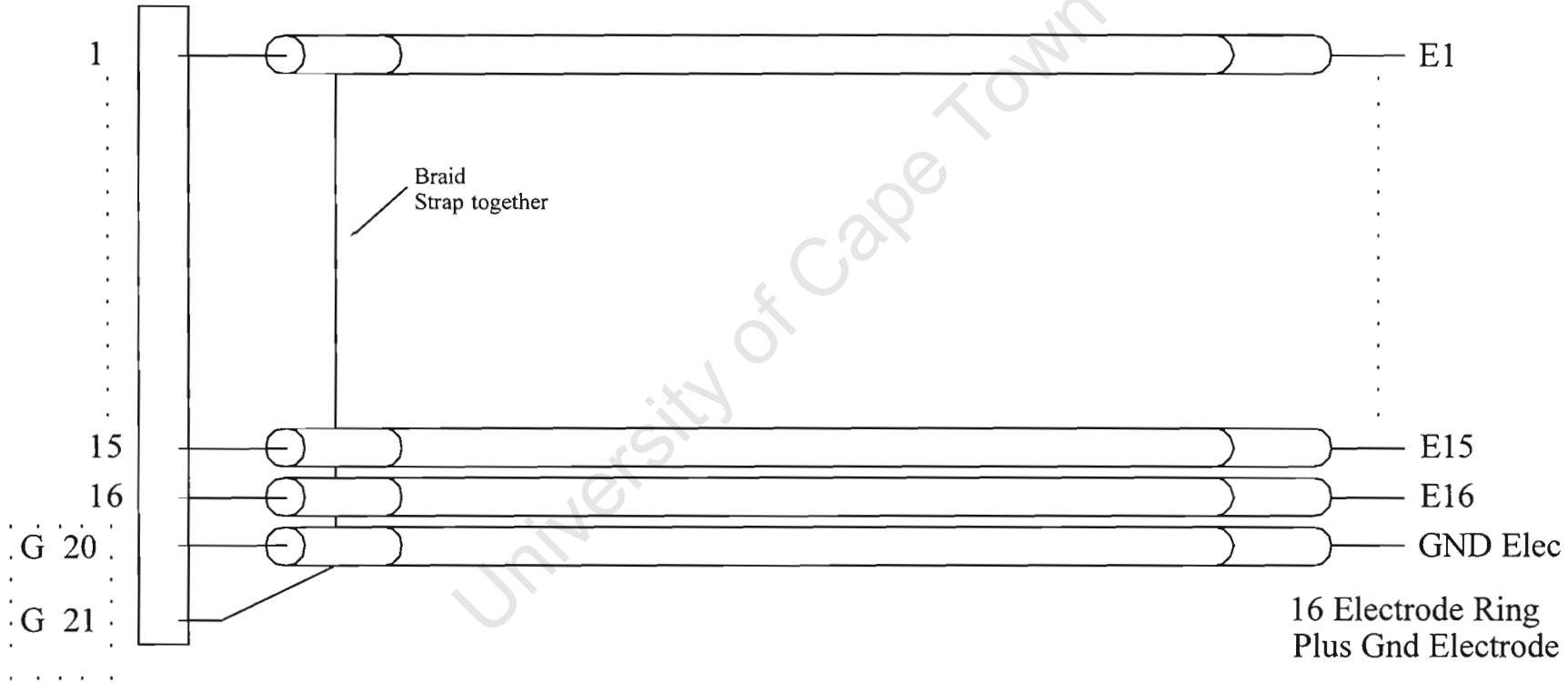

Title: **ERT Electrode Cable**		
Size: **A**	Document Number: ERTCABLE.OPJ(cable)	Rev: 0
Date: Wednesday, March 22, 2006	Sheet: 1 of 1	

TO ERT
Centronics 36 Way (male)

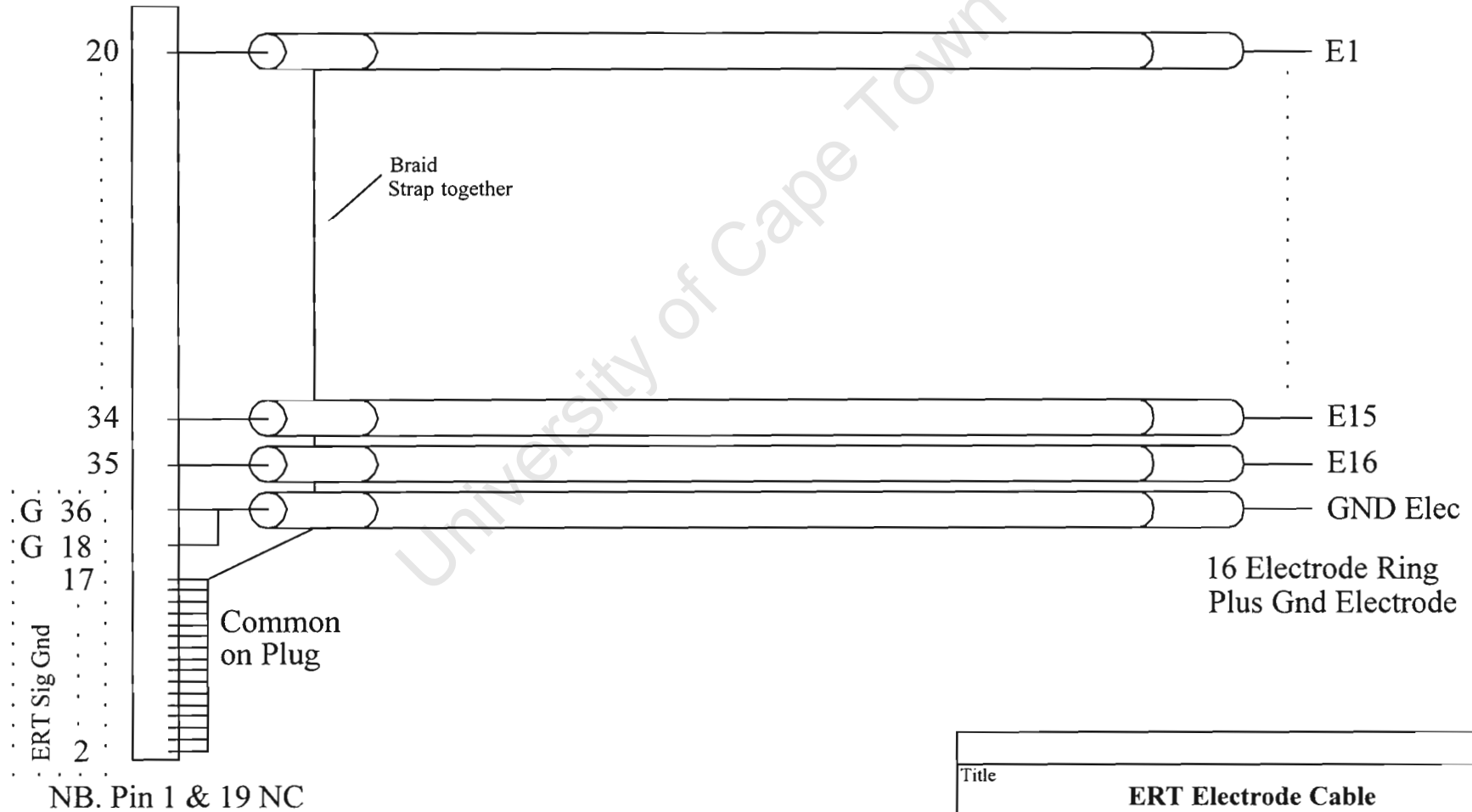

NB. Pin 1 & 19 NC

Title	**ERT Electrode Cable**	
Size: A	Document Number: ERTCABLE.OPJ(cable)	Rev: 0
Date: Wednesday, March 22, 2006	Sheet: 1 of 1	

Appendix B

Computer Code for FDM and TDM ERT Systems

TDM Single-Plane Static Image Reconstruction

```
% open mesh file
meshfilename = '22cm_no_hole_(836).mes';
mymesh = open_mesh_file(meshfilename);
disp('read in mesh file');
% open con file
[confilename, pathname] = uigetfile('*.con', 'Pick a file to display');
%confilename = '22cm_no_holes_0.0001_0.con';
fid = fopen([pathname confilename], 'rb');
colourmaprange = [0.1 1.2];
cmap = 'jet';
if(fid == -1)
    disp('Invalid filename');
    return;
end
data = [];
while feof(fid) == 0

    data = [data ; fread(fid, mymesh.n_elements, 'float32')'];

end
fclose(fid);
data = mean(data);
disp('read in binary file');
% regrid
n_samples = 100;
[gridx,gridy] = meshgrid(-mymesh.radius:mymesh.radius/(n_samples/2):mymesh.radius,-myme↙
sh.radius:mymesh.radius/(n_samples/2):mymesh.radius);
map_ = griddata(mymesh.midpoints.x, mymesh.midpoints.y, data, gridx, gridy, 'linear');
% save
filenamelength = length(confilename);
savefilename = [pathname confilename(1:filenamelength-4) '.mat']
save(savefilename, 'map_');
imagesc(map_);
axis equal;
caxis(colourmaprange);
colormap(cmap);
figure
```

```
% open mesh file
meshfilename = '22cm_no_hole_(836).mes';
mymesh = open_mesh_file(meshfilename);
disp('read in mesh file');
% open bin file
[binfilename, pathname] = uigetfile('*.bin', 'Pick a file to display');
%binfilename = '22cm_no_holes_0.0001_0.bin';
fid = fopen([pathname binfilename], 'rb');
if(fid == -1)
    disp('Invalid filename');
    return;
end
data = [];
n = 0;
%while feof(fid) == 0

    data = fread(fid, [mymesh.n_elements inf], 'float32');
 %   fprintf('.');

 %   if mod(n,30) == 0
 %       fprintf(' %d\n', n);
 %   end
 %   n =n+1;
%end
fclose(fid);
%data = mean(data);
disp('read in binary file');
% regrid
 n_samples = 100;
%
% [m, p] = size(data);
% ave_list = [];
% hh = figure;
%
% for i=1:m
%
%     [gridx,gridy] = meshgrid(-mymesh.radius:mymesh.radius/(n_samples/2):mymesh.radius↙
,-mymesh.radius:mymesh.radius/(n_samples/2):mymesh.radius);
%     map_ = griddata(mymesh.midpoints.x, mymesh.midpoints.y, stdlist, gridx, gridy, 'l↙
inear');
%
%     %% average map_
%     if mod(i,5) == 0
%         imagesc(map_);
%     end
%
%     ave_list = [ave_list; mean(mean(map_))];
%
% end
%
% % save
% filenamelength = length(binfilename);
```

```
%
% savefilename = [pathname binfilename(1:filenamelength-4) '.mat']
%
% save(savefilename, 'map_');
dataT = data';
stdlist = std(dataT);
n_samples = 100;
[gridx,gridy] = meshgrid(-mymesh.radius:mymesh.radius/(n_samples/2):mymesh.radius,-mymesh.radius:mymesh.radius/(n_samples/2):mymesh.radius);
map_ = griddata(mymesh.midpoints.x, mymesh.midpoints.y, stdlist, gridx, gridy, 'linear');
figure
imagesc(map_)
colorbar
colormap hot
title('Standard deviation in image - no averaging')
colormap hot
figure
plot(((data(1,:))))
title('Time sequence of reconstructed conductivity in one pixel element')
figure
plot(abs(fft(data(400,:)-mean(data(400,:)))))
title('FFT of a time sequence of the conductivity in 1 pixel element')
```

TDM Single-Plane Movie Creation

```
%%%%%%%%%%%%%%%%%%5
% makes a movie from a reconstructed data file
% run 'convertbinconductivity.m' first
%%%%%%%%%%%%%%%%%%%%%%%%%%%%%%%%

moviefilename = 'fe.avi';
framerate = 10.24;
colourmaprange = [0.1 1.2];
cmap = 'jet';

% n_samples = 100;
% [gridx,gridy] = meshgrid(-mymesh.radius:mymesh.radius/(n_samples/2):mymesh.radius,-my↙
mesh.radius:mymesh.radius/(n_samples/2):mymesh.radius);

[p n] = size(dataT);

aviobj = avifile(moviefilename, 'fps', framerate);

i = [];
for i=300:500
    %axis manual
    %plot(dataT(i, :))
    %axis([0 900 -1 3])
    map_ = griddata(mymesh.midpoints.x, mymesh.midpoints.y, dataT(i,:), gridx, gridy, '↙
linear');
    %subplot(2,1,1);
    %imagesc(map_);
    %axis equal;

    h = imagesc(map_);
    %set(h, 'edgecolor', [0.7 0.7 0.7], 'edgealpha', 0.5);
    %axis([0 100 0 100 -1.5 1.5])
    %%caxis(colourmaprange);
    %colormap(cmap);

    %subplot(2,1,2);
    %axis manual;
    %plot(newM(i, :));
    %axis([0 209 0 2])

    M(i) = getframe(gcf);
    aviobj = addframe(aviobj, M(i));
end

aviobj = close(aviobj);
```

FDM Re-Order Function

```
function [frame] = re_order(data)

% Written by Gareth Goldswain, 2005
%
% [frame] = re_order(data)
%
% This function returns in [frame] the re-ordered frame data.  This is necessary due to the
% messy way in which the data aquisition board captures the data.  It is rearranged to comply
% with Siggys projection order in fem.m. i.e TxA/RxA, TxA/Rxb, ..... , TxH/RxH
%
% (data) can be a vector or matrix.  If a vector then it represents one frame of data.  If a
% matrix then as many frames as rows are represented.

% the entries in reorder were found empirically and are related to the order in which the the demodulation
% boards' multiplexers spit out the data captured from the rig.  Note that this order is specific to the
% way in which the boards are wired for THIS project i.e. using capacitance demod channels as resistance
% demod channels for extra electrodes.

reorder = [29 33 30 34 31 35 32 36 21 41 22 42 23 43 24 44 13 49 14 50 15 51 16 52 5 57 6 58 7 59 8 60 25 37 26 38 27 39 28 40 17 45 18 46 19 47 20 48 9 53 10 54 11 55 12 56 1 61 2 62 3 63 4 64];

frame = data(:,reorder);
```

Adding Target Values Function for FDM System

```
%Adda the Target Values.

%Created by Jeremy Elliott 09/11/2005

five(:,65) = 5;
seven(:,65) = 7;
eight(:,65) = 8;
nine(:,65) = 9;
ten(:,65) = 10;
eleven(:,65) = 11;
twelve(:,65) = 12;
thirteen(:,65) = 13;
fourteen(:,65) = 14;
fifteen(:,65) = 15;
sixteen(:,65) = 16;
seventeen(:,65) = 17;
eighteen(:,65) = 18;
twenty(:,65) = 20;
noth(:,65) = 0;
```

FDM Matrix Creation

```
%Puts all the frames into two large matrice's (traing and simulation/testing).

%Written by Jeremy Elliott 01/11/2005.

%Creates training set.

TrainM = five(1:3000,:);
TrainM(3001:6000,:) = seven(1:3000,:);
TrainM(6001:9000,:) = eight(1:3000,:);
TrainM(9001:12000,:) = nine(1:3000,:);
TrainM(12001:15000,:) = ten(1:3000,:);
TrainM(15001:18000,:) = eleven(1:3000,:);
TrainM(18001:21000,:) = twelve(1:3000,:);
TrainM(21001:24000,:) = thirteen(1:3000,:);
TrainM(24001:27000,:) = fourteen(1:3000,:);
TrainM(27001:30000,:) = fifteen(1:3000,:);
TrainM(30001:33000,:) = sixteen(1:3000,:);
TrainM(33001:36000,:) = seventeen(1:3000,:);
TrainM(36001:39000,:) = eighteen(1:3000,:);
TrainM(39001:42000,:) = twenty(1:3000,:);
TrainM(42001:45000,:) = noth(1:3000,:);

%Creates validation set.

ValidationM = five(4001:5000,:);
ValidationM(1001:2000,:) = seven(4001:5000,:);
ValidationM(2001:3000,:) = eight(4001:5000,:);
ValidationM(3001:4000,:) = nine(4001:5000,:);
ValidationM(4001:5000,:) = ten(4001:5000,:);
ValidationM(5001:6000,:) = eleven(4001:5000,:);
ValidationM(6001:7000,:) = twelve(4001:5000,:);
ValidationM(7001:8000,:) = thirteen(4001:5000,:);
ValidationM(8001:9000,:) = fourteen(4001:5000,:);
ValidationM(9001:10000,:) = fifteen(4001:5000,:);
ValidationM(10001:11000,:) = sixteen(4001:5000,:);
ValidationM(11001:12000,:) = seventeen(4001:5000,:);
ValidationM(12001:13000,:) = eighteen(4001:5000,:);
ValidationM(13001:14000,:) = twenty(4001:5000,:);
ValidationM(14001:15000,:) = noth(4001:5000,:);

%Creates simulation set.

SimulationM = five(3001:4000,:);
SimulationM(1001:2000,:) = seven(3001:4000,:);
SimulationM(2001:3000,:) = eight(3001:4000,:);
SimulationM(3001:4000,:) = nine(3001:4000,:);
SimulationM(4001:5000,:) = ten(3001:4000,:);
SimulationM(5001:6000,:) = eleven(3001:4000,:);
SimulationM(6001:7000,:) = twelve(3001:4000,:);
SimulationM(7001:8000,:) = thirteen(3001:4000,:);
SimulationM(8001:9000,:) = fourteen(3001:4000,:);
SimulationM(9001:10000,:) = fifteen(3001:4000,:);
```

```
SimulationM(10001:11000,:) = sixteen(3001:4000,:);
SimulationM(11001:12000,:) = seventeen(3001:4000,:);
SimulationM(12001:13000,:) = eighteen(3001:4000,:);
SimulationM(13001:14000,:) = twenty(3001:4000,:);
SimulationM(14001:15000,:) = noth(3001:4000,:);

%Call the functions that randomize the rows in the matrice's so that the network will b↙
e trained
%realistically.

FinalTrain = rand_train(TrainM);
FinalSimulation = rand_sim(SimulationM);
FinalValidation = rand_val(ValidationM);
```

FDM Matrix Shuffling Function

```
%Shuffles matrix rows.

function [frame_mat] = create_mat(data_mat)

shuffle_mat = randperm(7000);

frame_mat = data_mat(shuffle_mat,:);
```

TDM Re-Order Function

```
function [frame] = re_orderTDM(data)

reorder = [3 4 5 6 7 8 9 10 11 12 13 14 15 20 21 22 23 24 25 26 27 28 29 30 31 32 33 37
 38 39 40 41 42 43 44 45 46 47 48 49 50 54 55 56 57 58 59 60 61 62 63 64 65 66 67 71 72
 73 74 75 76 77 78 79 80 81 82 83 84 88 89 90 91 92 93 94 95 96 97 98 99 100 101 105 10
6 107 108 109 110 111 112 113 114 115 116 117 118 122 123 124 125 126 127 128 129 130 1
31 132 133 134 135 139 140 141 142 143 144 145 146 147 148 149 150 151 152 156 157 158
159 160 161 162 163 164 165 166 167 168 169 173 174 175 176 177 178 179 180 181 182 183
 184 185 186 190 191 192 193 194 195 196 197 198 199 200 201 202 203 207 208 209 210 21
1 212 213 214 215 216 217 218 219 220 224 225 226 227 228 229 230 231 232 233 234 235 2
36 237 242 243 244 245 246 247 248 249 250 251 252 253 254];

frame = data(:,reorder);
```

TDM Matrix Creation

```
%Puts all the frames into two large matrice's (traing and simulation/testing).

%Written by Jeremy Elliott 01/11/2005.

%Creates training set.

TrainM = five(1:3000,:);
TrainM(3001:6000,:) = seven(1:3000,:);
TrainM(6001:9000,:) = eight(1:3000,:);
TrainM(9001:12000,:) = nine(1:3000,:);
TrainM(12001:15000,:) = ten(1:3000,:);
TrainM(15001:18000,:) = eleven(1:3000,:);
TrainM(18001:21000,:) = twelve(1:3000,:);
TrainM(21001:24000,:) = thirteen(1:3000,:);
TrainM(24001:27000,:) = fourteen(1:3000,:);
TrainM(27001:30000,:) = fifteen(1:3000,:);
TrainM(30001:33000,:) = sixteen(1:3000,:);
TrainM(33001:36000,:) = seventeen(1:3000,:);
TrainM(36001:39000,:) = eighteen(1:3000,:);
TrainM(39001:42000,:) = twenty(1:3000,:);
TrainM(42001:45000,:) = nothing(1:3000,:);

%Creates validation set.

ValidationM = five(4001:5000,:);
ValidationM(1001:2000,:) = seven(4001:5000,:);
ValidationM(2001:3000,:) = eight(4001:5000,:);
ValidationM(3001:4000,:) = nine(4001:5000,:);
ValidationM(4001:5000,:) = ten(4001:5000,:);
ValidationM(5001:6000,:) = eleven(4001:5000,:);
ValidationM(6001:7000,:) = twelve(4001:5000,:);
ValidationM(7001:8000,:) = thirteen(4001:5000,:);
ValidationM(8001:9000,:) = fourteen(4001:5000,:);
ValidationM(9001:10000,:) = fifteen(4001:5000,:);
ValidationM(10001:11000,:) = sixteen(4001:5000,:);
ValidationM(11001:12000,:) = seventeen(4001:5000,:);
ValidationM(12001:13000,:) = eighteen(4001:5000,:);
ValidationM(13001:14000,:) = twenty(4001:5000,:);
ValidationM(14001:15000,:) = nothing(4001:5000,:);

%Creates simulation set.

SimulationM = five(3001:4000,:);
SimulationM(1001:2000,:) = seven(3001:4000,:);
SimulationM(2001:3000,:) = eight(3001:4000,:);
SimulationM(3001:4000,:) = nine(3001:4000,:);
SimulationM(4001:5000,:) = ten(3001:4000,:);
SimulationM(5001:6000,:) = eleven(3001:4000,:);
SimulationM(6001:7000,:) = twelve(3001:4000,:);
SimulationM(7001:8000,:) = thirteen(3001:4000,:);
SimulationM(8001:9000,:) = fourteen(3001:4000,:);
SimulationM(9001:10000,:) = fifteen(3001:4000,:);
```

```
SimulationM(10001:11000,:) = sixteen(3001:4000,:);
SimulationM(11001:12000,:) = seventeen(3001:4000,:);
SimulationM(12001:13000,:) = eighteen(3001:4000,:);
SimulationM(13001:14000,:) = twenty(3001:4000,:);
SimulationM(14001:15000,:) = nothing(3001:4000,:);

%Call the functions that randomize the rows in the matrice's so that the network will b↙
e trained
%realistically.

FinalTrain = rand_trainTDM(TrainM);
FinalSimulation = rand_simTDM(SimulationM);
FinalValidation = rand_valTDM(ValidationM);
```

TDM Shuffle Function

```
%Shuffles the matrice rows individually.

function [frame_mat] = create_mat(data_mat)

shuffle_mat = randperm(7000);

frame_mat = data_mat(shuffle_mat,:);
```

```
%Function that trains the neural network by means of first pre-processing
%the data, and then training with the aid of a validation set.

%Written by Jeremy Elliott 23/11/2005.

%Creates the inputs and targets and validation data.

Input = FinalTrain(:,1:208);
Target = FinalTrain(:,209);

ValidIn = FinalValidation(:,1:208);
ValidT = FinalValidation(:,209);

SimulationIn = FinalSimulation(:,1:208);
SimulationT = FinalSimulation(:,209);

%Pre-process the matrices to get the Mean and Std deviation etc.

[IN,meanIN,stdIN,TN,meanTN,stdTN] = prestd(Input',Target');
%[IV,meanIV,stdIV,TV,meanTV,stdTV] = prestd(ValidIn',ValidT');
%[IS,meanIS,stdIS,TS,meanTS,stdTS] = prestd(SimulationIn',SimulationT');

[yv xv] = size(ValidIn);
Valid = ValidIn';
for i = 1:xv
    for j = 1:yv
        IV(i,j) = (Valid(i,j)-meanIN(i,1))/stdIN(i,1);
    end
end
[TV,meanTV,stdTV] = prestd(ValidT');

[ys xs] = size(SimulationIn);
Sim = SimulationIn';
for i = 1:xs
    for j = 1:ys
        IS(i,j) = (Sim(i,j)-meanIN(i,1))/stdIN(i,1);
    end
end

%Create validation set.

val.P = IV;
val.T = TV;

% Trains the neural network for 64 inputs.

net = newff(minmax(IN),[33,1],{'tansig','purelin'},'trainrp','learngd'); %Creates a fee↙
d-forward backpropogation network.
net.trainParam.show = 5;    %The training status is displayed for every 'show' iteratio↙
n of the algorithm.
net.trainParam.epochs = 400; %Determines when traing stops (if no of iterations exceeds↙
 epochs).
```

```
net.trainParam.goal = 0;    %Determines when traing stops (if performance drops below '↙
goal').
net.trainParam.max_fail = 10;
[net,tr] = train(net,IN,TN,[],[],val);

%Simulate the training inputs.

an = sim(net,IN);

%Post-process the results

result = poststd(an,meanTN,stdTN);

%Simulate the unseen data.

sn = sim(net,IS);

%Post-process the results

result2 = poststd(sn,meanTN,stdTN);
```

```
%Function that trains the neural network by means of first pre-processing
%the data, and then training with the aid of a validation set.

%Written by Jeremy Elliott 08/11/2005.

%Creates the inputs and targets and validation data.

Input = FinalTrain(:,1:64);
Target = FinalTrain(:,65);

ValidIn = FinalValidation(:,1:64);
ValidT = FinalValidation(:,65);

SimulationIn = FinalSimulation(:,1:64);
SimulationT = FinalSimulation(:,65);

%Pre-process the matrices to get the Mean and Std deviation etc.

[IN,meanIN,stdIN,TN,meanTN,stdTN] = prestd(Input',Target');
%[IV,meanIV,stdIV,TV,meanTV,stdTV] = prestd(ValidIn',ValidT');
%[IS,meanIS,stdIS,TS,meanTS,stdTS] = prestd(SimulationIn',SimulationT');

[yv xv] = size(ValidIn);
Valid = ValidIn';
for i = 1:xv
    for j = 1:yv
        IV(i,j) = (Valid(i,j)-meanIN(i,1))/stdIN(i,1);
    end
end
[TV,meanTV,stdTV] = prestd(ValidT');

[ys xs] = size(SimulationIn);
Sim = SimulationIn';
for i = 1:xs
    for j = 1:ys
        IS(i,j) = (Sim(i,j)-meanIN(i,1))/stdIN(i,1);
    end
end

%Create validation set.

val.P = IV;
val.T = TV;

% Trains the neural network for 64 inputs.

net = newff(minmax(IN),[25,1],{'tansig','purelin'},'trainrp','learngd'); %Creates a fee↙
d-forward backpropogation network.
net.trainParam.show = 5;    %The training status is displayed for every 'show' iteratio↙
n of the algorithm.
net.trainParam.epochs = 400; %Determines when traing stops (if no of iterations exceeds↙
 epochs).
```

```
net.trainParam.goal = 0;    %Determines when traing stops (if performance drops below '↙
goal').
net.trainParam.max_fail = 10;
[net,tr] = train(net,IN,TN,[],[],val);

%Simulate the training inputs.

an = sim(net,IN);

%Post-process the results

result = poststd(an,meanTN,stdTN);

%Simulate the unseen data.

sn = sim(net,IS);

%Post-process the results

result2 = poststd(sn,meanTN,stdTN);
```

```
%This function uses the trained neural network to simulate the data
%captured from the blender, as though it were doing it in real time.
%A movie file is then created which shows both the relevant voltages and
%the resultant diameter prediction for the blender, frame by frame.

%Created by Jeremy Elliott 08/11/2005

moviefilename = 'blend1.avi';
framerate = 10.24;
colourmaprange = [0.1 1.2];
cmap = 'jet';

% n_samples = 100;
% [gridx,gridy] = meshgrid(-mymesh.radius:mymesh.radius/(n_samples/2):mymesh.radius,-my↙
mesh.radius:mymesh.radius/(n_samples/2):mymesh.radius);

[p n] = size(SS);

SE = SS';

aviobj = avifile(moviefilename, 'fps', framerate);

i = [];
for i=1:p

    %Pre-processing.

    for j = 1:64
        PN(j,1) = (SE(j,i)-meanIN(j,1))/stdIN(j,1);
    end

    %Network simulation and post-processing.

    AN = sim(net,PN);
    Diameter = poststd(AN,meanTN,stdTN);

    %Plotting of Graphs.

    axis manual;
    subplot(2,1,1);
    bar(2,Diameter);
    hold on;
    bar(1,SimulationT(i,1));
    axis([0 4 -5 25]);
    xlabel(Diameter,'fontsize',20);
    error = SimulationT(i,1) - Diameter;
    bar(3,error);
    hold off;

    subplot(2,1,2)
    plot(SimulationIn(i,:));
    xlabel('Voltage');
```

```
    axis([0 65 0 6])

    %Creation of the movie file.

    M(i) = getframe(gcf);
    aviobj = addframe(aviobj, M(i));
end

aviobj = close(aviobj);
```

6-Plane Movie Creation for TDM Unit

```
%%%%%%%%%%%%%%%%%5
% makes a movie from a reconstructed data file
% run 'convertbinconductivity.m' first
%%%%%%%%%%%%%%%%%%%%%%%%%%%%%


moviefilename = 'blend6plane.avi';
framerate = 10.24;
colourmaprange = [0.1 1.2];
cmap = 'jet';

[x,y,z] = meshgrid(0:1:100,0:1:100,1:1:6);


% n_samples = 100;
% [gridx,gridy] = meshgrid(-mymesh.radius:mymesh.radius/(n_samples/2):mymesh.radius,-my↙
mesh.radius:mymesh.radius/(n_samples/2):mymesh.radius);

[p n] = size(dataT);


aviobj = avifile(moviefilename, 'fps', framerate);

i = [];
for i=410:510
    %axis manual
    %plot(dataT(i, :))
    %axis([0 900 -1 3])
    map(:,:,6) = griddata(mymesh.midpoints.x, mymesh.midpoints.y, data5(i,:), gridx, gr↙
idy, 'linear');

    map(:,:,5) = griddata(mymesh.midpoints.x, mymesh.midpoints.y, data4(i,:), gridx, gr↙
idy, 'linear');

    map(:,:,4) = griddata(mymesh.midpoints.x, mymesh.midpoints.y, data3(i,:), gridx, gr↙
idy, 'linear');

    map(:,:,3) = griddata(mymesh.midpoints.x, mymesh.midpoints.y, data2(i,:), gridx, gr↙
idy, 'linear');

    map(:,:,2) = griddata(mymesh.midpoints.x, mymesh.midpoints.y, data1(i,:), gridx, gr↙
idy, 'linear');

    map(:,:,1) = griddata(mymesh.midpoints.x, mymesh.midpoints.y, dataT(i,:), gridx, gr↙
idy, 'linear');


    %subplot(2,1,1);
    %imagesc(map_);
    %axis equal;

    %%h = surf(map_);
```

```
    %%set(h, 'edgecolor', [0.7 0.7 0.7], 'edgealpha', 0.5);
    %%axis([0 100 0 100 -1.5 1.5])


    h = slice(x,y,z,map,[],[],[1 2 3 4 5 6]);
    alpha('color')
    set(h,'EdgeColor','none','FaceColor','interp','FaceAlpha','interp')
    %alphamap('rampdown')
    %alphamap('increase',.1)
    %colormap(hsv)

    caxis(colourmaprange);
    colormap(cmap);

    %label axes
    %text(23,-5,'Frame:','Fontsize',16)
    %title(i,'FontSize',16)
    %text(-18,110.5,'Predicted Diameter:','Fontsize',16)
    %xlabel(result7(i),'FontSize',16)
    %text(63,110.5,'mm','Fontsize',16)

    view(-37.50,16.00);

    %subplot(2,1,2);
    %axis manual;
    %plot(newM(i, :));
    %axis([0 209 0 2])

    M(i) = getframe(gcf);
    aviobj = addframe(aviobj, M(i));
end

aviobj = close(aviobj);
```

Appendix C

Screenshots Showing the Surface Plot Movie Created With MATLAB

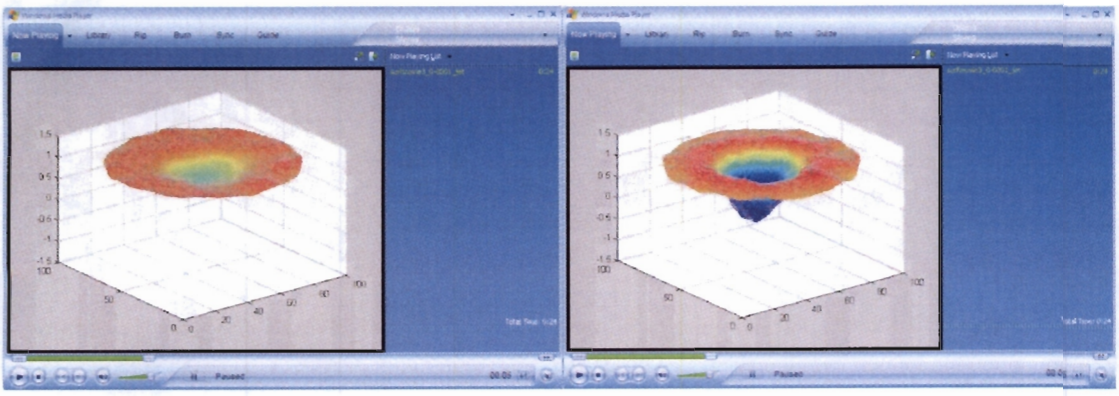

(a) (b)

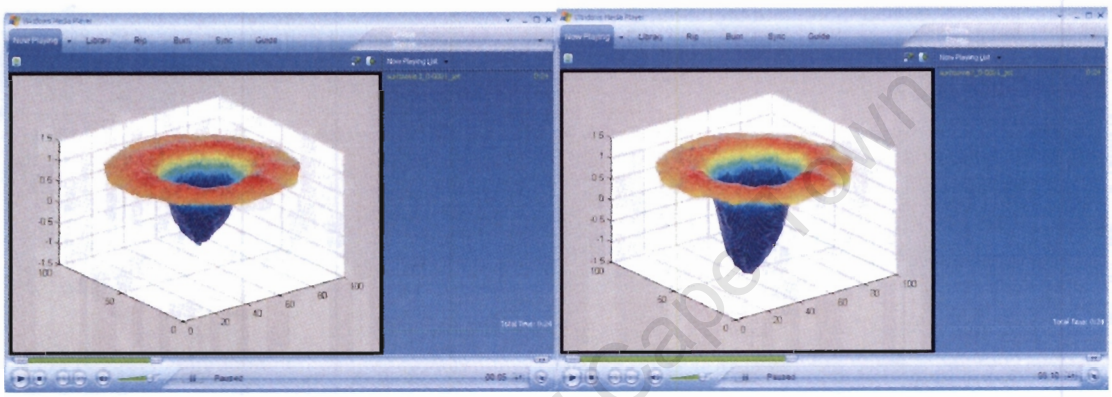

(c) (d)

Figure C (a-d): Screenshots of the surface plot movie created in MALAB. One can clearly see the air core formed by the blender.